



Max-Planck-Institut für Metallforschung
Stuttgart

Modeling of Crack-Tip Plasticity in Tungsten Single Crystals

Alexander Hartmaier

Dissertation
an der
Universität Stuttgart

Bericht Nr. 94
November 2000

Modeling of Crack-Tip Plasticity in Tungsten Single Crystals

Von der Fakultät Chemie der Universität Stuttgart
zur Erlangung der Würde eines Doktors der
Naturwissenschaften (Dr. rer. nat.) genehmigte Abhandlung

Vorgelegt von

ALEXANDER HARTMAIER

aus Zweibrücken



Hauptberichter:	Prof. Dr. phil. E. Arzt
Mitberichter:	Prof. Dr. rer. nat. H.-R. Trebin
Mitprüfer:	Prof. Dr. rer. nat. F. Aldinger
Tag der Einreichung:	15.08.2000
Tag der mündlichen Prüfung:	24.11.2000

MAX-PLANCK-INSTITUT FÜR METALLFORSCHUNG, STUTTGART

AUGUST 2000

for Sigrid

Acknowledgments

This work has been conducted at the *Max-Planck-Institut für Metallforschung* in Stuttgart.

I would like to express my sincere gratitude to Prof. E. Arzt for his continuous support and his interest in this work.

I am also indebted to Prof. H.-R. Trebin for his interest in this work.

I owe a strong debt of gratitude to Dr. P. Gumbsch for giving me the opportunity to cooperate on this challenging project, his substantial support during my stay at Stuttgart, and for many helpful discussions and insights.

I am grateful to Prof. L. P. Kubin and Dr. B. Devincre for inviting me to their institute and introducing me to their computational methods.

I would like to express my gratefulness to Prof. W. D. Nix for giving me the opportunity to work with his group and for the many discussions we enjoyed.

I would like to extend my thanks to all colleagues and guests at the *Max-Planck-Institut* for helping to create a pleasant and inspiring working atmosphere. In particular I would like to thank Dr. A. Wanner for critically reading the manuscript.

I gratefully acknowledge the financial support from the *Deutsche Forschungsgemeinschaft* (DFG) and travel grants from the *Deutscher Akademischer Austauschdienst* (DAAD) under nr. D/96/21803 and the *Klein, Schanzlin & Becker-(KSB)-Stiftung*.

Last but not least I am deeply indebted to my wife and my parents for their encouragement and support during my life as a student.

Abstract

Many materials exhibit a transition from brittle behavior at low temperatures to ductile response at higher temperatures. The mechanisms controlling this brittle-to-ductile transition (BDT) remain unclear despite the large efforts made in experimental and theoretical investigations. In particular, the question whether it is dislocation nucleation or dislocation mobility which controls crack-tip plasticity and thus the brittle-to-ductile transition is still unanswered. This problem is tackled again here by studying the plastic deformation of the crack-tip region on the basis of discrete dislocation models. Within these models dislocations are regarded as singular sources of stress in a linear-elastic medium in which also a crack is present. By virtue of their stress field the dislocations interact with each other as well as with the stress field of the crack. Dislocation velocity is calculated from these interaction forces and the equations of motion are integrated. The dislocation mobility is specific parameter of each material. The plastic deformation produced by the dislocations shields the crack tip from the applied load. The amount of shielding determines the fracture toughness of the considered material and, thus, its brittleness or ductility. Thus, discrete dislocation models can contribute to the understanding of the mechanisms controlling the BDT.

The results of the numerical studies performed in this work and their comparison with the results of an experimental study on tungsten single crystals (Riedle, 1995) leads to new insights on crack-tip plasticity and the BDT. The results are valid primarily for tungsten, but it can safely be assumed that they are transferable at least to other transition metals. A main conclusion drawn in this work is that crack-tip plasticity is limited by dislocation nucleation in well-annealed material at low temperatures. The lack of active dislocation sources prevents the emission of a sufficient number of dislocations to provide an efficient shielding of the crack tip. At higher temperatures the dislocation sources along the crack front become increasingly active and dislocation mobility starts to limit crack-tip plasticity and thus fracture toughness. The dislocations, which are generated in larger numbers, cannot leave the crack-tip region fast enough and thus inhibit the instantaneous nucleation of further dislocations.

The application of discrete dislocation models close to the BDT is difficult because of the high number of dislocations which is necessary to describe large plastic deformations. Therefore, no conclusive answer about the nature of the BDT can be given in this work. However, it seems to become clear that the blunting of the crack tip by plastic deformation plays an important role for the BDT. Further, it can be concluded from the comparison of model predictions with experimental results that screw dislocations, which are known to control bulk plasticity in transition metals, are not limiting crack-tip plasticity. A detailed

mechanism is proposed in this work which motivates the description of crack-tip plasticity as microplastic deformation, which is carried by non-screw dislocations.

Zusammenfassung

Viele Materialien zeigen einen Übergang von sprödem zu duktilem Verhalten bei steigender Temperatur. Die Mechanismen, die diesen Spröd-duktil-Übergang kontrollieren, sind trotz großer Anstrengungen experimenteller und theoretischer Natur immer noch nicht vollständig verstanden. Insbesondere die Frage, ob Rissspitzenplastizität und somit der Spröd-duktil-Übergang von der Versetzungsnukleation oder von der Versetzungsmobilität kontrolliert wird, ist immer noch unbeantwortet. In der vorliegenden Arbeit werden weitere Schritte unternommen, um dieser Antwort näher zu kommen. Dazu wird die plastische Verformung im Bereich einer Rissspitze mit Hilfe von diskreten Versetzungsmodellen untersucht. In diesen Modellen werden Versetzungen als singuläre Quellen mechanischer Spannungen in einem linear-elastischen Medium betrachtet. Die Versetzungen wechselwirken durch ihre Spannungsfelder sowohl untereinander als auch mit dem Spannungsfeld eines Risses. Die bekannten Wechselwirkungskräfte werden in Versetzungsgeschwindigkeiten umgerechnet und die Bewegungsgleichungen integriert. Die Mobilität der Versetzungen ist dabei eine materialspezifische Größe. Die von Versetzungen getragene plastische Verformung schirmt die Rissspitze von der äußeren Last ab. Der Betrag dieser Abschirmung bestimmt letztlich die Bruchzähigkeit des im Modell betrachteten Materials und somit auch dessen Sprödhheit oder Duktilität. Diskrete Versetzungsmodelle können somit wesentlich zu einem vertieften Verständnis der Mechanismen beitragen, die den Spröd-duktil-Übergang kontrollieren.

Die Ergebnisse der in der vorliegenden Arbeit durchgeführten numerischen Studien und der Vergleich mit experimentellen Ergebnissen an Wolfram-Einkristallen (Riedle, 1995) liefert neue Erkenntnisse über die Rissspitzenplastizität und den Spröd-duktil-Übergang. Die Ergebnisse sind primär für Wolfram gültig, jedoch kann davon ausgegangen werden, dass sie sich zumindest auf andere Übergangsmetalle übertragen lassen. Eine wesentliche Aussage dieser Arbeit ist, dass die Rissspitzenplastizität bei tiefen Temperaturen durch die Versetzungsnukleation eingeschränkt wird. Der Mangel an aktiven Quellen verhindert die Entstehung einer zur effizienten Abschirmung des Risses ausreichenden Anzahl an Versetzungen. Bei höheren Temperaturen werden die Quellen entlang der Rissfront verstärkt aktiv und somit wird die Versetzungsmobilität der kritische Faktor für die Rissspitzenplastizität. Die in vermehrter Zahl erzeugten Versetzungen können sich nicht hinreichend schnell von der Rissspitze entfernen und verhindern somit die sofortige Nukleation weiterer Versetzungen.

Die Anwendung der diskreten Versetzungsmodelle ist nahe beim Spröd-duktil-Übergang stark erschwert wegen der großen Zahl von Versetzungen, die zur Beschreibung großer plastischer Dehnungen erforderlich ist. Darum kann in der vorliegenden Arbeit keine abschließende Antwort über die Natur des Spröd-duktil-Übergangs gegeben werden. Jedoch zeichnet es sich ab, dass die Abstumpfung der Rissspitze durch die plastische Verformung

eine große Bedeutung für den Spröd-duktil-Übergang hat. Darüberhinaus konnte durch den Vergleich von Modellvoraussagen mit experimentellen Daten geschlossen werden, dass Schraubenversetzungen nicht für die Limitierung der Rissspitzenplastizität verantwortlich sind. Für Übergangsmetalle ist bekannt, dass Schraubenversetzungen die plastische Verformung im Massivmaterial kontrollieren. In der vorliegenden Arbeit wird dennoch ein Modell vorgeschlagen, das die Rissspitzenplastizität als mikroplastische Verformung erklärt, die von Nicht-Schraubenversetzungen getragen wird.

Contents

List of Symbols	xvii
List of Tables	xix
1 Introduction	1
2 Literature	5
2.1 Dislocation generation	5
2.2 Dislocation mobility	7
2.2.1 Thermally activated motion of screw dislocations	8
2.2.2 Motion of non-screw dislocations	10
2.3 Experimental investigations of the BDT	13
2.3.1 Silicon	13
2.3.2 Nickel-Aluminum (NiAl)	14
2.3.3 Tungsten	15
2.4 Models of crack-tip plasticity	19
2.4.1 Continuum plasticity model	20
2.4.2 Distributed dislocation models	20
2.4.3 Discrete dislocation dynamics models	22
3 Modeling of crack-tip plasticity	27
3.1 Elastic dislocation interaction with the crack	28
3.2 3D dislocation dynamics model	29
3.2.1 Discretization of dislocations	29
3.2.2 Numerical treatment of dislocation motion	33

3.2.3	Dislocation nucleation	35
3.3	2D dislocation dynamics model	40
3.3.1	Crack-tip blunting	41
3.3.2	Computer experiment	42
4	Fracture toughness in the transition regime	45
4.1	Influence of dislocation mobility	46
4.1.1	Source position	46
4.1.2	Activation energy and stress exponent	46
4.1.3	Lattice friction	49
4.1.4	Screw dislocation mobility	50
4.2	Influence of dislocation nucleation	51
4.2.1	3D model	51
4.2.2	2D model	55
4.3	Crack-tip blunting	56
4.4	Continuum model of the brittle-to-ductile-transition	57
5	Discussion	63
5.1	Low-temperature regime	63
5.1.1	Loading rate dependence	63
5.1.2	Predeformation	66
5.2	Semi-brittle regime	69
5.2.1	Quantitative comparison	69
5.2.2	Rate dependence and crack-tip blunting	71
5.2.3	Scaling behavior	72
5.3	Brittle-to-ductile transition	78
5.4	Summary	81
5.5	Criticism of the applied methods	82
5.5.1	2D discrete dislocation model	82
5.5.2	3D discrete dislocation model	83
5.5.3	2D continuum plasticity model	84
5.6	Outlook	84

6	Conclusions	86
A	Peach-Koehler force on a screw dislocation in front of a crack	97
B	Validation of the line-tension correction	99
C	Zusammenfassung (in German)	101
C.1	Einleitung	101
C.2	Modell der Rissspitzenplastizität	102
C.2.1	Versetzungsentstehung	103
C.2.2	Rissabstumpfung	105
C.3	Ergebnisse	105
C.4	Diskussion	106
C.4.1	Tieftemperaturbereich	106
C.4.2	Halb-spröder Bereich	108
C.4.3	Spröd-duktil-Übergang	109
C.5	Zusammenfassung	110

List of Symbols

Roman (and italic) letters

(bold characters represent vectorial quantities)

A	Proportionality constant in velocity law [Equation (2.10)]
B	Phonon drag coefficient
\mathbf{b}	Burgers vector
b	amount of Burgers vector
C	real constant
d_{c-s}	separation of crack tip and dislocation source
E	Young's modulus
F_0	total free energy to overcome the Peierls barrier at zero applied stress
\mathbf{f}_{PK}	Peach-Koehler force
\mathbf{f}_{fric}	lattice friction force on a dislocation
\mathbf{f}_{tot}	total force on a dislocation
ΔG	activation free enthalpy for dislocation glide (also “activation energy”)
g^{\max}	maximum of angular shear stress distribution around a crack tip
J	J-integral
K	stress intensity
K^{app}	applied stress intensity
K^{crit}	fracture toughness
k^{crit}	critical local stress intensity of a sharp crack tip
\hat{k}^{crit}	critical local stress intensity of a blunted crack tip
k^{tip}	local stress intensity at a crack tip
L_{min}	minimum discretization length in the 3D simulation
m	stress exponent
N^{dis}	total number of dislocations
Q_{dis}	activation energy for dislocation motion
r	cylindrical coordinate (radius)

r_{ZI}	radius of the zone of instability around a crack tip
r_{elast}	radius of the elastic zone around a crack tip
T	temperature
T_{BDT}	brittle-to-ductile transition temperature
U_{BDT}	activation energy for the brittle-to-ductile transition
v_{dis}	empirical law for dislocation velocity
v_{screw}	velocity of screw dislocations in bcc materials

Greek letters

γ	fit parameter for line tension correction
ε	strain tensor
$\dot{\varepsilon}$	strain rate
σ	stress tensor
μ	shear modulus
ν	Poisson ratio
Θ	cylindrical coordinate (angle)
τ	resolved shear stress
τ_{crack}	stress associated with loaded crack tip
τ_{fric}	lattice friction stress
τ_{image}	image stress
τ_{t}	stress associated with line tension

List of Tables

2.1	Parameters for screw dislocation mobility	10
2.2	Empirical data for edge dislocation mobility	11
2.3	Parameters for non-screw dislocation mobility	12
2.4	Material parameters for tungsten	12
2.5	Blunting slip systems in bcc structures	19

Chapter 1

Introduction

Failure of structural elements is not only a technical and economical problem, but also exposes the life and health of people to risks. Material failure can occur by fatigue or by mechanical overloading which results either in plastic failure or in fracture. Plastic failure occurs after a period of plastic deformation, in which mechanical work is done on the structural element. Since deformed parts can be detected and exchanged at regular service times, plastic failure is comparatively easy to handle from a technological point of view.

Brittle fracture, in contrast, is characterized by the absence of macroscopic plastic deformation prior to failure. Cleavage therefore occurs abruptly when a critical load is exceeded. Since no significant plastic deformation occurs, no significant amount of mechanical work is done. Brittle fracture is commonly found in materials of great strength or hardness and good temperature resistance.

Fracture can thus be said to be a competition between shear breakdown of the crack tip, which leads to plastic deformation and slows down or even stops crack propagation, and the breaking of chemical bonds between the atoms at the crack tip, which results in cleavage (Rice and Thomson, 1974). The result of this competition, *i.e.* cleavage or plastic failure, depends on material properties and thus the nature of the chemical bonds between the atoms (Eberhart, 2000).

Some materials, as for example transition metals, steels, and semiconductor crystals, exhibit a two stage behavior: at low temperatures or high loading rates they show brittle fracture, whereas at high temperatures or low loading rates they are capable of deforming plastically. Most transition metals, for example, show a temperature regime where they behave in a completely brittle manner, and a temperature regime where they behave in a completely ductile manner. In-between both regimes a usually gradual *brittle-to-ductile transition* (BDT) takes place. This transition regime, where catastrophic failure is preceded by

significant plastic deformation, is called *semi-brittle* regime [see any textbook on Materials Science or Fracture, for example Courtney (1999) or Domke (1994)].

To gain information on the BDT, the toughness of a material is tested under various conditions, such as temperature, loading rate, microstructure, crystallographic orientation, composition, specimen geometry, environment, etc. The Charpy impact test, for example, yields the energy absorption of specimens with a blunt notch [see for example Courtney (1999) or Domke (1994)]. More conclusive data is gained from three- or four-point-bending tests on specimens with a sharp pre-crack, from which the geometry-independent fracture toughness can be determined (Domke, 1994).

From a physical point of view, the most conclusive data is gained from experiments where the load on a specimen with a sharp pre-crack is transmitted to the crack-tip region as a well defined stress intensity. The specimen geometry can be such that the stress intensity stays constant when the crack advances (constant K specimen). In other geometries the stress intensity may either decrease or increase upon crack advance. Three- or four-point bending specimens are examples of geometries where the stress intensity increases if the crack advances. Crack advance therefore usually occurs in an instable manner. To get conclusive data, the test conditions should be such that the stress intensity is increased with a constant rate. The rate of increase in stress intensity is hereafter called *loading rate*. To exclude complicating effects from grain boundaries, the test material should be single crystalline.

Compared with the conditions under which “technical” materials are used, these testing conditions are of course highly idealized. However, the testing under such idealized conditions allows general conclusions about the nature of the BDT to be drawn. If these conclusions fit together and yield a consistent model of the BDT, this model can be extended to describe more realistic systems such as polycrystalline material.

Such idealized conditions are also the basis of theoretical approaches to describe crack-tip plasticity and the BDT. These descriptions have to take into account effects on various length and time scales. Close to the crack tip, where the stresses and the stress gradients are high, the conditions can only be described correctly on the atomic level. In the immediate vicinity of the crack tip the behavior of single dislocations is of great importance. Finally, continuum descriptions are best used to capture the entire plastic zone around the crack tip, which can have extensions of millimeters.

The great strength of atomistic models is that they are self-contained in the sense that no other information than that on the interatomic potentials needs to be provided and a large variety of results can be gained from these simulations. However, they are restricted to the simulation of fast and localized processes, and therefore usually do not predict macroscopic quantities. Models on larger scales, in contrast, must incorporate information about pro-

cesses on smaller scales in an averaged sense. Therefore they require the use of a number of model parameters which are not always well-defined. An advantage, especially of continuum models, is that they predict macroscopic quantities, which can immediately be compared with experimental results.

This work focuses on the intermediate scale between the atomistic and the continuum description. Crack-tip plasticity is described on the basis of the dynamical evolution of a population of single (discrete) dislocations. The model employed here is kept as simple as possible, to allow for the description of length and time scales that are usually treated with continuum models. This model is the basis of a numerical simulation scheme which is used to investigate crack-tip plasticity in its two aspects, namely the nucleation of dislocations at or near the crack tip and their propagation away from the crack.

The aim of this work is to close the gap in the understanding of the mechanisms limiting the plastic deformation of the crack-tip region of bcc metals. In spite of the many efforts made to understand crack-tip plasticity and the BDT, it is still not clear whether the difficult activation of plasticity (dislocation nucleation) causes the brittleness of some materials, or rather the slow rates at which plastic deformation takes place (dislocation mobility). In the picture of dislocations these ideas are formulated as dislocation nucleation control of plasticity, or accordingly as dislocation mobility control. To reach the proposed aim, a purely dislocation mobility controlled model is set up. The consistency of the predictions of this model with experimental data from Riedle (1995) is investigated. Where inconsistencies are found, the model is refined in iterative steps.

The model material chosen in this work is tungsten. This transition metal crystallizes in the bcc structure and exhibits a BDT in a temperature regime that is suitable for experimental investigations (Riedle, 1995). At liquid nitrogen temperature, tungsten cleaves in an almost perfectly brittle manner and gives fracture toughnesses close to values predicted by atomistic simulations (Gumbsch, 1995; Riedle et al., 1996). Moreover, the elastic behavior of tungsten is almost isotropic. Compared to silicon, which has been extensively studied as a model material for the BDT (St.John, 1975; Brede and Haasen, 1988; Samuels and Roberts, 1989), tungsten, a representative of brittle metallic materials, is much better suited to serve as model material for other structural materials which exhibit a BDT.

In the following chapter, an overview of the current literature on plasticity in the vicinity of crack tips and the BDT is given. An experimental study on tungsten single crystals is referred to as the basis for quantitative comparisons. Thereafter a model of crack-tip plasticity is developed and described in detail. This model is transformed into a two-dimensional (2D) simulation scheme, which allows the macroscopic quantity fracture toughness to be calculated. The dependence of fracture toughness on loading rate and temperature as well

as several model parameters is studied next. The process of dislocation nucleation is then further investigated with a three-dimensional (3D) simulation scheme. The results of these numerical studies are presented and then compared with experimental data. The conclusions that can be drawn from these comparisons are discussed in detail. The BDT itself is investigated using a simple, but illustrative, continuum model.

Chapter 2

Literature

The BDT is of fundamental interest for engineers and has therefore been the subject of a plentitude of experimental and theoretical investigations. This chapter gives a comprehensive overview of this work. Since the question whether the BDT is determined mainly by dislocation mobility or rather by dislocation nucleation is still under discussion, a special focus is set on these two issues before the actual BDT is discussed.

A list of materials ordered with respect to increasing brittleness, *e.g.* polymers, noble metals, transition metals, intermetallics, ceramics, and ionic crystals, reflects also the increasing strength of the chemical bonds between the respective compounds, *i.e.* van-der-Waals, metallic, covalent, and ionic bonds. Thus, the transition metals do not merely represent a transition in the periodic table of elements, but also a transition from purely metallic to increasingly covalently bonded materials. As a general rule it can be stated that the stronger the bonds between the atoms (or molecules) are, the more the material will restrain from plastic deformation.

2.1 Dislocation generation

During the early stages of plastic deformation of a well annealed material an increase in dislocation density is generally observed. Consequently, dislocation sources must be activated inside the material. For example, new dislocations can nucleate at grain boundaries or other imperfections. The multiplication of pre-existing dislocations, for example by the formation and operation of Frank-Read sources, is another mechanism for the generation of new dislocations. For an overview of dislocation sources see for example Chapter 20 in Hirth and Lothe's (1992) textbook.

The mechanisms by which dislocations are generated in the vicinity of a crack tip are not yet identified with satisfying certainty. Currently experimental *in-situ* and *ex-situ*

investigations, like TEM (Baither et al., 1999; Zielinski et al., 1995), X-ray topographic imaging (Michot, 1997), or positron annihilation spectroscopy (Hansen et al., 1997; Wider et al., 1998), are conducted to obtain a better understanding of these processes. Until now these efforts have only led to qualitative models of how dislocations are generated at crack tips.

Atomistic modeling efforts showed that homogeneous dislocation nucleation seems possible in fcc crystals like copper or in solid state noble gases (Zhou et al., 1996; Abraham, 1997; Abraham et al., 1997; Zhou et al., 1998), whereas for metals with bcc structure – and also materials with covalent bonding of the atoms – the activation energy for homogeneous nucleation is higher than the Griffith energy (Rice and Thomson, 1974; Schoeck, 1991), *i.e.* the energetic barrier for crack advance. Hence, homogeneous nucleation cannot occur in such materials, which consequently are labeled *inherently brittle*. These investigations showed that the early stages of dislocation nucleation are controlled by processes on the atomic length and time scale.

A Kosterlitz-Thouless-type instability has been proposed by Khantha et al. (1995) to explain the overcoming of the high activation barrier for homogeneous nucleation. Other authors have proposed morphological imperfections in the crack front, like ledges, jogs, or kinks, as the preferred sites of dislocation nucleation (Zhou and Thomson, 1991a; Xu et al., 1995) [see also the experimental work of Roberts et al. (1994)].

In silicon single crystals cracks can be produced with a high level of perfection (Michot, 1997), whereas it is evident that cracks in silicon polycrystals and in single- as well as polycrystalline metals always show a comparatively large amount of imperfections. The stress field at the crack tip is changed by such imperfections in a way that locally mode-II and mode-III stress components appear, which facilitate the generation of dislocation nuclei (Zhou and Thomson, 1991a; Xu et al., 1995). Michot (1997) has reported that massive dislocation emission was triggered at the instant when an externally created dislocation intersected the crack front.

In conclusion, it is stated that homogeneous nucleation of dislocations occurs in inherently ductile materials, like for example copper and gold (Rice and Thomson, 1974; Zhou et al., 1996; Abraham, 1997). In materials that exhibit brittle behavior under certain conditions homogeneous nucleation seems unlikely (Rice and Thomson, 1974). However, it can be assumed that imperfections in the crack front serve as dislocation sources in all materials (Zhou and Thomson, 1991a; Xu et al., 1995).

2.2 Dislocation mobility

Since the velocity of dislocations is difficult to measure experimentally, data on the temperature and stress dependence of dislocation velocity is scarce. Direct observations of dislocation velocity can be obtained from etch pit experiments (Schadler, 1964; Prekel et al., 1968) or X-ray topographic imaging (George and Michot, 1993; Loyola de Oliveira and Michot, 1994) or sometimes even *in-situ* transmission electron microscopy (Alexander et al., 1987; Gottschalk et al., 1993). However, these techniques require a tremendous effort to obtain data on a sound statistical basis. Moreover, not all materials can be investigated with every method. Due to the difficulties in receiving reliable experimental data on dislocation mobility by direct observation most theories on dislocation mobility rely on investigations of the deformation velocity $\dot{\epsilon}$ as a function of the resolved shear stress τ , the temperature T , and the density of mobile dislocations ρ_m . These quantities are connected by the Orowan law

$$\dot{\epsilon} = b\rho_m v_{\text{dis}}(\tau, T), \quad (2.1)$$

where b is the Burgers vector and $v_{\text{dis}}(\tau, T)$ is the average dislocation velocity. It is noted here that the density of mobile dislocations is not straightforwardly obtained from experimental investigations, but must be determined *post mortem*.

Experimental investigations in soft materials showed a linear stress dependence of the dislocation velocity, see for example (Nadgornyi, 1988; Kocks et al., 1975, Chapter 3). This is expressed in the form

$$v_{\text{dis}}(\tau) = \frac{b\tau}{B}, \quad (2.2)$$

where the phonon drag coefficient B is only slightly dependent on temperature. Since the dislocation velocity is directly proportional to the resolved shear stress, Equation (2.2) is usually called viscous glide law. A generalization of this linear law is to describe the dislocation velocity to be proportional to some power of the stress, see for example (Nadgornyi, 1988; Kocks et al., 1975, Chapter 3).

In many materials, such as bcc metals, semi-conductors, and intermetallic phases, the deformation rate $\dot{\epsilon}$ and thus also the dislocation velocity, increase strongly with temperature up to the so-called *athermal temperature*. Above this temperature dislocation velocity is widely temperature independent, whereas below this temperature dislocation velocity is regarded as being thermally activated (Schoeck, 1965; Nadgornyi, 1988; Kocks et al., 1975, Chapter 4) with some activation energy Q . Thus, dislocation velocity is expressed in the Arrhenius-type form

$$v_{\text{dis}}(T) \sim \exp\left(-\frac{Q}{k_B T}\right), \quad (2.3)$$

where k_B is Boltzmann's constant.

In bcc metals, large differences are found in the activation energies for screw and non-screw dislocations. These large differences are commonly explained by the threefold splitting of the screw dislocation's core onto three possible slip planes of $\{110\}$ -type (Hirsch, 1960; Vitek, 1974; Seeger and Šesták, 1978; Seeger, 1981), which results in a high Peierls barrier to dislocation motion. This Peierls barrier is overcome in a thermally assisted manner. A resolved shear stress that is pushing the dislocation in a certain direction can be considered as effectively lowering and thus facilitating the thermally activated overcoming of this barrier.

In the present work only the conservative motion of dislocations, *i.e.* *dislocation slip*, is considered. This slip requires only the breaking of atomic bonds in the dislocation core, but no long range material transport such as diffusion.

In the following the thermally activated motion of screw dislocations in bcc crystals is described in detail. Then the focus is laid on the motion of non-screw dislocations in bcc metals.

2.2.1 Thermally activated motion of screw dislocations

A thermodynamic treatment of dislocation motion (Schoeck, 1965; Kocks et al., 1975, Chapter 4), where the periodic Peierls barrier is regarded as a periodic sequence of obstacles, showed that the activation energy Q should be viewed as a stress dependent activation free enthalpy ΔG . The stress dependence of this activation free enthalpy is written as (Kocks et al., 1975, Equation (43w) therein)

$$\Delta G(\tau) = F_0 \left[1 - \left(\frac{\tau}{\tau_P} \right)^n \right]^p, \quad (2.4)$$

where F_0 is the total free energy to overcome the Peierls barrier in the absence of an applied stress ($\tau = 0$) and τ_P is the Peierls stress, *i.e.* the stress to move the dislocation at $T = 0$. In general two stress exponents n and p are necessary to describe the stress dependence of the activation free enthalpy correctly.

This yields a velocity law for screw dislocations in bcc metals of the form

$$v_{\text{screw}}(\tau, T) = v_0 \exp \left(-\frac{\Delta G(\tau)}{k_B T} \right). \quad (2.5)$$

The proportionality factor v_0 itself is a function of the attempt frequency at which a dislocation tries to overcome the Peierls barrier and, at low temperatures, the length of the mobile dislocation segment.

The dependence on the length of the mobile dislocation segment is obtained from models which consider the overcoming of the Peierls barrier to occur locally by the formation of kink pairs (Hirsch, 1960; Seeger, 1981). This process is thermally activated, such that its

probability increases with temperature. At low temperatures a comparatively high stress is required to enable the formation of a kink pair. Once such a kink pair is generated, it spreads out quickly under the high stress, dragging the dislocation into the next Peierls valley. Since the expectation value of the generation of a single kink pair is proportional to the length of the screw dislocation segment, longer segments exhibit a higher velocity. At higher temperatures the stress level and thus the mobility of the kink pair is lower. Hence, the average distance between kink pair generation sites, which is independent of the segment length, determines the dislocation velocity. Details of the kink pair model can be found for example in the work of Seeger (1981).

The temperature dependence of the flow stress is derived by inserting Equations (2.5) and (2.4) into Equation (2.1) and solving with respect to τ , which yields

$$\tau(T) = \tau_P \left[1 - \left(\frac{T}{T_{\text{at}}} \right)^{1/p} \right]^{1/n}, \quad (2.6)$$

where

$$T_{\text{at}} = \frac{F_0}{C k_B}, \quad (2.7)$$

and

$$C = \log \left(\frac{\dot{\epsilon}}{b \rho_m v_0} \right). \quad (2.8)$$

The quantity C is a dimensionless constant, which lies generally in the interval [20, 30] (Nadgorny, 1988).

Equation (2.6) has been fitted to experimentally determined flow stress data (Brunner, 1998) by using the Peierls stress τ_P , the athermal temperature T_{at} , and the stress exponents p and n as fitting parameters. The experimental data and the best fit is shown in Figure 2.1, the fitting parameters are listed in Table 2.1. The fit curve describes the experimental data very well up to temperatures of $T = 500$ K. Beyond this temperature deviations occur that are attributed to the simplified form of Equation (2.6), which does not take into account the change in the mode of dislocation motion. The theory of Seeger (1981) describes the motion below the so-called ‘‘knee’’ temperature as being controlled by the formation of kink pairs, whereas above the knee temperature it is controlled by the motion of kink pairs which are easily formed. An application of this theory yields a better description of the flow stress curve, even beyond the knee temperature (Brunner, 1998), but the simple mathematical representation used here is more suited for the scope of this study, in which the velocity law (2.5) will not be used for such high temperatures.

Because the fitting parameters in this model all have a physical meaning, the consistency of the fit can be verified. The activation enthalpy matches well with data obtained from mechanical spectroscopy (Ziebart, 1986). The Peierls stress and the athermal temperature are consistent with other experimental flow stress data (Argon and Maloof, 1966).

Figure 2.1: Experimentally determined yield stress τ_{yield} of single crystalline tungsten from (Brunner, 1998). The data points are connected with the best fit of Equation (2.6), the according fit parameters are listed in Table 2.1.

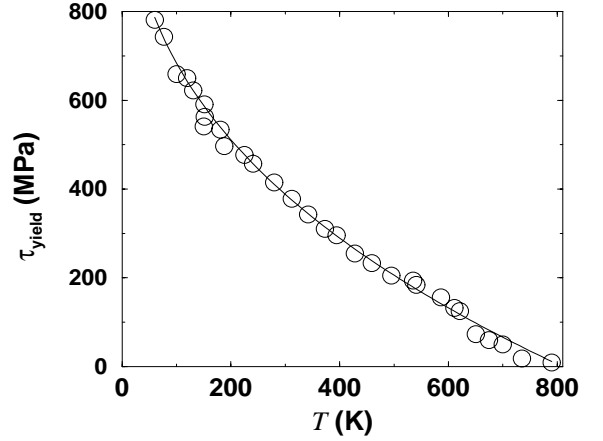


Table 2.1: Material parameters for screw dislocation mobility. The athermal temperature is denoted by T_{at} , v_0 is the proportionality constant with units of a velocity, τ_P is the Peierls stress, p and n are stress exponents, F_0 is the total free energy to overcome the Peierls barrier at zero stress, which is calculated from Equation (2.7) with a value of $C = 26$. The quantity v_0 is the proportionality constant with units of a velocity.

T_{at} (K)	τ_P (GPa)	p	n	F_0	v_0 (m/s)
810	1.3	2.8	1.0	1.8	3000

Cross-slip

It has been proposed (Seeger and Šesták, 1978) that cross-slip occurs easily in bcc structures due to the threefold splitting of the core of a dislocation at rest (Vitek, 1974). Since the dislocation core of such a stationary dislocation is equally distributed onto three slip planes, the dislocation core can concentrate and move on the most highly stressed slip plane. This holds also if dislocation motion occurs by kink pair formation.

At stresses close to the Peierls stress, when the thermal activation of dislocation motion is of subordinate importance, the dislocation core is almost planar on the plane of motion (Schroll et al., 1998). It is not clear whether cross-slip occurs easily under these conditions. At present, no detailed theory describing cross-slip under all conditions is available.

2.2.2 Motion of non-screw dislocations

In bcc metals, the preferred Burgers vector and line direction are both of $\langle 111 \rangle$ -type. Therefore, two minima of the line energy with respect to the angle Θ between Burgers vector and line direction are found. The first minimum is that for screw dislocations at $\Theta = 0^\circ$, the

Table 2.2: Parameters describing the mobility of non-screw dislocations in tungsten as expressed in Equation (2.9) [after (Schadler, 1964)].

T (K)	τ_N (MPa)	m
77	425	10.5
298	308	4.8

second minimum is found at $\Theta = 70.5^\circ$. Somewhat imprecisely these dislocations are called “edge” dislocations.

The mobility of non-screw dislocations is less well investigated theoretically than that of screw dislocations. Recent atomistic simulations (Duesbery and Xu, 1998) indicate that the basic mechanisms causing dislocation motion are the same as those for screw dislocations, but that the activation energy for kink pair generation along a non-screw dislocation is considerably lower. Therefore, the mobility of non-screw dislocations is expected to be athermal already at low temperatures.

However, there is experimental evidence of a thermal activation of the mobility of 70.5° -dislocations in a wide temperature range in tungsten (Schadler, 1964) as well as in molybdenum (Prekel et al., 1968). Moreover, in these investigations temperature dependent stress exponents between 3 and 12 have been found. Schadler (1964) conducted etch-pit experiments in tungsten single crystals in which he determined the velocity of “edge” dislocations to be

$$v_{\text{edge}} = \left(\frac{\tau}{\tau_N} \right)^m, \quad (2.9)$$

with temperature dependent constants τ_N and m as reproduced in Table 2.2.

In a more general form, the velocity of non-screw dislocations is written as

$$v_{\text{dis}}(\tau, T) = A \left(\frac{\tau}{\tau_0} \right)^{m(T)} \exp \left(-\frac{Q_{\text{dis}}}{k_B T} \right), \quad (2.10)$$

where τ_0 and A are temperature independent. The temperature dependence of the stress exponent is assumed to be of the form (Prekel et al., 1968)

$$m(T) = \frac{\alpha}{T} + \beta, \quad (2.11)$$

with two fit parameters α and β , which are evaluated from the stress exponents given in Table 2.2. Originally, Prekel et al. (1968) proposed a stress exponent inversely proportional to the temperature, however, the data on tungsten cannot be described by such a simple form. Therefore a constant value β is added to inter- and extrapolate from the experimental data points.

Table 2.3: Material parameters for non-screw dislocation velocity. The quantity A is the proportionality constant with units of a velocity, α and β serve to describe the temperature dependence of the stress exponent m , and Q_{dis} is the apparent activation energy for non-screw dislocation motion.

α (K)	β	A (m/s)	Q_{dis} (eV)
592	2.81	3.23×10^{-9}	0.323

Table 2.4: Material parameters for tungsten taken from (Pearson, 1956), E is Young's modulus, μ is the shear modulus, ν is Poisson's ratio, a is the lattice parameter, and $b = a/2 \langle 111 \rangle$ is the amount of Burgers vector.

E (GPa)	μ (GPa)	ν	a (nm)	b (nm)
388.7	152.7	0.29	0.3159	0.274

From the knowledge of the stress exponent m and the normalization stress τ_N at two different temperatures, an apparent ¹ activation energy for dislocation motion is estimated. To accomplish this, the stress exponent m and the normalization stress τ_N are inserted into Equation (2.10), which gives two equations for the two different temperatures. These equations are solved with respect to the activation energy Q_{dis} and the proportionality constant A . Table 2.3 lists all parameters for non-screw dislocation velocity as derived here.

In general, the understanding of dislocation mobility in bcc transition metals is still unsatisfactory. One of the reasons is that it is not clear which elementary step of dislocation motion requires a thermal activation. Especially the mobility of non-screw dislocations is not understood well enough to give a thermodynamical description. Therefore, in this work, an empirical approach is chosen and the critical parameters are always varied in a sensible range to give an estimate of the errors arising from the uncertainties in dislocation mobility.

For completeness, the material parameters of tungsten used in this work are listed in Table 2.4. Since tungsten is elastically isotropic, the knowledge of the shear modulus and Poisson's ratio is sufficient to describe dislocation motion.

¹Empirical activation energies are in the following referred to as "apparent" activation energies to distinguish them from thermodynamically well-defined activation energies or activation enthalpies.

2.3 Experimental investigations of the BDT

The distinction between brittle and ductile material behavior is generally not strict. Between the brittle and the ductile regime, a more or less well-developed semi-brittle transition regime can be found in most transition metals. Ceramics and semi-conductors under certain conditions reveal a very abrupt change from completely brittle to ductile behavior (St.John, 1975; Brede and Haasen, 1988; Samuels and Roberts, 1989). Intermetallic phases may even show a two stage BDT with two distinct steps of increase in fracture toughness at two different temperatures (Bergmann and Vehoff, 1995).

For single crystals, the BDT temperature can be defined as the temperature at which the specimens fail by yielding rather than by final fracture. This BDT usually coincides with a significant increase in the energy absorption and the fracture toughness. Another way of determining the BDT temperature is to expose a specimen to a temperature gradient and start a running crack at the cold side of the specimen. The position where the crack arrests can be classed with a BDT temperature.

A large part of the experimental investigations of the BDT has been reported for silicon (references see below), for which high-purity, dislocation-free single crystals are available commercially. Other investigations have been conducted on Fe-Si steel (Lii et al., 1990; Marsh and Gerberich, 1994; Zielinski et al., 1995), refractory metals (Lii et al., 1990; Huang and Gerberich, 1994; Riedle, 1995; Gumbsch et al., 1998), intermetallics (Bergmann and Vehoff, 1995; Booth and Roberts, 1997; Ebrahimi and Shrivastava, 1998), and ceramics (Kim and Roberts, 1994). In the following an overview of this experimental work is given with respect to its impact on the present study.

The actual BDT temperatures depend strongly on experimental details as specimen size and loading rate. Moreover only small amounts of alloying elements, dopants, or impurities change the BDT temperature significantly. Therefore only rough figures for the BDT temperatures for the different materials are given in the following, except for the case of tungsten, where the results shall be compared with model predictions below.

2.3.1 Silicon

Extensive studies on the BDT in silicon have been performed by several groups. In general, it was found that silicon fractures by cleavage at low temperatures (room temperature) and that the fracture toughness stays almost constant up to the BDT temperature ($T_{\text{BDT}} \approx 600 \text{ K}$ to 1200 K), from where it rises steeply. The BDT usually occurred within a very narrow temperature range of typically 5K (St.John, 1975; Brede and Haasen, 1988; Samuels and Roberts, 1989), such that the BDT temperature could be determined without ambiguity.

The actual BDT temperatures reported by various groups, see for example (St.John, 1975; Brede and Haasen, 1988; Samuels and Roberts, 1989; Hirsch et al., 1989; Warren, 1989; Hsia and Argon, 1994), strongly depend on the specimen geometry and the content of dopants and thus vary over a large range. However, it was found by all groups that the BDT temperature T_{BDT} scales with the loading rate, see for example the overview of Roberts et al. (1994, Figure 1 therein). The BDT temperature is correlated with the loading rate \dot{K} , *i.e.* the rate of increase of the stress intensity factor, by an Arrhenius-type law of the form

$$\dot{K} \sim \exp\left(-\frac{U_{\text{BDT}}}{k_B T_{\text{BDT}}}\right). \quad (2.12)$$

This allowed an apparent activation energy for the BDT to be determined by plotting the data in an Arrhenius plot. It is found that the apparent activation energies for the BDT as determined by the various groups all fall into the same range (Roberts et al., 1994). The content of dopants in silicon was reported to affect the BDT temperature itself as well as its loading rate dependence, and thus the apparent activation energy for the BDT (Brede and Haasen, 1988). This is of special interest because the doping of silicon has a pronounced influence on dislocation mobility, whereas it should not change the morphology of the crack front and, therefore, also leave the dislocation nucleation probability unchanged. Moreover, it was reported that the activation energy for the BDT agrees very well with that for dislocation motion (Samuels and Roberts, 1989; Serbena and Roberts, 1994).

Experiments on predeformed silicon specimens (Warren, 1989) revealed distinct differences compared to the dislocation-free specimens. The predeformation caused a semi-brittle regime to occur, where the fracture toughness rose slowly from the low temperature value. A BDT was not found within the temperature range of the investigation, from which it was concluded that predeformation raises the BDT temperature.

Loyola de Oliveira and Michot (1994) reported that the stress intensity at which the first dislocations are emitted changes with the perfection of the crack front. The authors could suppress dislocation emission right up to the BDT temperature by increasing the perfection of the crack front.

2.3.2 Nickel-Aluminum (NiAl)

Experimental investigations of the intermetallic phase NiAl revealed a BDT in polycrystals (Bergmann and Vehoff, 1995; Ebrahimi and Hoyle, 1997) as well as in single crystals (Vehoff, 1992; Bergmann and Vehoff, 1995; Ebrahimi and Shrivastava, 1998). The investigations of Shrivastava (1997) and Ebrahimi and Shrivastava (1998) on NiAl single crystals were performed on double notch tensile specimens. Since NiAl exhibits a pronounced semi-brittle regime, the BDT temperature could only be determined with some arbitrariness. However,

Ebrahimi and Shrivastava (1998) stated that within the semi-brittle regime a transition from small-scale to large-scale yielding occurs. These authors define small-scale yielding as the limitation of the plastic zone to the immediate vicinity of the crack tip, whereas in large scale yielding the whole diameter of the notched tensile specimen is deformed plastically. The fracture toughness was reported by the authors to increase rapidly from the onset of small-scale yielding, which was used as a definition of the BDT.

Ebrahimi and Shrivastava (1998) plotted the temperature at a constant level of fracture toughness K^0 against the loading rate in an Arrhenius-type plot. From this plot the apparent activation energies $U(K^0)$ for crack-tip plasticity were determined. It was found that these apparent activation energies increased monotonously with the level of fracture toughness K^0 . At the highest fracture toughness investigated the apparent activation energy for crack-tip plasticity agreed with that for bulk plasticity. The transition in the activation energy coincided with the transition from small-scale to large-scale yielding.

Ebrahimi and Shrivastava (1998) argue that slip localization on only a few active slip planes and consequent crack initiation by slip decohesion is responsible for fracture in the semi-brittle regime in single crystalline NiAl, but especially also in polycrystalline NiAl (Ebrahimi and Hoyle, 1997). Since an enhanced cross-slip probability reduces the slip localization and leads to an improved ductility of the material, Ebrahimi and Shrivastava (1998) suggest that the low apparent activation energy for the BDT is associated with that for cross-slip.

Investigations of mode-III loaded crack tips with atomic force microscopy by Göken et al. (1995) revealed that under their testing conditions in fact a single slip band is activated. These authors studied the dislocation distribution on this slip plane and found that it corresponds to an inverse pile-up. Ochmann and Vehoff (1995) investigated the fracture toughness and BDT temperature of NiAl bi-crystals as a function of the separation of crack tip and grain boundary. They found that the fracture toughness is larger for smaller separations. Ochmann and Vehoff (1995) also conducted computer simulations where discrete dislocations are emitted from a crack tip. These dislocations form a pile-up in front of the grain boundary that is considered impenetrable to dislocations. Ochmann and Vehoff (1995) could reproduce their experimental results if they allowed dislocation re-nucleation behind the grain boundary to occur. If they considered the grain boundary as impenetrable barrier to dislocation motion, their model predictions disagreed with the experimental results.

2.3.3 Tungsten

A thorough investigation of the BDT in tungsten single crystals has been performed by Joachim Riedle at the *Max-Planck-Institut für Metallforschung* in Stuttgart/Germany (Riedle, 1995). This author has conducted three-point bending tests on specimens with either a sharp

pre-crack or a blunt notch. The influence of temperature and loading rate on the BDT have been investigated as well as the influence of predeformation, crystallographic orientation, and the notch radius. At the lowest temperature of $T = 77$ K all tested specimens showed an almost perfectly brittle behavior, followed by a semi-brittle regime at intermediate temperatures, where the fracture toughness increased, and finally by the BDT that coincided well with a maximum in fracture toughness.²

The experimental procedure and details of the results have been published (Riedle, 1995; Riedle et al., 1996; Gumbsch et al., 1998), nevertheless a short review is provided here, because a comparison of the numerical results with experimental data is aimed at. The influence of the crystallographic orientation on the fracture toughness and the BDT temperature is shown in Figures 2.2 A and B. The specimens with a $\{110\}$ -type fracture surface showed generally a higher fracture toughness than those with a $\{100\}$ -type fracture surface. At low and intermediate temperatures fracture tests with two different crack front orientations revealed that on both fracture surfaces the specimens with a $\langle 001 \rangle$ crack front gave a higher fracture toughness than those with a $\langle 011 \rangle$ crack front. However, the BDT temperature of the specimens with $\langle 001 \rangle$ -type crack front was about 100 K higher, whereas the influence of the orientation of the fracture surface on the BDT temperature was comparatively small.

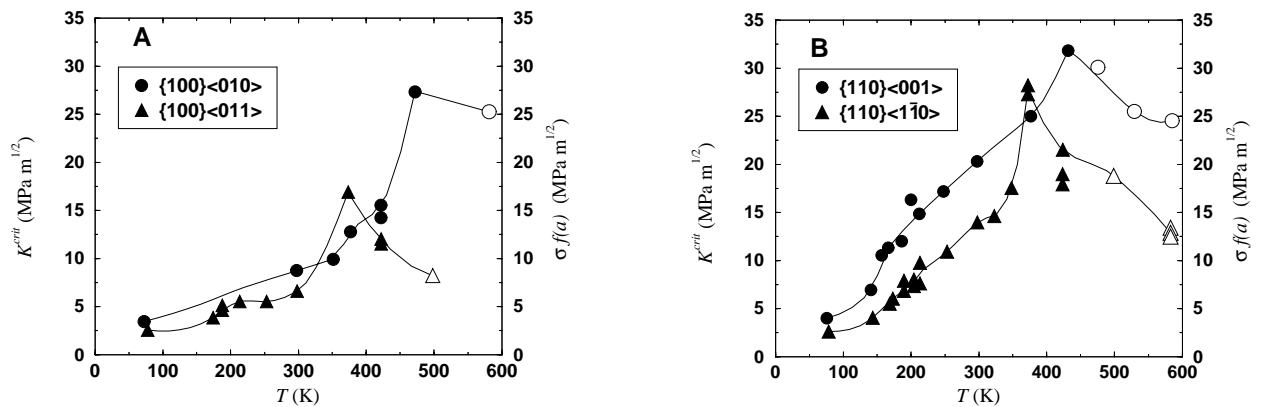


Figure 2.2: Fracture toughness as a function of temperature T and crystallographic orientation of the crack. Crack planes of $\{100\}$ -type are shown in part A, crack planes of $\{110\}$ -type in part B. Filled symbols represent fracture toughnesses (left axis), open symbols represent stresses at failure (right axis), which are normalized by a value proportional to the square root of the crack length a for compatibility with the fracture toughness scale. Lines are shown only as a guide for the eye. The data is taken from (Riedle, 1995).

²The fracture toughness given in the referenced work is the stress at failure normalized by a function of the crack length. Therefore, a maximum in fracture toughness is found, whereas other measures like the J -integral would show a continued increase in fracture toughness, because the amount of plasticity increases monotonously with temperature.

Some fracture surfaces were etched *post mortem* to reveal traces of dislocation activity (Riedle, 1995; Gumbsch et al., 1998). Electron-microscopy images of two $\{100\}$ -type fracture surfaces broken at liquid nitrogen temperature and room temperature are reproduced in Figures 2.3A and B. Besides the crack front – and a small-angle grain boundary in Figure 2.3A – several lines emanating from the crack front are clearly seen in both figures. These lines result from etch-pits, which mark the positions of steps on the fracture surface. These steps on the surface can be produced by irregularities in the moving crack front or by screw dislocations penetrating the surface. Whether these lines are pile-ups of screw dislocations or slip lines of just a few screw dislocations penetrating the fracture surface is not entirely clear. In any case, the density of these lines is much higher in the specimen fractured at room temperature than in the specimen fractured at liquid nitrogen temperature. The fracture toughness of the room temperature specimen was about 30% higher, but the testing did not reveal a significant deviation from linear elastic behavior. These results were interpreted as a limited amount of small scale plasticity occurring at room temperature in the immediate vicinity of the crack front (Gumbsch et al., 1998).

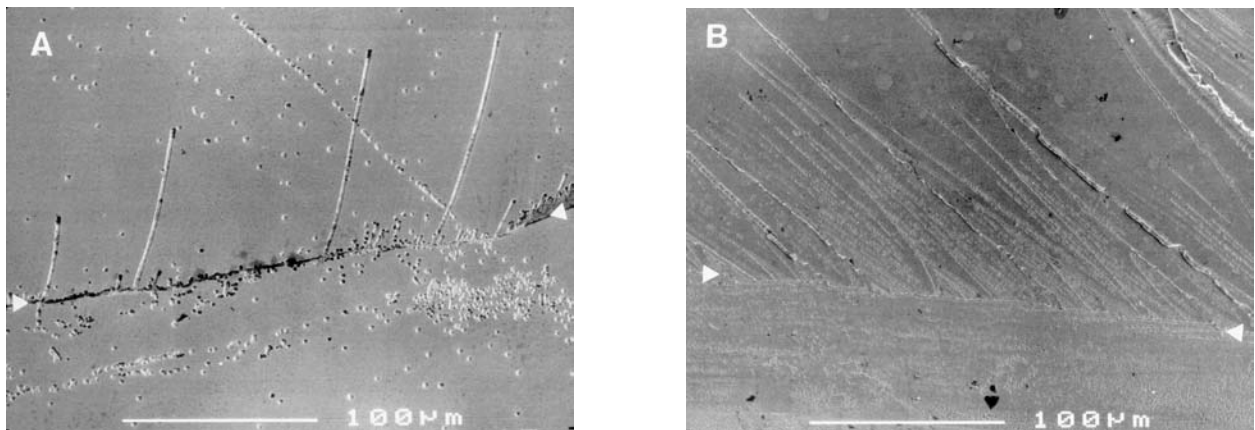


Figure 2.3: Fracture surface of a $\{100\}\langle 010\rangle$ crack produced at 77K (A) and 298K (B). The surface has been etched to make traces of dislocation activity visible. The triangles mark the position of the crack front before final fracture occurred. These images are taken from (Riedle, 1995).

Important information on the thermal activation was gained by an investigation of the loading rate dependence of the fracture toughness and the BDT temperature. The results of these experiments are plotted in Figure 2.4. The BDT temperature was found to increase with the loading rate, while the fracture toughness at the BDT remains approximately constant.

A further key experiment for the understanding of the mechanisms controlling the BDT was the investigation of predeformed specimens. These specimens have been predeformed up to 10% plastic strain under compression at a temperature of $T = 678$ K before they have

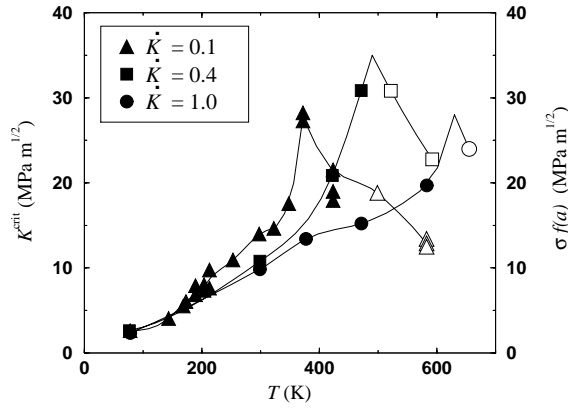


Figure 2.4: Dependence of the fracture toughness K^{crit} on the loading rate \dot{K} . Rest of assignments as in Figure 2.2. The data is taken from (Riedle, 1995).

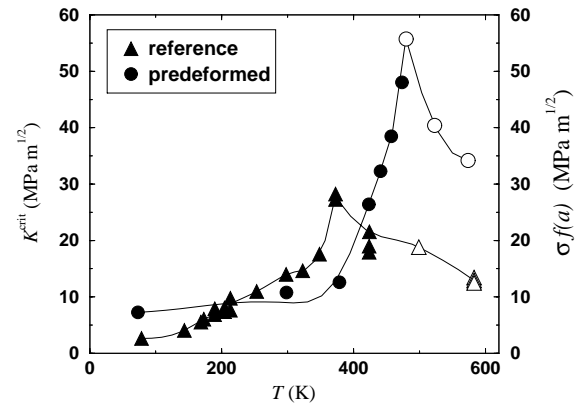


Figure 2.5: Temperature dependence of the fracture toughness of predeformed material compared with that of undeformed reference material. Rest of assignments as in Figure 2.2. The data is taken from (Riedle, 1995).

been studied in the same way as the undeformed material. The resulting fracture toughness as a function of temperature is compared with the fracture toughness of undeformed reference specimens in Figure 2.5. Predeformation increased the fracture toughness at low temperatures. Beyond a certain temperature the toughening effect of predeformation vanished and the fracture toughness was found to be even lower than in the undeformed state. Predeformation also shifted the BDT towards higher temperatures.

Further experiments were conducted on specimens with a blunt notch instead of a sharp pre-crack. Beyond the BDT the notched specimens failed approximately at the same loads as the specimens with sharp pre-cracks. At all temperatures below the BDT temperature the notched specimens exhibited higher fracture toughnesses than the pre-cracked ones. However, the influence of the notch was such that the fracture toughness was increased by an almost constant amount at all temperatures. Therefore, the shape of the curve through the data points did not change notably by the variation in the crack radius.

Later it will be seen that the blunting slip systems are of great interest for the description of crack tip plasticity. Therefore Table 2.5 gives a list of the blunting slip systems, the Schmid factor calculated from the far-field stress, and the inclination angle of the slip plane. This table is compiled from the more complete overview in the appendix of Riedle's (1995) thesis.

Table 2.5: The blunting slip systems for each low indexed crack system. The data is compiled from Riedle (1995, Appendix).

crack system	blunting slip system	Schmid factor	inclination angle
(100)[001]	(110)[1 $\bar{1}\bar{1}$]	0.27	45°
	(110)[1 $\bar{1}\bar{1}$]	—” —	—” —
	($\bar{1}\bar{1}0$)[$\bar{1}\bar{1}\bar{1}$]	—” —	—” —
	($\bar{1}\bar{1}0$)[$\bar{1}\bar{1}\bar{1}$]	—” —	—” —
(100)[011]	(01 $\bar{1}$)[111]	0.2	90°
	(01 $\bar{1}$)[1 $\bar{1}\bar{1}$]	—” —	—” —
	(01 $\bar{1}$)[$\bar{1}\bar{1}\bar{1}$]	—” —	—” —
	(01 $\bar{1}$)[$\bar{1}\bar{1}\bar{1}$]	—” —	—” —
	(21 $\bar{1}$)[1 $\bar{1}\bar{1}$]	0.27	35.3°
	($\bar{2}\bar{1}\bar{1}$)[$\bar{1}\bar{1}\bar{1}$]	—” —	—” —
(011)[100]	(0 $\bar{1}\bar{1}$)[111]	0.29	90°
	(0 $\bar{1}\bar{1}$)[$\bar{1}\bar{1}\bar{1}$]	—” —	—” —
	(0 $\bar{1}\bar{1}$)[1 $\bar{1}\bar{1}$]	—” —	—” —
	(0 $\bar{1}\bar{1}$)[$\bar{1}\bar{1}\bar{1}$]	—” —	—” —
	(011)[11 $\bar{1}$]	0.23	0°
	(011)[$\bar{1}\bar{1}\bar{1}$]	—” —	—” —
(011)[0 $\bar{1}\bar{1}$]	(211)[$\bar{1}\bar{1}\bar{1}$]	0.4	54.7°
	($\bar{2}\bar{1}\bar{1}$)[$\bar{1}\bar{1}\bar{1}$]	—” —	—” —

2.4 Models of crack-tip plasticity

Parallel to the experimental investigations theoretical efforts are currently in progress to explain the BDT on a physical basis. Numerical continuum plasticity approaches are concerned with the rate sensitivity of crack-tip plasticity. Several groups are engaged in analytical modeling of the BDT by distributed dislocation models, where instead of single (discrete) dislocations ensembles of dislocations or dislocation densities are considered. Finally, numerical methods are used to describe the dynamical evolution of a population of discrete dislocations in the vicinity of a crack tip in two and three dimensions.

2.4.1 Continuum plasticity model

Continuum plasticity is well suited for implementation in finite element models. Several groups apply such methods to investigate crack-tip plasticity and crack advance in cohesive zone models, see for example the works of Needleman (1987) and Cleveringa et al. (1999). Nitzsche and Hsia (1994) have developed a very simple continuum model that shows a BDT. This model describes the time-dependent plastic (viscoplastic) material behavior around a crack tip. The rate of plastic deformation $\dot{\epsilon}$ is proportional to a power of the shear stress τ and a Boltzmann term with a thermal activation energy U , which gives

$$\dot{\epsilon} = A \exp\left(-\frac{U}{k_B T}\right) \left(\frac{\tau}{\tau_0}\right)^m, \quad (2.13)$$

where k_B is Boltzmann's constant, T is the temperature, and m is the stress exponent. The proportionality constant A has the units of a creep rate (1/s), and τ_0 is the constant normalization stress.

In the immediate vicinity of the crack tip the very high stresses lead to rapid plastic relaxation. In the case of power-law material behavior, this changes the stress singularity at the crack tip from a $1/\sqrt{r}$ -type to a Hutchinson-Rice-Rosengren-(HRR)-type singularity (Hutchinson, 1968; Rice and Rosengren, 1968). The HRR description generalizes the conventional stress intensity approach. The stress in the vicinity of a crack tip is proportional to the J -integral and decreases with a power of the distance r to the crack tip, which can be different from $-1/2$.

However, a stress intensity based analysis can still be conducted if the elastic zone concept of Suo et al. (1993) is applied: A circular region around the crack tip is restricted to purely elastical behavior. This model will be adapted to tungsten and described in more detail in Section 4.4.

Nitzsche and Hsia (1994) found that this model shows a sharp BDT at a well-defined temperature. The sharpness of the BDT is not quite as high, but still comparable to the BDT observed in experiments on silicon single crystals (St.John, 1975; Brede and Haasen, 1988; Samuels and Roberts, 1989). The scaling behavior of the BDT temperature with loading rate follows an Arrhenius-like equation, and the apparent activation energy for the BDT is the same as that for the viscoplastic deformation.

2.4.2 Distributed dislocation models

Khantha-Pope-Vitek model

According to Khantha et al. (1995), the experimentally observed strong increase in fracture toughness with temperature close to the BDT cannot be explained by a thermally activated

process, since such processes are more gradual in nature. Especially, it is doubted by these authors that dislocation multiplication exclusively caused by Frank-Read sources can result in a sudden, strong increase in dislocation density. The authors also find it “difficult to imagine that the process of dislocation production could differ very much depending on whether a pre-existing crack is present or absent in the material” (Khantha et al., 1994). In the present work, mechanisms will be presented that provide an explanation why dislocation generation in the highly stressed crack-tip region should in fact be different from dislocation generation at the moderate and homogeneous stresses in the bulk.

Consequently, the model of the BDT developed by Khantha, Pope, and Vitek (KPV) incorporates only intrinsic material properties and does not rely on detailed nucleation mechanisms, like Frank-Read sources or dislocation nucleation at crack tips (Khantha, 1994; Khantha et al., 1994; Khantha et al., 1995). Instead, the KPV model is based on a stress-aided Kosterlitz-Thouless-type dislocation instability (Kosterlitz and Thouless, 1972), which results in a sudden increase in dislocation density. Following Kosterlitz and Thouless (1972) KPV assume that dislocation loops of the size of a few Burgers vectors can nucleate spontaneously by thermal activation. Usually, these loops collapse under their own line tension on short time scales. However, these loops also lead to a plastic polarizability of the material. The existence of the small dislocation loops thereby facilitates the generation of larger loops. In the presence of external stresses, this *cooperative dislocation screening* eventually develops into an massive dislocation generation at increasing temperature. This instability is interpreted as a *dislocation-mediated melting transition* (Kosterlitz and Thouless, 1972; Khantha et al., 1994). This mechanical melting point of the material is reached at temperatures lower than the thermodynamical melting point only if very high external stresses are present (Khantha et al., 1994).

The KPV model describes the development of this dislocation instability in the presence of an external stress field. KPV derive an analytical expression for the critical temperature and stress level, above which the instability occurs. For stress levels of about 1 GPa the so-calculated critical temperatures are of the order of two thirds of the melting temperature (Khantha et al., 1994). This model, moreover, predicts a very sharp transition from brittle to ductile material behavior, as it is found for example in dislocation-free silicon.

A strain rate dependence of the BDT temperature and the fracture toughness in the semi-brittle regime is introduced into the KPV model by considering the dynamics of dislocation dipoles in the vicinity of a crack tip (Khantha, 1994). This dynamical behavior is assumed to be self-similar in its time evolution. The velocity of the dislocations is described by an empirical stress power law, similar to Equation (2.10). This approach leads to a Arrhenius-like scaling of the BDT temperature with strain rate, as commonly found in experimental investigations (see above). Since this model requires the motion of screw dislocations in the

far-field stress, the predicted activation energy for the BDT should be equal to that for bulk plasticity, which is not the case for transition metals, as discussed in Section 5.2.3.

Conventional models

In a more conventional framework Ashby and Embury (1985) considered the influence of the local dislocation density around the crack tip on the shielding behavior. They found that an increased dislocation density yields a lower BDT temperature. However, in this work the authors neglected the influence of the increased yield strength of the material. Experiment shows (Gumbsch et al., 1998) that predeformation shifts the BDT temperature to higher values. This may override the toughening effect of the increased dislocation density.

Hähner and Stamm (1995) included the dynamical development of the dislocation population around the crack tip into their model. They derived an analytical expression for the BDT temperature that depends exclusively on physically well-defined quantities. These authors predict a BDT temperature proportional to the difference of the Gibbs free energies for dislocation emission from the crack tip and that for thermally activated dislocation glide. The BDT temperature moreover depends in a complicated fashion on the strain rate and the yield stress of the material. Within their model Hähner and Stamm (1995) can describe the influence of cold working, *i.e.* predeformation, and irradiation damaging on the BDT temperature at least qualitatively. However, the use of this model is problematic for single crystals.

2.4.3 Discrete dislocation dynamics models

While the models introduced at this point focus strongly on the BDT temperature, the class of discrete dislocation dynamics (DDD) models, which are presented in the following, are more suited to gain new insight in the mechanisms that determine fracture toughness in the semi-brittle regime. Moreover, the DDD methods are capable of incorporating more details of the dislocation nucleation process.

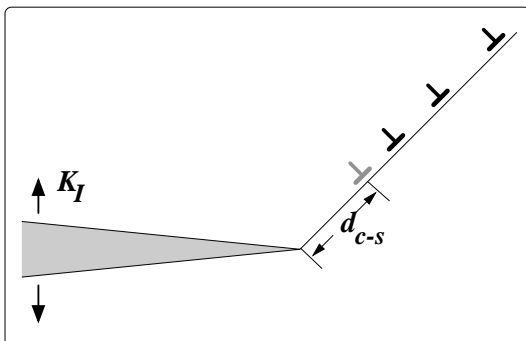


Figure 2.6: Crack loaded with stress intensity $K_I = K$. A freshly nucleated dislocation is drawn in gray at the location d_{c-s} of the dislocation source. The shielding dislocations, which move away from the crack tip, form an inverse pile-up.

In these mesoscopic models of crack-tip plasticity, dislocations are regarded as singular sources of stress, which are embedded in an infinite elastic medium with a semi-infinite crack. In the following, a 2D model will be introduced, where all dislocations are straight lines parallel to the crack front (Figure 2.6). In cases that require a fully 3D investigation, the dislocation line must be discretized into smaller segments. In any case, the total force³ \mathbf{f}_{tot} acting on dislocation i (or dislocation segment i) at position \mathbf{x}_i is written as the sum (Lin and Thomson, 1986)

$$\mathbf{f}_{\text{tot}}^{(i)} = \mathbf{f}_{\text{Kd}}(\mathbf{x}_i) + \mathbf{f}_{\text{dd}}(\mathbf{x}_i) + \sum_{j \neq i} \mathbf{f}_{\text{dd}'}(\mathbf{x}_i, \mathbf{x}_j) + \mathbf{f}_{\text{fric}}, \quad (2.14)$$

where \mathbf{f}_{Kd} is the force due to the applied stress intensity K , \mathbf{f}_{dd} is the image force due to the presence of the free crack surfaces, $\mathbf{f}_{\text{dd}'}$ is the interaction force with every other dislocation, and \mathbf{f}_{fric} is the constant lattice friction force. The image force is always directed towards the crack tip, while the applied force \mathbf{f}_{Kd} can be attractive or repulsive with respect to the crack tip depending on Burgers vector, line direction, and position of the dislocation. The lattice friction is always opposite to the direction of motion, such that it always reduces the driving force on the dislocation. However, it cannot give rise to a negative driving force.

If a dislocation exerts a crack closing stress on the crack tip, it is called a shielding dislocation, otherwise it is called an anti-shielding dislocation. The shielding or anti-shielding character of a dislocation depends on its Burgers vector and line direction, as well as on its position relative to the crack tip. In 2D models, it is possible to introduce a local stress intensity k_I , which describes the stress field close to the crack tip, taking into account the crack opening or closing stress of the dislocation population (Thomson, 1986). The far-field stress beyond the plastic zone is not affected by the dislocation population, therefore it is still described by the applied stress intensity K_I . The dimensionless shielding factor $s \equiv k_I/K_I$ is a quantitative measure for the amount of shielding associated with the dislocation population.

To perform a dynamical simulation, the total force acting on each dislocation must be transformed into a dislocation velocity. Usually the time scale of the simulations is large enough such that inertia can be neglected. Thus, the dislocations instantaneously possess the velocity according to the appropriate velocity law [Equations (2.5) and (2.10)]. Once the velocity of all dislocations is known their equations of motion are integrated numerically. The integration generally requires several additional rules to be obeyed in order to avoid dislocation passing or intersection processes that may occur due to the finite time step.

³Vectorial quantities in two or three dimensions are denoted with bold Roman letters, their amount is expressed by the same letter set in Italics, for example $f = |\mathbf{f}|$.

Because dislocation nucleation at crack tips takes place on length and time scales below that of DDD models, this process must also be described by special rules. The most common rule (Roberts, 1996) is also applied in this work as described in Section 3.2.3.

2D-DDD models

Most applications of DDD methods in two dimensional fracture problems are based on the work of Lin and Thomson (1986), who derived analytical formulations of the force on a straight dislocation of arbitrary Burgers vector in a medium with a semi infinite crack in the presence of an arbitrary dislocation population (Lin and Thomson, 1986; Thomson, 1986). A number of groups have used their ideas to develop simulation schemes for crack tip plasticity. For example, Zacharopoulos et al. (1997) investigated the development of dislocation microstructure in the vicinity of a mode-III loaded crack; Xin and Hsia (1997) studied the influence of multiple slip planes on the BDT; and Pippan and Riemelmoser (1995) used the 2D-DDD method to study crack tips under cyclic loading and the appearance of striations.

The most extensive use of the 2D-DDD method has been made by the Oxford group around Hirsch, Samuels, and Roberts, who mainly studied the BDT in silicon (Samuels and Roberts, 1989; Hirsch and Roberts, 1989; Hirsch et al., 1989; Roberts et al., 1993; Roberts et al., 1994; Roberts, 1996), but also in other semi-conductors (Serbena and Roberts, 1994; Kim and Roberts, 1994) and in TiAl (Booth and Roberts, 1997). The authors succeeded in modeling a sharp BDT in silicon by assuming that dislocation nucleation is suppressed up to loads close to the critical stress intensity and by assuming dislocation nucleation from discrete nucleation sites (Roberts, 1996).

Since the main part of the present work is based on a 2D-DDD study of crack tip plasticity, details of this method are provided in the next chapter.

3D-DDD models

In a 3D dislocation model it is necessary to describe the shape and the dynamics of curvilinear dislocations. The curved line is approximated by a succession of piecewise straight segments. In general, it is favorable to approximate a curved line by segments of mixed character with arbitrary angles between neighboring segments. In this work, instead, dislocation lines are discretized into pairwise orthogonal segments of pure edge and screw character, which simplifies the moving of a dislocation line considerably. This method has been proposed and first used by Kubin et al. (1992).

3D-DDD methods have been applied to investigate the formation of a dislocation microstructure (Kubin et al., 1992; Devincre and Kubin, 1994; Kubin et al., 1995; Zbib et al.,

1998), the rate dependence of plastic deformation in bcc metals (Tang et al., 1998), the dislocation microstructure under a nano-indent (Fivel et al., 1997; Fivel et al., 1999), and work-hardening in thin metal films (Schwarz and Tersoff, 1996; Schwarz, 1997; Hartmaier, Nix, Gumbsch and Arzt, 1999).

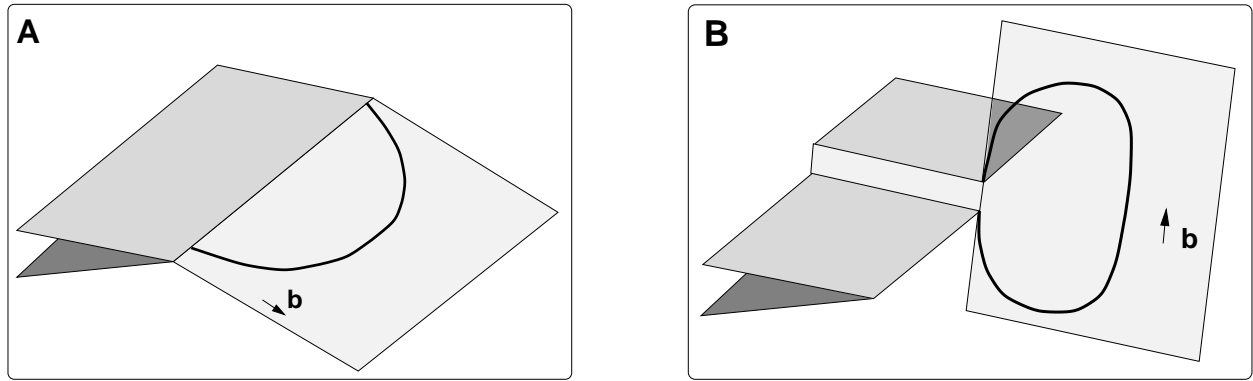


Figure 2.7: The two different types of nucleation sites. A: Dislocation emission on slip systems containing the nominal crack front, B: dislocation nucleation on oblique slip systems.

A 3D-DDD study of crack-tip plasticity has been conducted by Devincre and Roberts (1996). The authors of this work compared the dynamics and shielding behavior of blunting dislocation half-loops, where the crack front is contained within the slip plane (Figure 2.7A), with that of non-blunting dislocation loops, where the crack front cuts the slip plane in a single point (Figure 2.7B).

Devincre and Roberts (1996) find that the shielding of non-blunting dislocations is quite strong, but localized around the source. Moreover, dislocation emission in the non-blunting configuration is more difficult, because a complete loop must be generated (compared to a half-loop in the blunting configuration). Furthermore, the dislocation in the non-blunting configuration surrounds the crack tip, and consequently is partially situated in regions where the resolved shear stress of the mode-I crack is low. Therefore, the nucleation rate of a non-blunting source is rather low. In contrast, dislocation nucleation in the blunting configuration occurs more easily and with a higher rate, because the expansion of the half-loops takes place on a slip plane where the stress field of the mode-I crack is high. The shielding of blunting sources spreads more homogeneously along the crack front. But since the dislocations on blunting slip planes are more mobile and leave the crack-tip region easily, the amount of shielding of blunting sources is smaller than the local shielding around a non-blunting source. Therefore, Devincre and Roberts (1996) conclude that a high density of non-blunting sources along the crack front is necessary to give a high *and* homogeneous shielding.

To limit calculation time Devincre and Roberts (1996) used a rather coarse discretization length in their study. Therefore the shape of their dislocation loops and consequently the

ratio of parts with edge or screw character is not represented realistically, as shown in Section 3.2.1. This leads to inaccuracies in the dislocation velocity and nucleation rate. Furthermore, the shielding of the crack depends strongly on the shape of the dislocations.

The investigations with 2D-DDD models published to date all assume easy and homogeneous dislocation nucleation at the crack tip, only Roberts (1996) studied dislocation nucleation at discrete sites along the crack front in an approach that will be pursued further in this work. The temperature dependence of the activity of different dislocation sources as well as the influence of crack-tip blunting have been disregarded so far. Furthermore, the dependence of crack-tip plasticity and the BDT on the different model parameters and the form of the dislocation velocity law has not been investigated in detail. 3D-DDD studies on crack-tip plasticity are limited to the work of Devincre and Roberts (1996), which is subject of certain shortcomings as detailed above.

Chapter 3

Modeling of crack-tip plasticity

In this chapter, the dynamics of dislocation populations in the vicinity of a crack tip is studied. The model developed here is valid for single crystalline metals with bcc structure. Later the model predictions will be compared with experimental results on tungsten single crystals. Plastic activity at the crack tip has two toughening effects. First, dislocations can shield the crack tip from the applied load, and second, dislocations can blunt the crack tip, which increases the load necessary to propagate the crack (Gumbsch, 1995). In general, dislocations that are generated at the crack tip have a toughening effect, whereas the polarization of a pre-existing dislocation population increases the load on the crack tip (Zhou and Thomson, 1991*b*).

In the course of this work numerical simulation schemes in two and three dimensions have been employed to study the dynamical development of a dislocation population in the vicinity of a loaded crack tip. The aim of this study is to verify or falsify different assumptions about the mechanisms controlling the BDT. The simulation schemes have been adapted from ideas published by different authors [2D mainly Roberts (1996), 3D mainly Devincre and Roberts (1996) and Kubin et al. (1992)].

In the following the basic ideas underlying the numerical schemes are detailed. In the first section the static interaction of dislocations with the crack tip is investigated to estimate the extension of the zone around the crack tip where dislocations at rest cannot exist. Next the implications of discretizing dislocations into small segments are discussed. The discretization of a dislocation line is necessary for a 3D treatment. The basic ideas employed here are taken from the literature (Kubin et al., 1992), only a useful length scale for the following investigations of crack-tip plasticity had to be calculated. Also new are the ideas about dislocation nucleation at ledges on oblique slip planes and their cross-slip onto blunting slip planes. The basics for the simulation scheme in 2D, which are presented afterwards, are also taken from literature. The main adaptations here were the incorporation of the explicit nucleation procedure and the inclusion of crack-tip blunting. At the end of this chapter the

”computer experiment” is explained, which will be used in the following to calculate fracture toughnesses of model materials at different temperatures and loading rates.

3.1 Elastic dislocation interaction with the crack

In a first step, the elastic interaction of a dislocation with a semi-infinite crack in an infinite isotropic medium is studied within the framework of linear elasticity. The crack is loaded in the opening mode to an applied stress intensity $K_I = K$. In-plane and out-of-plane shear components vanish, *i.e.* $K_{II} = K_{III} = 0$.

Since the attractive image force decreases as $1/r$ with the distance r to the crack tip (Lin and Thomson, 1986) and the repulsive force from the crack-tip stress field decreases as $1/\sqrt{r}$, there exists a point where both forces are in equilibrium. For a dislocation closer to the crack tip than this point the image forces are stronger than the repulsion. Therefore, dislocations parallel to the crack tip cannot exist in equilibrium in this zone. This gives rise to a *zone of instability* around the crack tip.

The size of the zone of instability depends on the angle between crack and slip plane. Only perfect edge dislocations are considered in the 2D model, such that the Burgers vector is always orthogonal to the crack front direction. In this case, the resolved shear stress on a blunting slip plane is simply the stress component $\sigma_{r\Theta}$ in the polar coordinates r and Θ , where r is the distance from the crack tip and Θ is the angle between slip and crack plane. This stress component is given as [see for example (Thomson, 1986, Equation (9.13))]

$$\sigma_{r\Theta} = \frac{K}{\sqrt{2\pi r}} \sin(\Theta/2) \cos^2(\Theta/2). \quad (3.1)$$

The trigonometric functions reach their common maximum $g^{\max} = 0.38$ at $\Theta = 70.5^\circ$.

The maximum extension r_{ZI} of the zone of instability is estimated under the condition that the maximum resolved shear stress

$$\tau_{\text{crack}} = \frac{k_I}{\sqrt{2\pi r_{ZI}}} g^{\max} \quad (3.2)$$

due to the local stress intensity k_I be equal to the image stress

$$\tau_{\text{image}} = \frac{\mu b}{4\pi(1-\nu)r_{ZI}} \quad (3.3)$$

due to the free surface. This yields a maximum extension of the zone of instability of

$$\begin{aligned} r_{ZI} &= \left(\frac{\mu b}{2\sqrt{2\pi}(1-\nu)g^{\max}k_I} \right)^2 \\ &= \frac{1}{8\pi(1-\nu)^2} \left(\frac{\mu b}{g^{\max}k_I} \right)^2, \end{aligned} \quad (3.4)$$

which, in tungsten, takes a value of $r_{ZI} = 4b$ for $k_I = k^{\text{crit}} = 2 \text{ MPa}\sqrt{\text{m}}$ (material parameters are given in Table 2.4). The influence of existing dislocations is included in this value, because the local stress intensity k_I is considered, in which the shielding of the dislocation population is taken into account.

3.2 3D dislocation dynamics model

A detailed analysis of dislocation emission at discrete sites requires the description of curved dislocations, which is impossible within a 2D edge-on model. In this section the manner of discretizing a dislocation line is explained and a useful discretization length for the following calculations is determined. The implications of moving dislocation segments on a regular mesh are reiterated from literature. Finally, a detailed mechanism for the nucleation of dislocations on ledges in the crack front is introduced. The primary slip plane for dislocations nucleated at such sites are non-blunting slip planes. However, only dislocations on blunting slip planes give a good shielding. Therefore a cross-slip mechanism is proposed in this work that transforms dislocations from non-blunting slip planes to blunting slip systems.

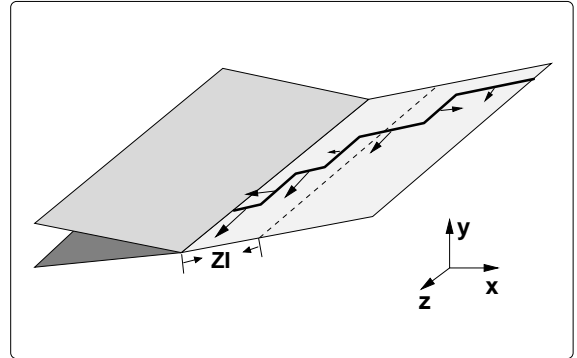
3.2.1 Discretization of dislocations

In the present work curved dislocations are discretized into a succession of pairwise orthogonal segments of edge and screw character, as described in Section 2.4.3. The minimum segment length is fixed to $L_{\text{min}} = 10b$, which corresponds approximately to twice the size of the zone of instability.

This choice is motivated by simple reasoning: If a dislocation segment shorter than the radius of the zone of instability moved along the crack front, this motion would require the generation of a segment parallel to the crack front, which would be absorbed by the crack tip immediately (Figure 3.1). This shows that the dynamical evolution of a dislocation connected with the crack tip is determined exclusively by its part outside the zone of instability. The shape of the dislocation within the zone of instability, especially the angle under which it touches the crack front cannot be calculated by continuum elasticity.

In terms of stability and efficiency of the numerical code it is desirable that a single segment threads the zone of instability. The mobility of this segment should be that of the part of the dislocation close to the perimeter of the zone of instability. Since the driving force on a dislocation segment is evaluated at the center point of the segment, the minimum segment length is chosen such that this point lies outside the zone of instability. The segments in contact with the crack front are always kept at this length.

Figure 3.1: Motion of dislocations penetrating the zone of instability (ZI). Arrows indicate direction and strength of the force on each segment. Segments parallel to the crack front are attracted to the crack tip if they lie within the zone of instability.



During the expansion of dislocation half loops the segments grow steadily. To assure the numerical accuracy of the method, it is necessary to rediscritize segments that have become too long. To accomplish this, the stress gradient along segments is controlled during each time step. If this stress gradient is larger than a predefined threshold, the segment is divided into two.

Dislocation self-interaction (line tension)

The discretization length has also a pronounced influence on the dislocation self interaction. In its analytical expression, this dislocation self interaction is written as a line integral over the dislocation line, see for example Chapter 6 in Hirth and Lothe's (1992) text book. This line integral is singular, because it is evaluated at a point on the integral path. To avoid this singularity it is necessary to introduce a cut-off radius around the point under consideration. This cut-off radius must be of finite size, because the singularity is strong enough to prevent the convergence of the integral if the cut-off radius tends to zero. Therefore, the value of the line integral, and thus the strength of the dislocation self interaction, depends on the value of the cut-off radius. Hirth and Lothe (1992) estimate a length of the cut-off radius between one and two Burgers vectors to give consistent results.

In the discretized formulation the line integral is the sum over the contributions of all segments of the dislocation line and the cut-off radius is half of the length of the segment under consideration. (The stress is always evaluated in the middle of a segment.) The minimum length of a segment is $L_{\min} = 10b$, such that the cut-off radius is always larger than $5b$ and moreover varying with the segment length. This leads to inaccuracies due to the line discretization. A solution to this problem would be to discretize a dislocation into segments of a constant length of $4b$, which is undesirable, because of its negative effect of efficiency and numerical stability. Therefore an alternative solution is chosen: The "real" self-stress at the point under consideration is estimated by evaluating the local line tension, which is assumed to be proportional to the discretization error (Fivel, 1997). This error is added to the value obtained by the elastic interaction.

The line tension τ_{lt} , and thus also the discretization error, is assumed to be inversely proportional to the local radius of curvature R (Hirth and Lothe, 1992, Chapter 6), which gives

$$\tau_{\text{lt}} = \gamma \frac{\mu b}{R} \quad (3.5)$$

where γ is the proportionality constant. If τ_{lt} is interpreted as the discretization error, the numerical value of γ depends on the minimum discretization length and has to be evaluated by a fitting procedure. In this procedure the channeling of a dislocation is simulated numerically, and the critical stress for the channeling is compared with an analytical solution of the problem. Details and results of this fitting procedure are given in Appendix B. In the following a value of $\gamma = 2 \times 10^{-5}$ is applied for $L_{\text{min}} = 10 b$.

Elastic interaction with the crack tip

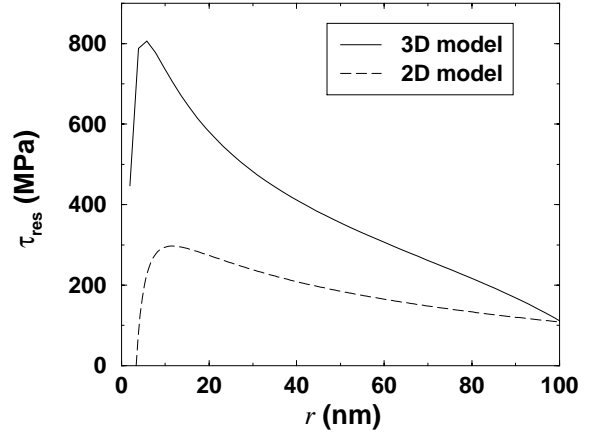
The immediate consequence of the interaction of a dislocation with a free surface is the attraction of the dislocation by the free surface. For the simple case of a screw dislocation parallel to the surface this attraction can be described by placing a dislocation of opposite Burgers vector at the same distance on the opposite side of the free surface. Therefore the force is called image force. This construction is completely parallel to the image forces arising when a charge is placed in the vicinity of a conducting surface, as described by electrostatics. For non-screw dislocations it is necessary to take additional terms into account that compensate for the hydrostatical components of the dislocation stress field (Hirth and Lothe, 1992, Section 3-4). The image force is taken into account in the numerical model by applying a force at the center of each dislocation segment. This force acts on the middle of the segment and is oriented along the normal from this point to the crack tip. The amount of the image force is approximated by (Devincre and Roberts, 1996)

$$f = \kappa \frac{\mu b}{r}, \quad (3.6)$$

where r is the distance from the middle of the segment to the crack tip and κ respectively is $1/4\pi$ for screw segments and $1/4\pi(1-\nu)$ for edge segments. For infinitely long screw segments parallel to the crack front this formulation gives the same results as the 2D description. The corrections for possible hydrostatic components of the segment stress fields are neglected here.

However, the interaction between a dislocation and a free surface does not merely give rise to an image force, but also alters the stress field of each segment. Again, this is to be seen analogously to electrostatics, where the electrical field of a charge is distorted by the presence of a conducting surface. The distortion of the elastic dislocation stress field by the free surface affects the segment-segment interaction. The error produced by neglecting this

Figure 3.2: Resolved shear stress τ_{res} on the slip plane of two dislocations in dependence on the distance to the crack tip r . One dislocation sits at position $r = 145$ nm and the second at $r = 290$ nm. Values calculated by the image force approximation in the 3D model are compared with the analytical solution in two dimensions. The crack tip is loaded with a stress intensity $K = 1 \text{ MPa}\sqrt{\text{m}}$.



three-body interaction (dislocation – crack – dislocation) is quite large already for only two dislocations. In Figure 3.2 the resolved shear stress obtained by the image force approximation are compared with those obtained from the 2D model, in which the boundary conditions are treated correctly (Lin and Thomson, 1986). For a single dislocation the differences between both methods are below 1%. Two possible solutions to solve the elastic interaction between crack-tip and dislocation to a better approximation are sketched in the following. However, the implementation of these ideas into the present 3D-DDD code has not yet been achieved.

There exist analytical solutions for the stress field of straight dislocations or dislocation loops in a half-space or even in a bicrystal (Bacon and Grooves, 1970; Barnett and Lothe, 1974; Gutkin and Romanov, 1991) and for shear dislocation loops emerging from a crack tip (Anderson and Rice, 1987; Gao and Rice, 1989). These solutions, due to their complexity, do not seem to be suited for a DDD simulation scheme.

Another method to treat free surfaces is based on the superposition of a finite element model of an elastic medium with a free surface with a 3D-DDD model that describes the evolution of the dislocation population. The theoretical foundations of such a superpositioning have been derived by Lubarda et al. (1993). The basic idea is to use the discrete dislocation description to calculate the tractions on the plane that is to become the free surface, and to compensate these tractions by appropriate point or nodal forces. The response of the medium to these point or nodal forces is calculated by a continuum description, *i.e.* the Boussinesq formula (Boussinesq, 1885; Fivel et al., 1996) or a finite element model (Fivel, 1997). Once the stress inside the medium resulting from the traction compensation is known, the additional forces on the segments arising from this stress are calculated. This traction compensation method has already been applied to study plasticity close to a planar free surface (Fivel et al., 1996; Hartmaier et al., 1998; Hartmaier, Fivel, Canova and Gumb-

sch, 1999). However, its reformulation and implementation for the crack problem requires significantly more theoretical effort.

Shielding

To determine the shielding of the crack tip by curved dislocations requires a local stress intensity at the crack tip to be calculated. This local stress intensity in general is a function of the position along the crack front. Gao (1989) has derived formulas describing the shielding due to an arbitrarily positioned and oriented, but infinitely long dislocation. A formulation for finite length dislocation segments is not derived to present. However, Devincere and Roberts (1996) provided an estimate of the local stress intensity that is based purely on the crack opening or closing stress components of the dislocation stress field at the crack tip. If the crack extends into the z -direction and the crack plane is the $y = 0$ plane, the σ_{yy} component of the stress tensor causes crack opening. Then, the local stress intensity is written as

$$k^{\text{tip}}(z) = K^{\text{app}} + \sum_{i=1}^N \sqrt{\mu b |\sigma_{yy}^i(z)|} \text{sign}(\sigma_{yy}^i(z)) \quad (3.7)$$

where N is the total number of dislocation segments and $\sigma_{yy}^i(z)$ is the yy -component of the stress field of the i -th dislocation segment taken at position z along the crack front ($i \in [1, N]$). In the limit of infinitely long segments parallel to the crack front, this formula gives the same solution as the 2D analysis of Lin and Thomson (1986).

The three problems sketched in this section, namely dislocation self-interaction, elastic interaction with the crack tip, and shielding, show that the current state of the art of 3D-DDD methods does not allow for quantitative calculations. Therefore, the 3D-DDD simulation is employed in the present work only to yield qualitative insights about the dislocation nucleation process at discrete sites along the crack front. This problem is inherently three-dimensional and thus cannot be solved within a 2D description.

3.2.2 Numerical treatment of dislocation motion

In the previous part the computation of the forces acting on the dislocations has been discussed in detail. However, to perform a dynamical simulation of the development of a dislocation population it is necessary to attribute a velocity to each dislocation, which will be discussed in the following. For the movement of dislocations on a regular grid, as performed in the simulation scheme applied here, different additional rules for the dislocation motion have to be obeyed to obtain a realistic dislocation motion. These rules are detailed at the end of this section.

The theoretical description of dislocation mobility has been provided in Section 2.2. To determine the velocity of a dislocation segment, the resolved shear stress at its middle is calculated as the ratio of the force acting on the dislocation and the dislocation's Burgers vector. The resolved shear stress is needed to evaluate Equations (2.5) and (2.10) which in turn yield the velocity of the dislocation segment. When the velocity of each dislocation segment is known, the equations of motion of all segments are integrated using a fixed time-step Newton method.

In the region close to the crack tip, where the stresses are high, the dislocation velocity can reach very high values. Since the time step must be adapted to the fastest dislocations, a very small time step is needed even though only a small portion of the segments has high velocities. To enable the use of larger time steps, the dislocation velocity is capped at a value that corresponds to a velocity of $10 L_{\min}$ per time step. The time step is controlled such that the fraction of segments whose velocity is capped does not exceed 5% of the entire dislocation population.

Dislocations are only displaced over integers of L_{\min} in one time step to avoid the creation of segments with a fraction of the minimum discretization length as neighbors of the displaced segment. To perform a dynamical simulation, on the other hand, the fractional portion of the travel distance must not be disregarded. To accomplish this, the fractions of L_{\min} of the displacement of each segment are stored and summed up for every time step. This allows for a correct description of the dynamics in a discrete space.

Individual segments cannot always move according to their velocity. For each segment it must be checked whether another dislocation segment or another kind of obstacle, like the boundary of the simulation box, lies in its path of motion. In such a case special rules for the dislocation motion must be applied.

In the case of an obstacle dislocation repulsion or annihilation can occur. Repulsion takes place if segments of equal Burgers vector and line direction come too close to each other due to the fixed time step. In this case, the segments are stopped at the minimum distance L_{\min} and usually will move away from each other in the next time step. Annihilation occurs mainly if a part of the dislocation line touches another part of the same line, as for example during the operation of a Frank-Read source. In this work the formation of junctions cannot occur, because all dislocations are located on the same slip plane. However, junction formation must be taken into account in the general case. The rules that must be obeyed are described in detail in (Devincre and Kubin, 1994; Devincre, 1996).

Different rules are needed to control the interaction of a segment with the boundary of the simulation box (domain of the simulation). In this work, dislocation segments that touch the boundary are always absorbed, *i.e.* the segment or the part of it that has passed the

boundary is deleted. In general, the boundary could also be treated as being impenetrable to dislocations. Periodic boundary conditions, instead, are problematic for discrete dislocation simulations, because no solutions for the stress field of arbitrarily oriented segments in a periodic row are available in the general case. Furthermore, dislocations leaving the simulation box on an inclined slip plane in general do not re-enter the box on the same, but on a parallel slip plane, such that the connectivity of dislocation lines is not guaranteed.

Dislocation cross-slip is also disregarded in this work. In principle the DDD method holds the possibility to treat cross-slip if the according probabilities are known (Kubin et al., 1992).

3.2.3 Dislocation nucleation

After the implications of the dynamical treatment of dislocation motion in the vicinity of a crack tip have been discussed, this section focuses on the way dislocations are generated in the course of a simulation. In this work dislocation multiplication is disregarded: new dislocations are only generated by dislocation nucleation at sources at the crack tip. In the following a rather detailed mechanism is explained of (i) dislocation nucleation at macroscopic ledges in the crack tip and (ii) cross-slip from the primary non-blunting plane onto a secondary slip plane containing the crack front. As will be seen in the discussion such a complicated nucleation mechanism is capable of combining the observations that (i) dislocations nucleate preferentially at imperfections in the crack front (Zhou and Thomson, 1991a; Xu et al., 1995; Roberts et al., 1994) and (ii) non-screw dislocations parallel to the crack front are necessary to explain the observed fracture toughnesses (see Section 5.2).

To develop a criterion for dislocation nucleation, it is assumed that a well developed nucleus in the form of a half loop is present at the nucleation site. This nucleus is realized as a “virtual” dislocation, which interacts only passively in the sense that it is subject to the applied stress field and that of all other dislocations, but its own stress field is disregarded. The consistency of the assumption that the nucleus has developed requires that it does not collapse immediately under the resolved shear stress and its own line tension. If this condition is fulfilled, the nucleation is accepted and the dislocation is transformed into a “real” one. Otherwise the dislocation nucleation is rejected.

The acceptance or rejection of a new nucleation depends crucially on the size of the nucleus. A larger nucleus expands already at a lower stress level than a smaller one. Therefore, the nucleation criterion must be validated. Since no closed theory and no detailed experimental observations of dislocation nucleation are available at present, the simulations are performed such that the first nucleation events take place at 20% of the fracture toughness. This value is consistent with experimental data on silicon single crystals (Hirsch et al., 1989). Atomistic simulations of fracture in NiAl indicate that a nucleation criterion should be based on a

criterion taking into account the shear modes of the stress intensity as well as the opening modes (Ludwig and Gumbsch, 1998). However, the only places where noticeable shear components appear under a pure K_I loading are jogs in the crack front. The shear component arising from the internal stress of the dislocation population is very small compared to k^{crit} .

Two different geometries for dislocation sources are possible, the nucleation on oblique slip planes cutting the crack front and the nucleation on slip systems that contain the nominal crack front (see Figures 2.7A and B, respectively). Dislocation nucleation on blunting slip planes is highly unlikely (Zhou and Thomson, 1991*a*; Xu et al., 1995). Yet the expansion of dislocation loops on oblique slip planes is difficult because parts of the dislocation loop with screw character have to move out of the highly stressed crack-tip region. For bcc metals screw segments are only mobile at high stresses or at high temperatures and should thus stop at a relatively short distance from the crack tip in the decaying stress field of the crack. Therefore, such sources would soon be shielded by previously emitted dislocations and cease to generate new dislocations (see also Section 2.4.3). Furthermore, a dislocation on an oblique slip plane does not contribute to the blunting of the crack tip but creates a jog of one Burgers vector height in the crack front.¹

Dislocation half loops on slip systems that contain the crack front provide an efficient shielding to the part of the crack front that is contained within the half loop. Depending on their Burgers vector, the expansion of such a dislocation half loop requires only non-screw dislocations to be moved in the far-field stress. The screw part can remain connected with the crack tip, and thus move in the highly stressed region. In the crack tip region that is swept by the dislocation half loop, the crack tip blunting is increased by one Burgers vector. Therefore these dislocations are called blunting dislocations, whereas the dislocation type on oblique slip planes is called non-blunting dislocation.

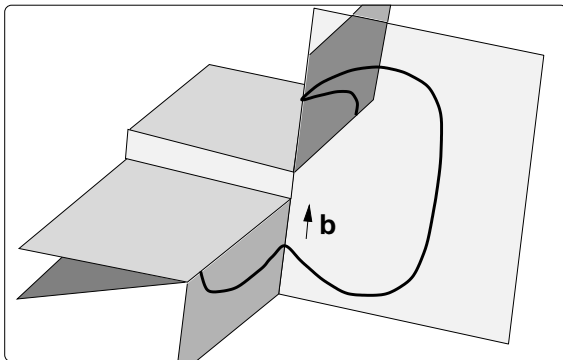


Figure 3.3: Dislocation emission in the non-blunting configuration (*cf.* Figure 2.7A) and cross slip onto slip planes containing the crack front.

As discussed in Section 2.1, dislocation nucleation occurs preferentially at imperfections like jogs in the crack front. The nucleation at jogs generates dislocations on oblique slip

¹In the case of an emission from a jog in the crack front, the jog height is reduced by one Burgers vector (Zhou and Thomson, 1991*a*).

planes. A cross-slip mechanism is proposed here that transforms a dislocation half loop on an oblique slip plane into a half loop on a slip plane containing the crack front (Figure 3.3). This model thus combines the easy nucleation at jogs with the high mobility and the good shielding potential of blunting dislocations.

A drawback of this model is that only blunting slip systems are considered as being significantly activated and responsible for the shielding and blunting of the crack tip. In a single crystal it is not clear whether such slip systems can always be found for every crystallographic orientation of the crack. However, for bcc tungsten two to six different blunting slip systems are identified for each low-indexed crack system (see Table 2.5).

Driving force for dislocation motion along crack front

It has been shown now that the proposed cross-slip mechanism is possible from a crystallographic point of view. Next the driving force for the motion of a screw dislocation to move along the crack front is calculated. The stress field of a crack can be described as that of a climb pile-up of edge dislocations with increasing density towards the crack tip (Bilby and Eshelby, 1968, Section IV.B). In this picture it is easily seen that a jog in the crack front has – at least partly – the character of a screw dislocation. This motivates already that a screw dislocation will be repelled from the jog and thus tend to change the slip plane and to move along the nominal crack front.

Quantitatively, the driving force on a dislocation close to a jog in the crack front is calculated by a 3D finite element (FE) analysis. The geometry of the finite element model is shown in Figure 3.4. Singular elements with a \sqrt{r} -displacement function, which leads to a $1/\sqrt{r}$ -interpolation for the stress (*Ansys Manual*, n.d.), have been employed around the crack tip. The jog is inclined to the crack front by 45° . This geometry corresponds to a $[011]$ -jog in the $(100)[001]$ -crack system.

A $\langle 111 \rangle$ -type screw dislocation has slip planes containing the jog as well as the nominal crack front. If a dislocation with such a Burgers vector is nucleated at the jog, it has the possibility to spread out along the jog. During this motion the screw parts of the dislocation stay connected with the crack front. Figure 3.5A shows the resolved shear stress for this dislocation on the slip plane containing the crack front. This resolved shear stress, which corresponds to the driving force for dislocation motion, is simply the shear stress component in polar coordinates, according to Equation (A.2) in Appendix A. It is seen that there exists a high driving force pushing the screw parts of the dislocation along the jog. At the points where the jog ends and the nominal crack front starts, the screw dislocation is able to cross slip onto the slip plane containing the nominal crack front. For the motion along the nominal crack front there exists again a high driving force as seen in Figure 3.5B. It is also seen that

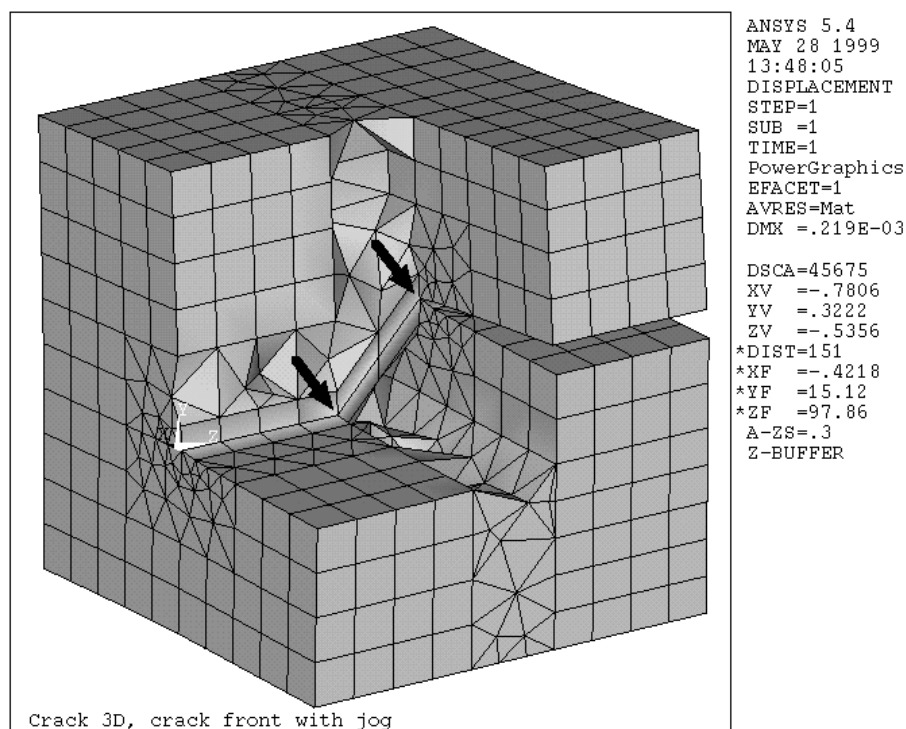


Figure 3.4: Finite element representation of a jog in the crack front. A part of the model has been removed to enable the view on the crack plane. The crack front is marked with arrows.

the driving force on the dislocation on this slip plane is amplified by the stress field of the jog (as motivated above). This shows that the jog promotes cross-slip along the nominal crack front. The probability for cross-slip onto the blunting slip plane is increasing with the the driving force on that plane. However, the cross-slip process of a dislocation in such a high and strongly varying stress field cannot be studied with a continuum model, but must be investigated by atomistic simulations.

The model introduced here transforms dislocation emitted on oblique slip planes into well shielding blunting dislocations. Since the details of the nucleation and cross slip process can only be described on an atomistic level, it is assumed in the further argumentation that dislocation half loops on blunting slip systems are available whenever the stress is such that they can expand. These dislocations need not necessarily originate from the proposed cross-slip mechanism, but may also be generated by different mechanisms. The consistency of this assumption with experimental data is discussed in Chapter 5.1.

If a dislocation half loop is nucleated at the crack front, the blunting of the crack tip is of course restricted to the region swept by the half loop. It can be shown easily that

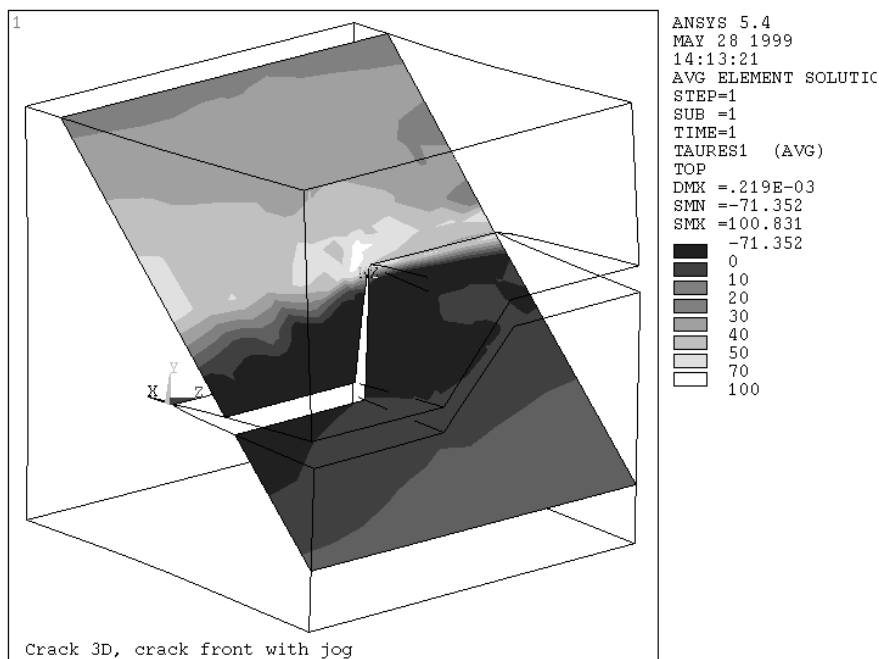
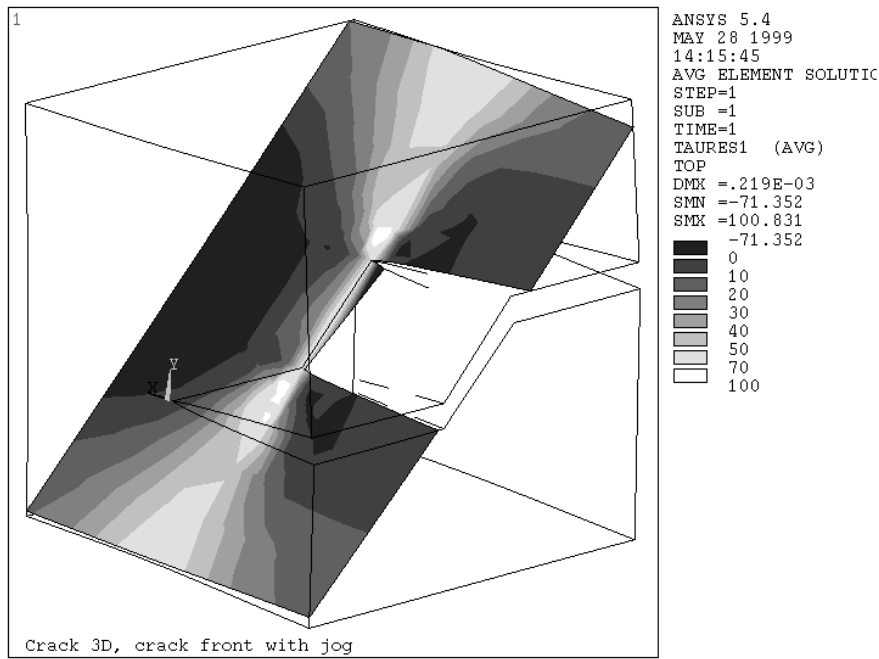


Figure 3.5: The resolved shear stress for a screw dislocation on its primary slip plane containing the jog (A) and on its secondary slip plane containing the nominal crack front (B). The values given in the color bar are in MPa.

the shielding of the crack tip is similarly limited to that portion of the crack tip which is contained within the dislocation half loop (see Figure 4.11). An anti-shielding, which decays on length scales of a few b , is found outside the half loop. Thus, brittle crack advance can still occur in regions between the nucleation sites, until the expansion of the half loops has covered the whole crack tip. This implies that there is a delay between the time when the first dislocations nucleate at discrete sites and the time when the whole crack front is shielded. This “incubation” time Δt depends on the average spacing between two nucleation sites and the mobility of the dislocation segment connected to the crack front, which itself depends on the temperature and the applied load.

The dislocation segment moving away from the crack tip travels a certain distance δ (see Figure 3.6), which depends on its velocity and the time Δt needed to bridge the gap between the discrete nucleation sites. When two expanding dislocation half loops meet, they coalesce because the segments connected to the crack front annihilate. Due to line tension a large part of the dislocation eventually becomes parallel to the crack front (Figures 3.6 and 4.9). From this stage, the system can be viewed edge-on and, thus, be captured within the 2D model.

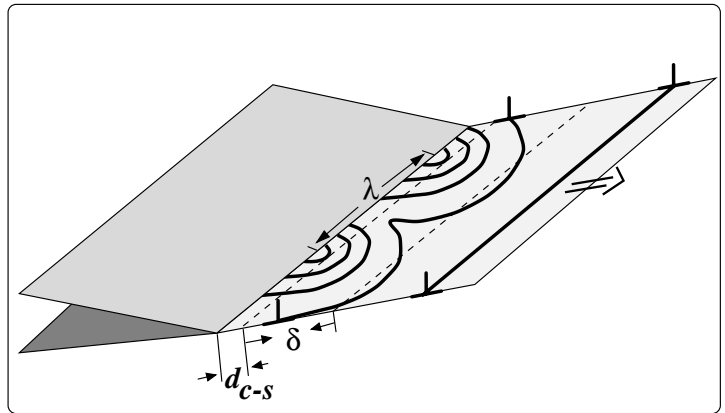


Figure 3.6: Dislocation nuclei develop at discrete sites along the crack tip. During expansion these half loops coalesce and form dislocation parallel to the crack front. The spacing between two nucleation sites is denoted by λ .

3.3 2D dislocation dynamics model

With the help of the 3D dislocation model details of the nucleation process will be investigated. Yet, to study crack-tip plasticity with many dislocations or even to calculate fracture toughnesses with this model would be far too expensive in terms of calculation times. Therefore, further simplifications are necessary to conduct “computer experiments” that can be directly compared with “real experiments”.

In the 2D model all dislocations are straight lines viewed edge-on. The details of the process of dislocation nucleation at discrete sites are implemented into the 2D model as follows: After

a dislocation has been nucleated according to the usual criterion, *i.e.* a dislocation at position d_{c-s} senses a force repelling it from the crack tip, this dislocation has to move a distance δ before its shielding is taken into account. During this time, the dislocation interaction with the other dislocations is already fully taken into account, which means that the exact shape of the dislocation line and all line tension effects are neglected. In a rudimentary form this procedure has already been proposed by Roberts (1996), who however did not take into account any temperature or loading rate dependence of δ .

3.3.1 Crack-tip blunting

The 2D model also allows crack-tip blunting to be taken into account, however, in a rather rough and qualitative manner. The conservation of the total Burgers vector requires that the notch radius of the crack tip increases about one Burgers vector with each newly generated dislocation. It is evident that a blunted crack tip cannot propagate without diffusional transport of atoms. Therefore, an atomically sharp crack is re-initiated if crack advance takes place. For a radius of curvature of the blunted crack tip below a few Burgers vectors the critical stress intensity for re-initiation increases only marginally (Gumbsch, 1995), but re-initiation becomes increasingly difficult for larger amounts of blunting. The blunting of the crack tip is proportional to the number of dislocations and, therefore, should not be neglected at elevated temperatures, where a large number of dislocations is generated.

Riedle (1995) found in his experimental investigation that the fracture toughness of specimens with a blunt notch was increased by an almost constant (temperature independent) amount compared with specimens with a sharp pre-crack. This indicates that the plastic relaxation at the crack tip is not significantly influenced by the crack-tip radius. In the 2D model, therefore, the effect of the notch can be described consistently as an increase in the critical local stress intensity for crack advance. A further influence on the dislocation nucleation and motion can be disregarded in a first approximation.

To estimate the functional dependence of the critical local stress intensity on the tip radius r , the maximum stress at a blunted crack tip is considered (Rice, 1968, Equation (161) therein)

$$\sigma_{\max} \approx \left(\frac{15}{8}\right)^{1/2} \frac{K_I}{\sqrt{r_{\text{tip}}}}. \quad (3.8)$$

The stress diverges for vanishing tip radii, leading to the concept of stress intensity. For finite radii Equation (3.8) yields finite values for the maximum stress, which should be evaluated in terms of a maximum stress criterion for crack advance. In the present work, the influence of crack-tip blunting shall only be investigated qualitatively. To accomplish this, the blunting of the crack tip is taken into account by increasing the critical local stress intensity for final

fracture with the tip radius. The radius dependent value for the critical local stress intensity \hat{k}^{crit} takes the form

$$\hat{k}^{\text{crit}}(r_{\text{tip}}) = k^{\text{crit}} \left(1 + C \sqrt{\frac{r_{\text{tip}}}{r_{\text{unit}}}} \right), \quad (3.9)$$

where C is a real constant and $k^{\text{crit}} = 2 \text{ MPa}\sqrt{\text{m}}$ is the constant value applied before. The constant $r_{\text{unit}} = 1 \text{ nm}$ is the unit distance. This formulation is chosen, because it gives the correct limit for a vanishing tip radius, *i.e.* $r_{\text{tip}} \rightarrow 0$. It will be seen later that this formulation yields a rather shallow increase of the critical local stress intensity with the tip radius. The only independent alternative formulation $\hat{k}^{\text{crit}} = k^{\text{crit}} \sqrt{r_{\text{tip}}/r_{\text{unit}} + 1}$ would shift the square root parabola to the left and thus yield a still more shallow curve.

3.3.2 Computer experiment

After all ingredients of the physical model describing crack-tip plasticity on the basis of discrete dislocations are collected, the course of the computer experiment itself shall be explained. This numerical procedure allows fracture toughness to be calculated as a function of different model parameters as for example temperature and loading rate. In the following chapter results of such calculations will be presented which will lead to new insights about the mechanisms controlling fracture toughness and the BDT.

The 2D simulations are conducted in a way mimicking the experimental procedure, *i.e.* they are started at zero applied stress intensity and without pre-existing dislocations. The stress intensity is raised at a constant rate. A constant temperature is assumed during each simulation. Besides temperature and loading rate, the simulation allows to study the influence of several model parameters on the fracture toughness, and thus to test the consistency of different assumptions with experimental findings.

The knowledge of the temperature and the resolved shear stress on the slip plane – taking into account all mutual dislocation-dislocation interactions and the interaction with the crack tip including all image effects – allows the dislocation velocities to be calculated by evaluating Equations (2.5) or (2.10), respectively. The displacement of each dislocation is obtained by integrating this velocity with respect to time, using a second order Runge-Kutta scheme (Press et al., 1986). The global time step is chosen such that its product with the average velocity of the dislocations does not exceed $10b$. This restriction is necessary to achieve a good convergence of the simulation. For dislocations that are faster than the average velocity a reduced time step is introduced such that the dislocation is not moved farther than $10b$ within the reduced time step. Several reduced time steps are performed in direct succession until their sum yields the global time step.

To reduce computing time, a superdislocation of rank 2 is formed out of three dislocations of rank 1 after the nine-th dislocation has been emitted (see Figure 3.7). This process

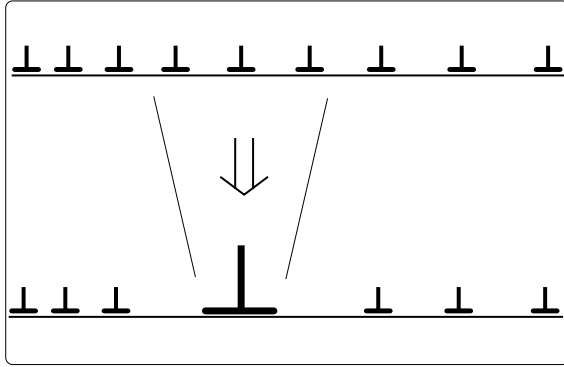


Figure 3.7: Schematic view of the formation of the first superdislocation out of three single dislocations.

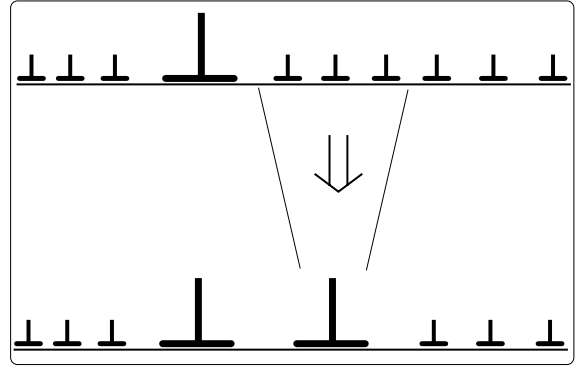


Figure 3.8: Schematic view of the formation of the second superdislocation out of three single dislocations in the presence of the first superdislocation.

is repeated such that whenever the nine-th dislocation of rank $n \in \mathbb{N}$ is created the three central dislocations are combined to one superdislocation of rank $n+1$. In the general case the dislocations of the same rank are not in direct succession, but enclose one or more dislocations of higher rank (Figure 3.8). This procedure has been described in (Roberts, 1996) and yields good results as long as the dislocations are restricted to one glide plane. If the dislocations are distributed more homogeneously in space, the formation of superdislocations may produce rather large errors in the dislocation-dislocation interaction. In the cases investigated in this work, it is a very efficient method to reduce the effective number of dislocations, without any significant loss of accuracy.

At each time step of the simulation the dislocation nucleation criterion is evaluated to decide whether or not a new dislocation is nucleated. The nucleation of shielding dislocations effectively reduces the local stress intensity at the crack tip as seen in Figure 3.9, where the local stress intensity k^{tip} is shown to be equal to the applied stress intensity K^{app} until the first dislocation is emitted and the local stress intensity drops severely. Because of this drop of the local stress intensity, further dislocation nucleation is impeded until the emitted dislocation has moved sufficiently far away from the crack tip. At a certain point the local stress intensity is again high enough such that the nucleation of a second dislocation becomes possible. After several dislocations have been nucleated, an inverse dislocation pile-up develops on the slip plane (see Figure 3.10), *i.e.* the dislocation density decreases with the distance from the crack tip.

In the time step immediately before a new dislocation is nucleated, the local stress intensity is at its maximum (Figure 3.9). This maximum increases steadily in magnitude as the applied stress intensity is raised. Finally, the local stress intensity k_I at the crack tip exceeds the critical value for fracture [$k_I^{\text{crit}} = 2 \text{ MPa}\sqrt{\text{m}}$ (Riedle et al., 1996)]. The applied stress intensity

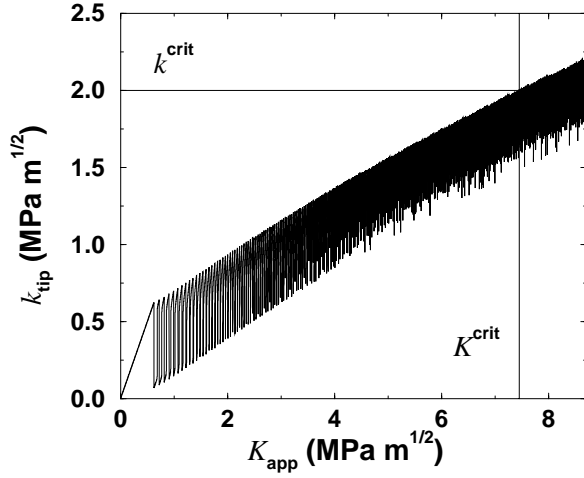


Figure 3.9: The development of the local stress intensity k^{tip} at the crack tip with the applied stress intensity K^{app} , which is raised at a constant rate of $\dot{K} = 0.04 \text{ MPa}\sqrt{\text{m}}/\text{s}$. When the local stress intensity reaches the critical value for failure k^{crit} the applied stress intensity K^{app} is equal to the macroscopic fracture toughness. The temperature for this simulation is $T = 77 \text{ K}$.

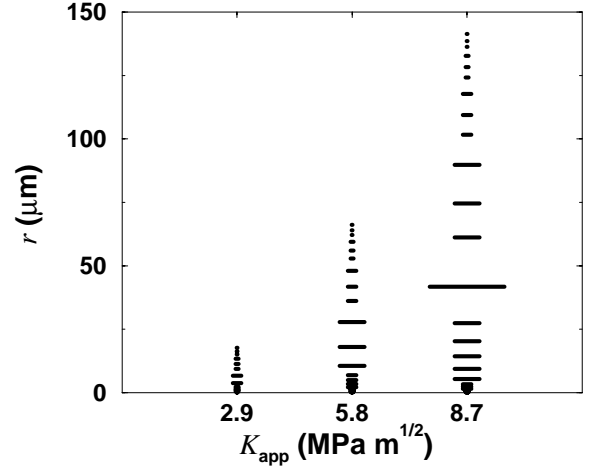


Figure 3.10: Position of the dislocations in front of a crack tip during a 2D simulation at three different loads K^{app} . Each bar corresponds to a (super-)dislocation at distance r to the crack tip, the width of the bar indicates the rank of the superdislocations, which correlates with the amount of their Burgers vector. The dislocation population forms an inverse pile-up.

at this stage defines the macroscopic fracture toughness K^{crit} (Figure 3.9). The computer experiment is terminated at this point, because it corresponds to instable crack advance. The fracture toughness and the total number of emitted dislocations as calculated by this numerical scheme for different model parameters will be presented in the following chapter and compared with experimental data in the discussion.

Chapter 4

Fracture toughness in the transition regime

In this chapter, the dependence of the numerically predicted fracture toughness on the model parameters that control dislocation mobility and dislocation nucleation are studied. In a first step, dislocation nucleation is assumed to occur easily and fracture toughness is studied as a function of dislocation mobility exclusively. Different functional forms for dislocation mobility mimicking edge and screw-type behavior are investigated. The parameters for edge-type mobility are varied in a sensible range. Furthermore, the influence of a constant lattice friction on the fracture toughness is studied. In this part of the investigation it is not tried to model the behavior of a certain material, instead the influence of a variation of the model parameters on the results is studied to draw more general conclusions.

In a second step, the model of dislocation nucleation occurring at discrete nucleation sites along the crack front is considered. From this point, the model parameters are chosen to represent single crystalline tungsten. The loading rate dependence of the saturation of nucleation sources is studied qualitatively with the 3D-DDD model. The 2D model is employed to obtain quantitative predictions of the macroscopic fracture toughness for a temperature dependent density of nucleation sites along the crack front. A loading rate dependence of the source density could not be described satisfactorily and is therefore disregarded in the 2D model. In a further step, the importance of crack tip blunting for the BDT is investigated qualitatively.

In the last section of this chapter a continuum plasticity model is applied to study the loading rate dependence of the fracture toughness and the BDT itself. The description of the large plastic strains that occur at the BDT is the domain of continuum models, whereas discrete dislocation models are suited to investigate details of the small plastic deformations of the transition regime.

4.1 Influence of dislocation mobility

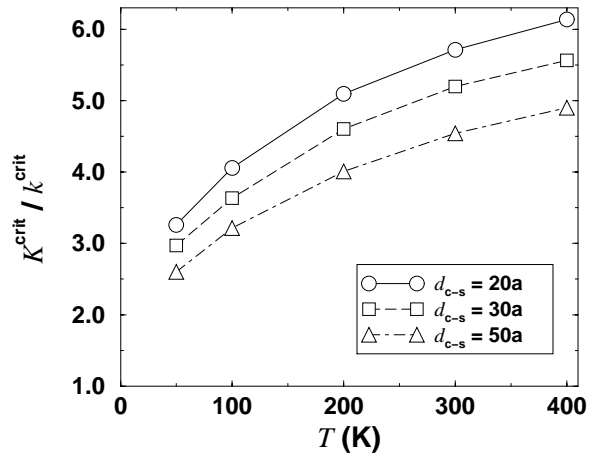
In the following calculations, dislocation nucleation has been assumed to occur quasi-homogeneously, *i.e.* the additional length that dislocations have to overcome before their shielding covers the entire crack front and is thus taken into account, has been set to $\delta = 0$. Before material specific simulations are conducted, the influence of the different model parameters on the numerical results is studied.

Throughout this chapter the plotted data points are connected with lines. These lines serve only as a visual guide and are not based on a physically motivated interpolation.

4.1.1 Source position

It has been shown in Section 3.2.3 that the distance of the dislocation source to the crack tip is not self-consistently defined within the 2D-DDD model. A distance of $d_{c-s} = 30a$ causes the first dislocation to be generated at 20% of the critical load. The influence of this parameter on the resulting fracture toughness is seen in Figure 4.1. The fracture toughness is higher for sources closer to the crack tip at all temperatures. The shape of the $K^{\text{crit}}-T$ -curves is not altered by the source spacing. For these simulations the mobility law as formulated in Equation (2.10) for edge dislocations has been employed with the parameters from Table 2.3. A loading rate of $\dot{K} = 1.0 \text{ MPa}\sqrt{\text{m}}/\text{s}$ has been assumed.

Figure 4.1: Influence of the distance d_{c-s} between dislocation source and crack tip on the relative fracture toughness $K^{\text{crit}}/k^{\text{crit}}$ at various temperatures T ; d_{c-s} is measured in lattice parameters a . The loading rate is $\dot{K} = 1.0 \text{ MPa}\sqrt{\text{m}}/\text{s}$.



4.1.2 Activation energy and stress exponent

The parameters of the dislocation mobility law, have a pronounced influence on the numerically determined fracture toughness, as well as on the shape of the $K^{\text{crit}}-T$ -curves. Figures 4.2A and B show the fracture toughness as a function of temperature for three different stress exponents and two different activation energies.

A higher activation energy merely rescales the temperature axis, as could be expected from the form of the mobility law [Equations (2.10)]. The shape of the $K^{\text{crit}}-T$ -curves is not changed by a change in the activation energy. This will be verified quantitatively and discussed in detail in Section 5.2.3.

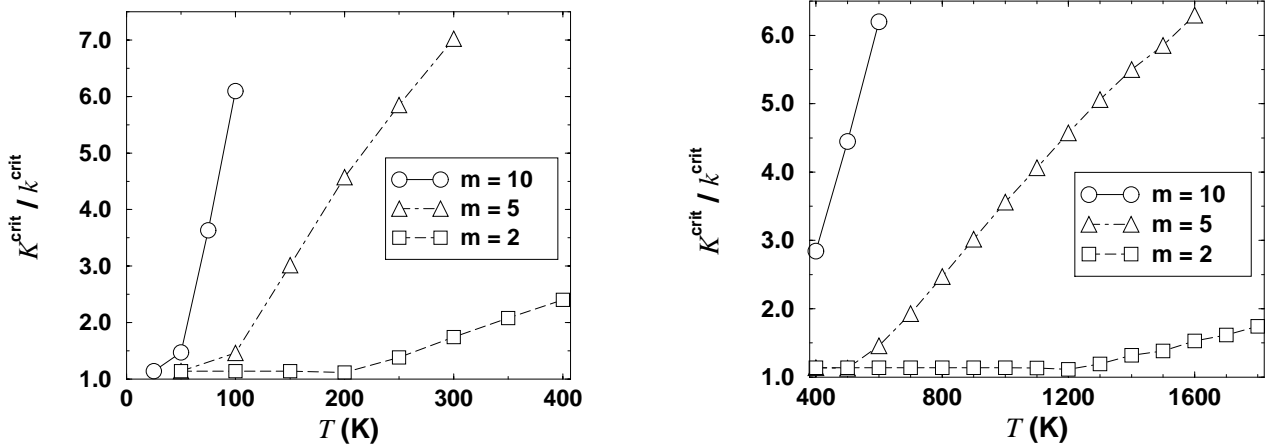


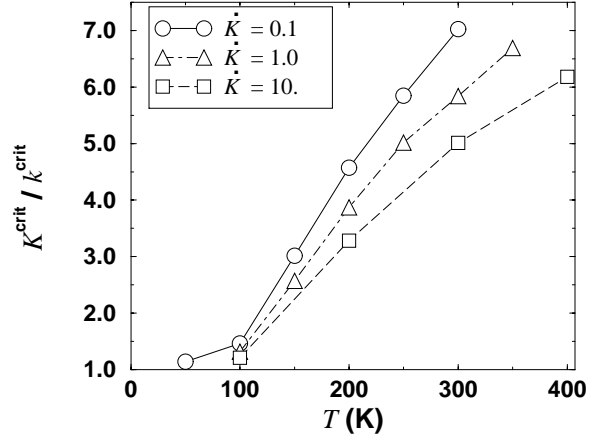
Figure 4.2: Relative fracture toughness versus temperature assuming edge-type mobility [Equation (2.10)] with an activation energy of $Q_{\text{dis}} = 0.3$ eV (A) and $Q_{\text{dis}} = 1.8$ eV (B). Results are shown for different stress exponents ($\dot{K} = 0.1$ MPa $\sqrt{\text{m}}/\text{s}$).

The stress exponent, in contrast, has a strong influence on the shape of the $K^{\text{crit}}-T$ -curves. A small stress exponent of $m = 2$ gives rise to a relatively shallow increase in fracture toughness with temperature. Moreover, the rise of the fracture toughness begins at higher temperatures compared to the results determined with higher stress exponents. The $K^{\text{crit}}-T$ -curve for $m = 10$ is the steepest of the three curves displayed, and starts to rise at the lowest temperature.

Quantitatively, the numerical results show a relative fracture toughness $K^{\text{crit}}/k^{\text{crit}}$ that is always greater than one. This is explained by the simple nucleation criterion, which causes at least a single dislocation to be nucleated. If the velocity of this dislocation is small, it stays close to the crack tip and further dislocation nucleation is suppressed. With rising temperature the velocity of the first emitted dislocation increases, and the separation between crack tip and dislocation increases significantly. Since the shielding of a more remote dislocation is weaker, the fracture toughness decreases slightly. This is seen in the $K^{\text{crit}}-T$ -curves for $m = 2$. At still higher temperatures, dislocation velocity becomes high enough to permit the nucleation of further dislocations to occur. Beyond this temperature the fracture toughness increases steadily. The temperature, where the fracture toughness starts to rise, strongly depends on the stress exponent.

The influence of the loading rate on the fracture toughness is shown in Figure 4.3 for $Q_{\text{dis}} = 0.3$ eV and $m = 5$. The dependence on the loading rate is not as strong as the

Figure 4.3: Fracture toughness as function of temperature for different loading rates. The activation energy for dislocation motion is $Q_{\text{dis}} = 0.3$ eV, the stress exponent is $m = 5$.



dependence on the stress exponent. The $K^{\text{crit}}-T$ -curves are more shallow for higher loading rates, such that the fracture toughness is reduced at all temperatures.

Figure 4.4 shows the fracture toughness as a function of temperature and loading rate for a temperature dependent stress exponent. For these calculations the dislocation mobility law formulated in Equation (2.10) has been used with the parameters mimicking edge dislocation mobility in tungsten (Table 2.3). The rise in the $K^{\text{crit}}-T$ -curve for the loading rate $\dot{K} = 0.1$ MPa $\sqrt{\text{m}}/\text{s}$ is moderate compared with the rise in the curves for constant stress exponents $m \leq 5$ in Figure 4.2. This is associated with the decrease in the stress exponent with rising temperature [Equation (2.11)]. An increase in loading rate causes the fracture toughness K^{crit} to decrease at all temperatures, as expected for a thermally activated process. This decrease is stronger for higher temperatures, but still significant at $T = 50$ K. Since the loading rate is constant, the time-to-fracture is

$$t_{\text{frac}} = \frac{K^{\text{crit}}}{\dot{K}}. \quad (4.1)$$

In no case a ductile behavior of the material is predicted by the 2D calculations, *i.e.* the critical local stress intensity at the crack tip was always exceeded after a finite time. Therefore no BDT temperature can be defined. However, as a general rule it can be stated that a high number of dislocations yields a good shielding of the crack tip and consequently a high fracture toughness. This is due to the long range stress field of the dislocations decaying only as $1/r$ with the distance from the dislocation. Therefore, even dislocations that are in some distance to the crack tip contribute to its shielding.

The number of emitted dislocations, shown in Figure 4.5, reflects the behavior of the fracture toughness, however, the differences between the different loading rates are more pronounced. At low temperatures, the total number of emitted dislocations N^{dis} always amounts to a few hundreds. This number increases with temperature. At higher loading rates the time until the critical load is exceeded is shorter than for smaller loading rates. Therefore

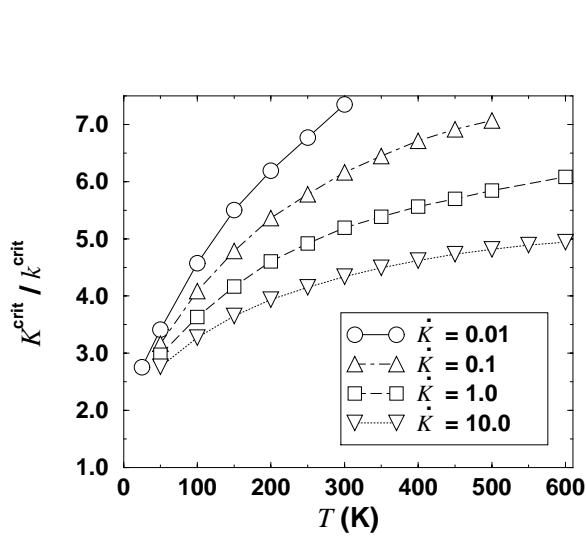


Figure 4.4: Relative fracture toughness $K^{\text{crit}}/k^{\text{crit}}$ as a function of temperature T for different loading rates \dot{K} ($\text{MPa}\sqrt{\text{m}}/\text{s}$). The numerical results are obtained for a dislocation mobility law mimicking non-screw dislocation motion with a temperature dependent stress exponent.

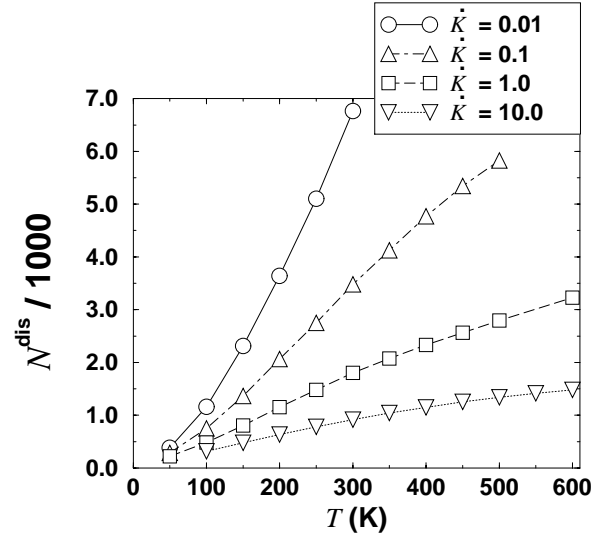
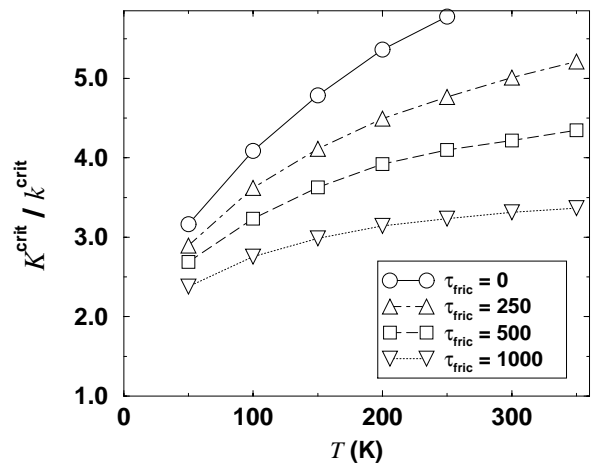


Figure 4.5: Number N^{dis} of emitted dislocations as function of temperature T . Rest of the assignments as in Figure 4.4

the dislocations cannot move away from the crack tip to a large distance. This causes a strong elastic interaction between the dislocations and the crack tip, which suppresses the nucleation of further dislocations.

4.1.3 Lattice friction

Figure 4.6: Relative fracture toughness $K^{\text{crit}}/k^{\text{crit}}$ as a function of temperature T for different lattice friction stresses τ_{fric} (in MPa) as given in the legend. The result without lattice friction is given for comparison. The loading rate for all data is $\dot{K} = 0.1 \text{ MPa}\sqrt{\text{m}}/\text{s}$.



A constant lattice friction stress reduces the dislocation velocity at all temperatures, because it reduces the effective driving force on the dislocations [see Equation (2.14)]. It is

seen in Figure 4.6 that a constant lattice friction stress reduces the fracture toughness at all temperatures. This holds for all loading rates. Moreover, the rise of the $K^{\text{crit}}-T$ -curves becomes more shallow with increasing lattice friction.

4.1.4 Screw dislocation mobility

The impact of applying a high activation energy in the non-screw dislocation mobility law [Equation (2.10)] has already been demonstrated. However, the motion of screw dislocations is better described by Equation (2.5), where the thermally aided overcoming of the Peierls barrier is taken into account. The material parameters for tungsten are provided in Table 2.1. Figure 4.7 shows the fracture toughnesses resulting from these calculations. The fracture toughness stays moderate up to $T = 200$ K, where it begins to rise with a small but increasing rate. The loading rate dependence at $T = 450$ K is comparable to that obtained for non-screw dislocations in tungsten at $T = 50$ K (*cf.* Figure 4.4).

The curvature of the $K^{\text{crit}}-T$ -graphs in Figure 4.7 is progressive, *i.e.* their slope is increasing. This is in contrast to the findings obtained for non-screw dislocation mobility, where – for stress exponents $m < 10$ – always a regressive curvature is determined.

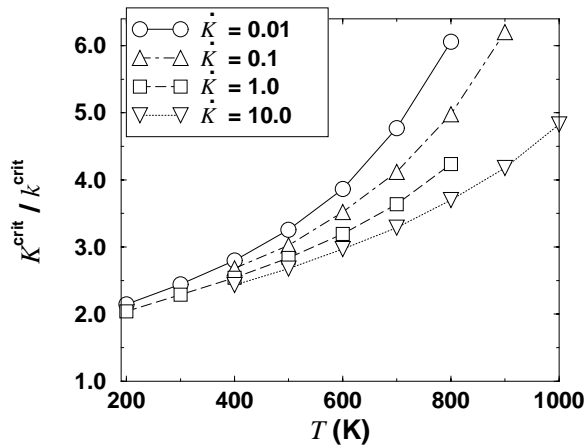


Figure 4.7: Relative fracture toughness as a function of temperature assuming screw dislocation mobility [Equation (2.5)]. The loading rate \dot{K} is given in $\text{MPa}\sqrt{\text{m}}/\text{s}$

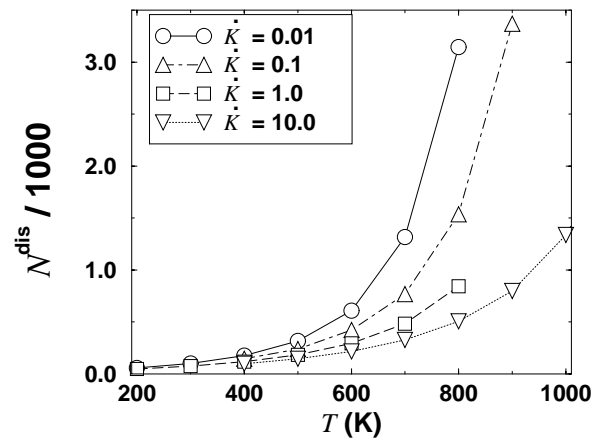


Figure 4.8: Number N^{dis} of emitted dislocations as a function of temperature T . Rest of the assignments as in Figure 4.7.

The total number N^{dis} of emitted dislocations plotted in Figure 4.8 is much smaller and much less rate dependent than that determined for non-screw dislocations. The temperature dependence is moderate up to $T = 600$ K. Beyond this temperature the number of dislocations increases strongly and exhibits a significant loading rate dependence.

4.2 Influence of dislocation nucleation

After the influence of dislocation mobility on the fracture toughness has been studied with the 2D model under the assumption of easy dislocation nucleation in the preceding section, dislocation nucleation at discrete sites is explicitly taken into account now. The separation λ of the nucleation sites is proposed to be temperature dependent on the basis of experimental observations in tungsten. From Figure 2.3 the source separation is estimated to be $\lambda_1 = 60 \mu\text{m}$ at $T_1 = 77 \text{K}$ and $\lambda_2 = 3 \mu\text{m}$ at $T_2 = 300 \text{K}$. The linear form

$$\lambda(T) = \lambda_1 - (\lambda_2 - \lambda_1) \frac{T - T_1}{T_2 - T_1} \quad (4.2)$$

is used to interpolate and extrapolate the parameter λ for the temperatures under consideration. A more reliable description of the source density along the crack front is not available at present.

In a first step 3D-DDD simulations are performed to obtain a qualitative estimate of the loading rate dependence of the additional distance δ , which dislocations must move before their shielding covers the entire crack front. Quantitative dependences cannot be derived, due to the limitations of the employed 3D model.

Subsequently the 2D model is employed to obtain an estimate of the influence of the model parameters δ on the macroscopic fracture toughness.

4.2.1 3D model

In the 3D simulations, a portion of the crack tip is regarded on which two sources with separation λ are active. Dislocation half loops are nucleated on a single blunting slip plane, such that the dislocations meet between the sources and coalesce. The extensions of the simulation box are chosen such that the dislocation half loops touch the boundary at the time they start to coalesce. The displacement δ of the dislocation segment parallel to the crack tip is investigated for different loading rates and source separations.

The time step Δt of the 3D simulations is determined by the fastest dislocations, which are found in the high stress field close to the crack tip ($\Delta t \sim 10^{-13} \text{s}$). This time step is much smaller than that of the 2D simulations ($\Delta t \sim 10^{-6} \text{s}$). This makes it necessary to apply much higher loading rates to obtain results within a reasonable calculation time. Higher loading rates, as shown above, shift the temperature regime of interest towards higher temperatures. However, in this temperature regime the dislocation mobility laws are unreliable, which is another drawback for the 3D simulation.

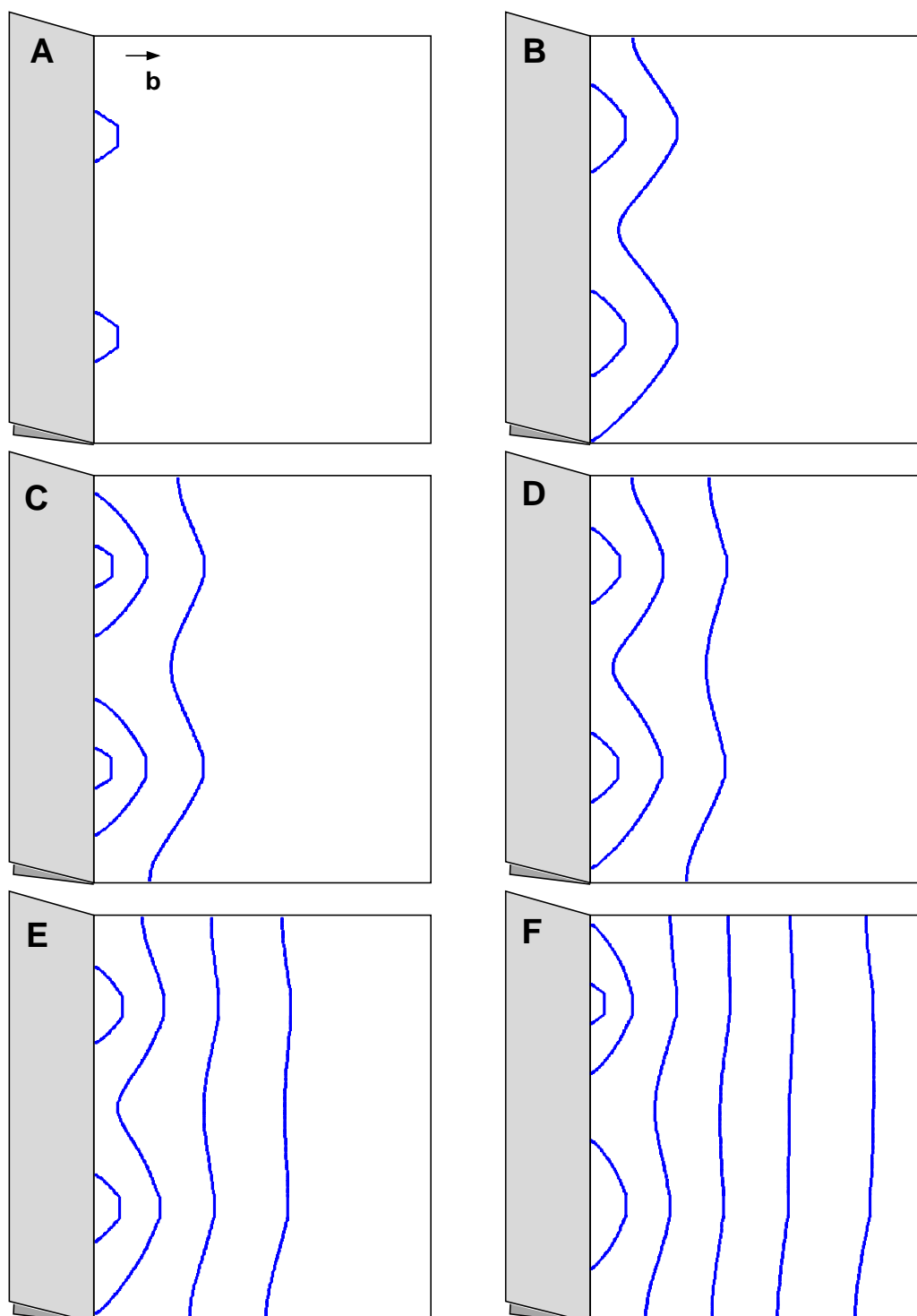


Figure 4.9: Different stages during the expansion of two half loops on the same slip plane. The temperature $T = 400$ K and the loading rate $\dot{K} = 5 \times 10^6$ MPa $\sqrt{\text{m}}/\text{s}$ were applied in this simulation. The Burgers vector b indicated in part A is representative for all other plots. The applied loads are $K^{\text{app}} = 0.602$ MPa $\sqrt{\text{m}}$ (A), 0.616 MPa $\sqrt{\text{m}}$ (B), 0.622 MPa $\sqrt{\text{m}}$ (C), 0.628 MPa $\sqrt{\text{m}}$ (D), 0.642 MPa $\sqrt{\text{m}}$ (E), and 0.662 MPa $\sqrt{\text{m}}$ (F). The slight asymmetry in the dislocation shapes results from an asymmetry in the dislocation positions with respect to the simulation box.

This problem is solved by considering that the time step is determined by the dislocations close to the crack tip. Under these high stresses the dislocations move athermally, *i.e.* their velocity is independent of temperature. If thus the activation energy for dislocation motion is lowered, the velocity of the fastest dislocation remains unchanged, whereas the average dislocation velocity is increased considerably. It has been demonstrated above that lowering the activation energy for dislocation motion shifts the temperature regime of interest towards smaller values, and thus has the opposite effect of increasing the loading rate. The relation between loading rate and temperature is further discussed in Section 5.2.3. Here it is sufficient to note that the average dislocation velocity can be increased by decreasing the activation energy for dislocation motion, without further speeding up the fastest dislocations. Therefore the time step of the simulation can remain constant.

In the following the activation energy for screw dislocation motion is assumed to be $H_{\text{screw}} = 1.27 \text{ eV}$. The activation energy for the motion of non-screw dislocations is already low. If this activation energy is further reduced, the motion of non-screw dislocation is no longer thermally activated at temperatures above $T = 300 \text{ K}$, *i.e.* a temperature change in this regime does not affect dislocation mobility. Therefore dislocation motion is assumed to obey the viscous drag law formulated in Equation (2.2). The drag coefficient $B = 8 \times 10^{-4} \text{ Pa s}$ is chosen to be half the value obtained for copper (Jassby and Vreeland, Jr., 1970). The rest of the parameters is set according to Tables 2.1 and 2.3.

Figure 4.9A–F shows the slip plane during different stages of a simulation at temperature $T = 400 \text{ K}$ and $\dot{K} = 5 \times 10^6 \text{ MPa}\sqrt{\text{m}}/\text{s}$. The slip plane is inclined by 45° with respect to the crack plane. The simulation was started with an applied load of $K^{\text{app}} = 0.6 \text{ MPa}\sqrt{\text{m}}$, such that two dislocation half-loops are emitted right from the start (Figure 4.9A). The half loops expand and a second pair of half loops is nucleated. Eventually the first dislocation pair coalesces and forms a single dislocation line that is still strongly curved (Figure 4.9B). Under the influence of line tension the dislocation shape becomes smoother (C). This process is repeated for the second (D), third (E), and fourth (F) pair of emitted half loops. Finally the emitted dislocations start to form an inverse pile-up in front of the crack tip. The most distant dislocations have developed into almost completely straight lines parallel to the crack tip, as proposed in the model of dislocation emission at discrete sources for the 2D simulation (Section 3.2.3).

When two half loops are merged, the newly generated segment can be described as a single straight dislocation segment. This increases the efficiency of the calculation by far and does not affect the results noticeably. The position of this new segment is where the frontmost segment of the two “mother”-segments has been. This position can be identified with the model parameter δ of the 2D simulation. Figure 4.10 shows this parameter as a function of the applied load. After some nucleation events, δ is almost constant, and only slowly rising

as the load increases. The lower bound for δ is given by the extension of the dislocation nuclei that are used for the nucleation criterion. A new nucleus can only be developed if the dislocation that has been generated before is sufficiently remote.

An increase in the source separation increases the the parameter δ as seen in Figure 4.10. An increase of the loading rate has also been found to increase δ . However the range of loading rates available for the 3D simulation is so small that this result is hardly significant. Moreover δ depends strongly on the radius of the half loops of the dislocation nuclei. This radius is more or less chosen arbitrarily such that the first emission occurs at 20% of the local stress intensity for failure.

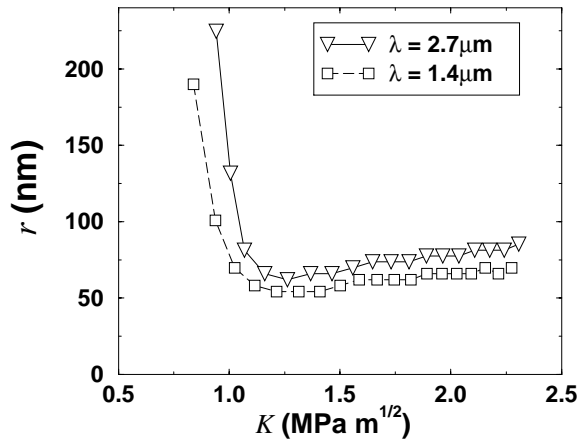


Figure 4.10: The model parameter δ as calculated from the 3D-DDD simulation for different source separations λ as a function of the applied load. The simulations have been performed at room temperature and a loading rate $\dot{K} = 10^8 \text{ MPa}\sqrt{\text{m}}/\text{s}$.

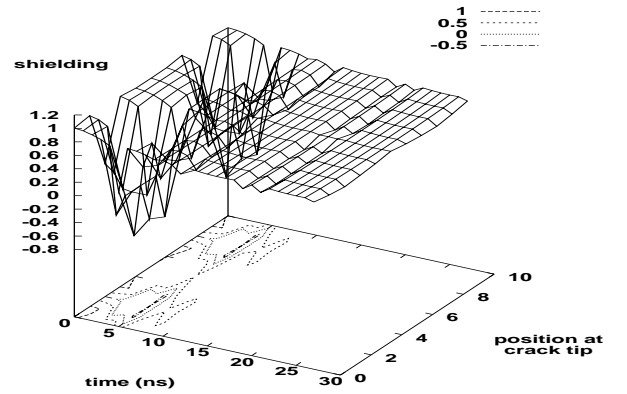


Figure 4.11: The shielding $k^{\text{tip}}/K^{\text{app}}$ along the crack front at room temperature as a function of time. The separation of the nucleation sites is $\lambda = 1.4 \mu\text{m}$, the total width of the simulation box is 2λ . The loading rate amounts to $\dot{K} = 4 \times 10^7 \text{ MPa}\sqrt{\text{m}}/\text{s}$.

In Figure 4.11 the shielding $k^{\text{tip}}/K^{\text{app}}$ of the crack front by the dislocation population is plotted as a function of time. At the beginning the shielding is very localized around the nucleation sites. Outside the region covered by the half loops a small anti-shielding is found. After some time the shielding is more homogeneously distributed along the crack front, but still quite strong (even negative values are calculated, which indicates that there are crack closing stresses). At still larger times the shielding along the crack front is constant, because the dislocation population consists mainly of straight segments. From this point the shielding decreases steadily, since the increasing load pushes the dislocations farther away from the crack tip. This corresponds to the slight increase in the δ parameter with the load.

4.2.2 2D model

In this section the dependence of the fracture toughness on the model parameter δ is investigated for different loading rates and temperatures. The parameter δ , *i.e.* the additional distance that dislocations have to move before their shielding covers the entire crack front, is a function of the source separation λ and the loading rate \dot{K} , as seen in the previous section. It can also be presumed that δ depends on the temperature. However, neither of these dependencies can be formulated in a strict way. For simplicity, δ is considered as being a tenth of the source separation λ . The consequences of this simplification are discussed later.

Pure edge dislocations are considered whose mobility is described by Equation (2.10) and Table 2.3. Figure 4.12 shows the fracture toughness as function of temperature for different loading rates. The fracture toughness at low temperatures is smaller than the one predicted for easy dislocation nucleation (Figure 4.4). Beyond the temperature at which the nucleation sites are dense along the crack front, the results for both models are equal. Between these two regimes a rather steep increase in fracture toughness is observed.

Higher loading rates cause again lower fracture toughnesses at all temperatures. However, the loading rate dependence of fracture toughness at low temperatures is comparatively small, and virtually vanishes at the lowest temperatures investigated. The number of emitted dislocations N^{dis} strongly depends on loading rate and temperature (Figure 4.13). However, below $T = 100$ K this dependence almost vanishes.

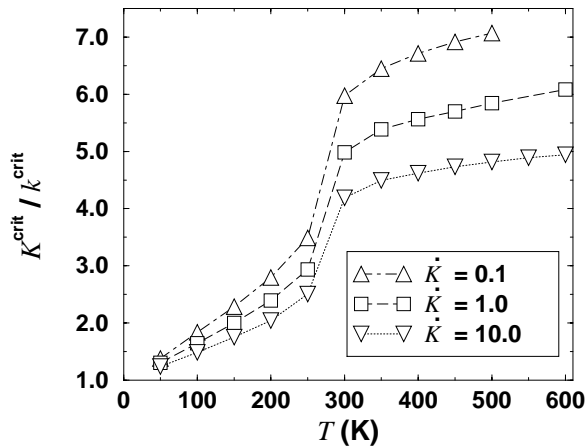


Figure 4.12: Fracture toughness K^{crit} as a function of temperature T for the same loading rates \dot{K} ($\text{MPa}\sqrt{\text{m}}/\text{s}$) and material parameters as in Figure 4.4, but under the assumption of discrete nucleation sites.

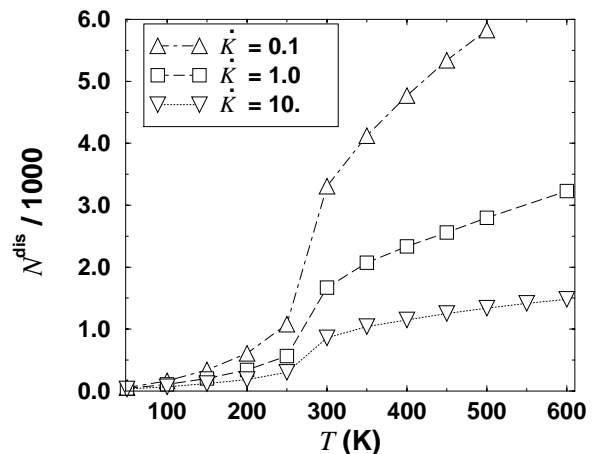


Figure 4.13: Number N of dislocations emitted at different loading rates \dot{K} ($\text{MPa}\sqrt{\text{m}}/\text{s}$) as function of temperature T . Dislocation nucleation at discrete sites is considered.

4.3 Crack-tip blunting

In the previous sections the only effect of the dislocations on the crack tip was their elastic interaction. However, the net Burgers vector of the dislocation population requires that the crack tip is also blunted. It is obvious, that the advance of a blunted crack tip is only possible if diffusion is involved. To achieve crack advance, a sharp crack has to be re-nucleated. To account for this additional hindrance to crack advance the critical local stress intensity is assumed to be proportional to the square root of the crack tip radius [see Equation (3.9)]. A proportionality constant of $C = 4 \times 10^{-3}$ yields fracture toughnesses comparable with experiment (Riedle, 1995, *cf.* Figure 5.3 and). This means that for a number of 5000 emitted dislocations, *i.e.* a tip radius of $r_{\text{tip}} = 5000 b \sin 70.5 = 1.3 \mu\text{m}$, the critical local stress intensity is raised by 14%. For a notch radius of $r_{\text{tip}} = 60 \mu\text{m}$ the critical local stress intensity is almost doubled. A higher value for the parameter C results in a severe overestimate for the fracture toughness as compared with experiment.

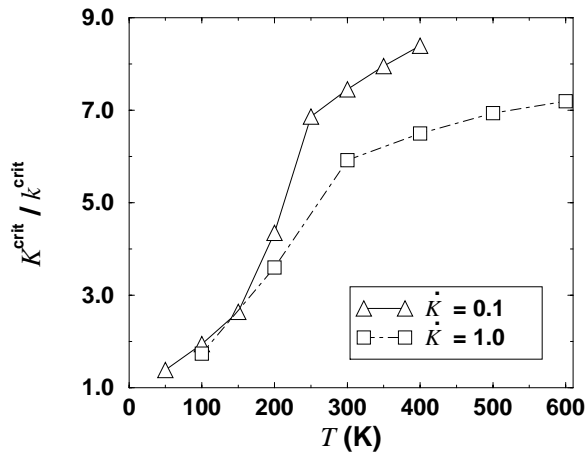


Figure 4.14: Relative fracture toughness at different loading rates as function of temperature. The blunting of the crack tip is taken into account according to Equation (3.9) with constant $C = 4 \times 10^{-3}$.

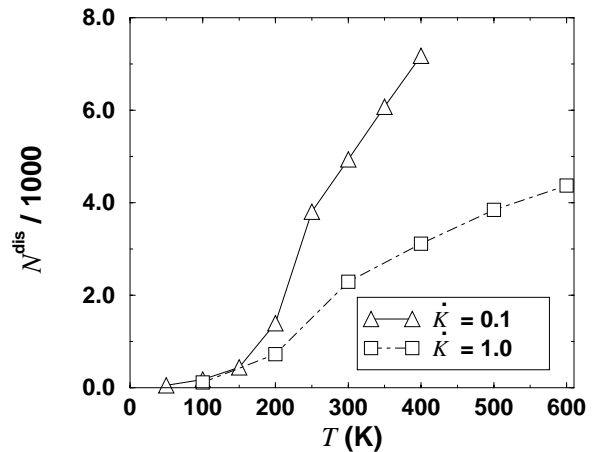


Figure 4.15: Number of emitted dislocations as function of temperature under the same conditions as Figure 4.14.

The influence of the crack tip blunting on fracture toughness and the total number of emitted dislocations is small at low temperatures (see Figures 4.14 and 4.15). At higher temperatures, already below the temperature where the density of nucleation sites along the crack front becomes dense, were the dislocation nucleation sites become dense the blunting strongly increases the fracture toughness. The blunting results in a self-amplifying effect as seen in Figure 4.16. The more dislocations are emitted, the more the crack tip is blunted. This increases the critical local stress intensity for fracture and therefore yields more time for

further dislocation emission. Accordingly, the fracture toughness (see Figure 4.16 and also Figure 4.4) and the number of emitted dislocation are found to be larger than for (quasi-) homogeneous emission (*cf.* Figures 4.5, 4.13 and 4.15).

Figure 4.17 shows how the critical local stress intensity and the local stress intensity at the crack tip develops with the applied load K^{app} . The increase in local stress intensity k^{tip} is still much steeper than the increase in the critical local stress intensity k^{crit} due to the blunting. A BDT would occur if the $K^{\text{app}}-k^{\text{tip}}$ -curve remained below the $K^{\text{app}}-k^{\text{crit}}$ -curve at all applied loads. However no indications of such a BDT was found, even at lower loading rates.

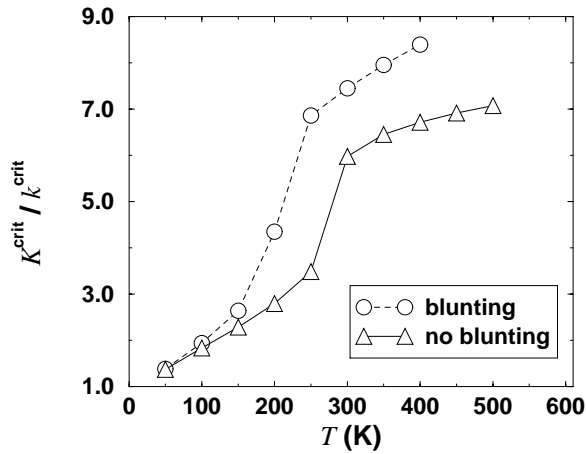


Figure 4.16: Comparison of the relative fracture toughness with and without crack-tip blunting for the loading rate $\dot{K} = 0.1 \text{ MPa}\sqrt{\text{m}}/\text{s}$.

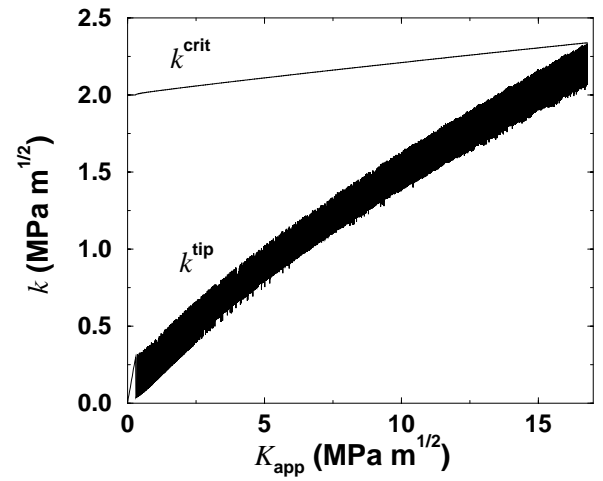


Figure 4.17: Local stress intensity at the crack tip k^{tip} versus applied stress intensity K^{app} ($T = 400 \text{ K}$, $\dot{K} = 0.1 \text{ MPa}\sqrt{\text{m}}/\text{s}$). The critical local stress intensity k^{crit} is a function of the crack tip radius as described by Equation (3.9) with $C = 4 \times 10^{-3}$.

Discrete dislocation models are not well suited to describe large plastic strains, because of the large number of dislocation necessary for such a description. Furthermore, dislocation multiplication is not taken into account by the model applied in this work. To overcome these difficulties, a continuum plasticity model, which has been used to describe the BDT in silicon (Nitzsche and Hsia, 1994), is adapted to tungsten in the following section.

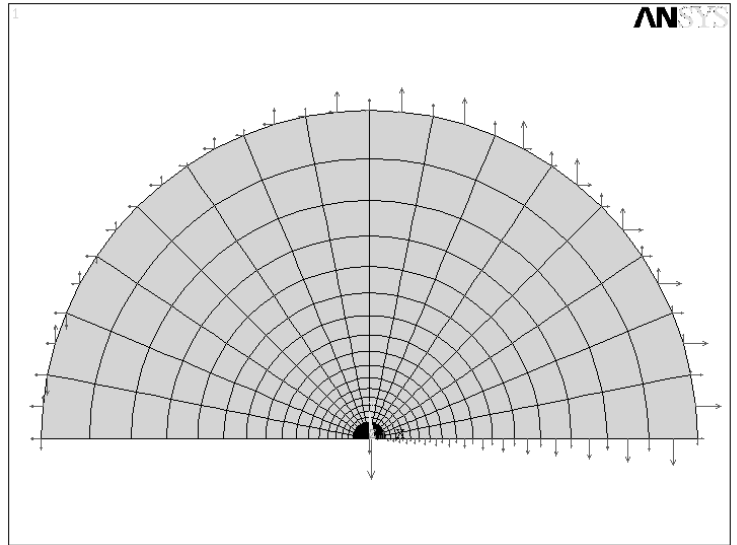
4.4 Continuum model of the brittle-to-ductile transition

A 2D finite element model of the crack-tip region is set up, which is based on a viscoplastic material behavior. Compared with the 2D-DDD method the finite element description

is not limited to single slip planes and small plastic strains. The constitutive law of the continuum plasticity description captures activity on multiple slip planes and cross-slip as well as dislocation multiplication in an average sense. The model employed here has been developed by Nitzsche and Hsia (1994) to describe the sharp BDT of silicon single crystals (*cf.* Section 2.4.1).

The geometry of the finite element model employed here is a half-circle of radius R (see Figure 4.18). Following Nitzsche and Hsia (1994), the linear elastic displacements of a pure K_I field are applied as nodal displacements at the outer boundary of the model. Free boundary conditions are active on one half of the diameter which represents the symmetry boundary. Accordingly, this part is the crack plane. Along the second half of this diameter perpendicular nodal displacements are blocked, which yields a mirror symmetry along this line. Plane strain conditions are assumed for all elements. The size r_{elast} of the elastic zone surrounding the crack tip is smaller than the crack length R by a factor of 20.

Figure 4.18: 2D finite element model to describe crack-tip plasticity and the BDT. The viscoplastic zone is shaded light gray, the elastic zone dark gray. Plane strain is assumed for all elements. The forces resulting from the displacement boundary conditions are displayed as arrows. Details of the model are given in the text.



The material behavior outside the elastic zone is rate-dependent viscoplastic. The strain rate $\dot{\epsilon}$ follows the Orowan law expressed in Equation (2.1), in which the dislocation velocity according to Equation (2.10) is inserted. This gives for the the strain rate

$$\begin{aligned}\dot{\epsilon} &= b\rho_m A \exp\left(-\frac{Q_{\text{dis}}}{k_B T}\right) \left(\frac{\tau}{\tau_N}\right)^{m(T)} \\ &= A^*(T) \left(\frac{\tau}{\tau_N}\right)^{m(T)},\end{aligned}\quad (4.3)$$

with a temperature dependent stress exponent $m(T) = \alpha/T + \beta$. The form of this viscoplastic law resembles the usual formulations of power law creep. It is adapted to the case of tungsten from Equation (2.13). The material parameters are given in Tables 2.3 and 2.4, except for

the the density ρ_m of mobile dislocations. A value of $\rho_m = 3.5 \times 10^{10} \text{ m/m}^3$ is assumed for the mobile dislocation density, because this value gives good agreement of the numerical results for the BDT temperatures with the experimental data of Riedle's work. If the dislocation density is higher, the BDT occurs at lower temperatures and *vice versa*. The value of ρ_m employed here is slightly higher than that determined by X-ray topography of Riedle's specimen material ($\rho_{\text{exp}} = 5.0 \times 10^9 \text{ m/m}^3$) (Glebovsky, Shipilevsky, Kapchenko and Kireyko, 1992; Glebovsky, Kapchenko and Shipilevsky, 1992).

Similar to the 2D-DDD model, the numerical simulations start with a zero applied stress intensity K_I , which is raised with a constant rate \dot{K} . The temperature is assumed constant during each simulation. The applied load is increased in equidistant steps ΔK . The system is allowed to relax for the time $\Delta t = \Delta K / \dot{K}$ after each step. The convergence of the finite element calculation is verified by controlling the relaxation of the nodal forces.

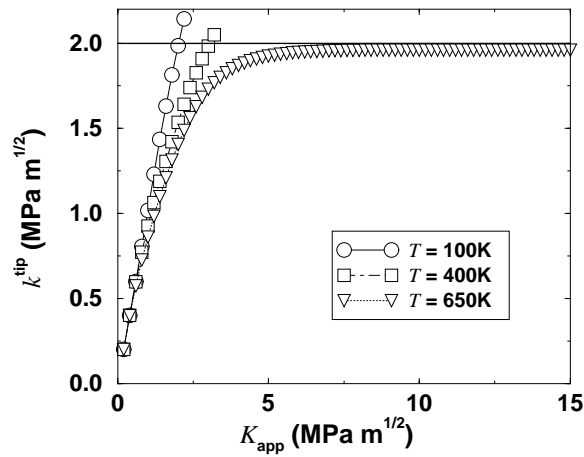


Figure 4.19: Local stress intensity k^{tip} versus applied stress intensity K^{app} for different temperatures T . The loading rate is $\dot{K} = 1.0 \text{ MPa}\sqrt{\text{m}}/\text{s}$. The critical local stress intensity is $k^{\text{crit}} = 2.0 \text{ MPa}\sqrt{\text{m}}$ (thick lines).

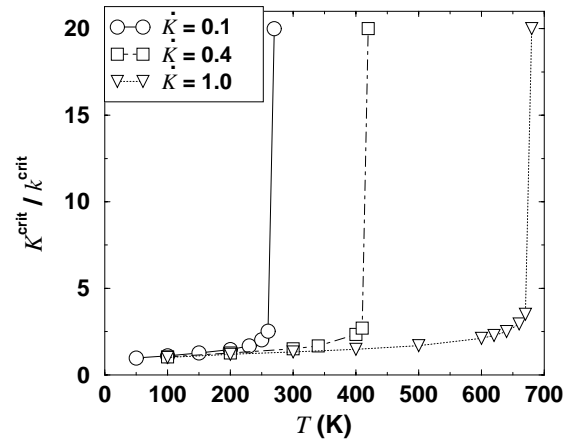


Figure 4.20: Fracture toughness K^{crit} versus temperature T as calculated with the 2D finite element model. The density of mobile dislocations is $\rho_m = 3.5 \times 10^{10} \text{ m/m}^3$, the loading rate \dot{K} is given in $\text{MPa}\sqrt{\text{m}}/\text{s}$.

The simulation is stopped when the critical local stress intensity at the crack tip is exceeded or when the applied load of $K^{\text{app}} = 40 \text{ MPa}\sqrt{\text{m}}$ is reached. In the latter case, the local stress intensity assumes a constant value lower than the critical stress intensity, as seen in Figure 4.19. The first occurrence of such a flat $k^{\text{tip}}-K^{\text{app}}$ -curve defines the BDT.

Fracture toughness versus temperature is plotted for several loading rates in Figure 4.20. The fracture toughness remains almost constant up to the BDT temperature, where it rises sharply. As stated above, for the chosen dislocation density the BDT temperatures agree approximately with the experimental results revisited in Section 2.3.3. Furthermore, the results are consistent with the observations of Nitzsche and Hsia (1994). An evaluation of

the BDT temperatures with Equation 2.12 yields an apparent activation energy of the BDT of $U_{\text{BDT}} = 0.09$ eV, which is significantly lower than the activation energy of the underlying viscoplastic deformation law ($Q_{\text{dis}} = 0.3$ eV).

The plastic strain at the boundary at radius R remains below 1% up to applied loads of $K_I = 20$ MPa $\sqrt{\text{m}}$, which provides a justification for applying the elastic displacements as boundary conditions.

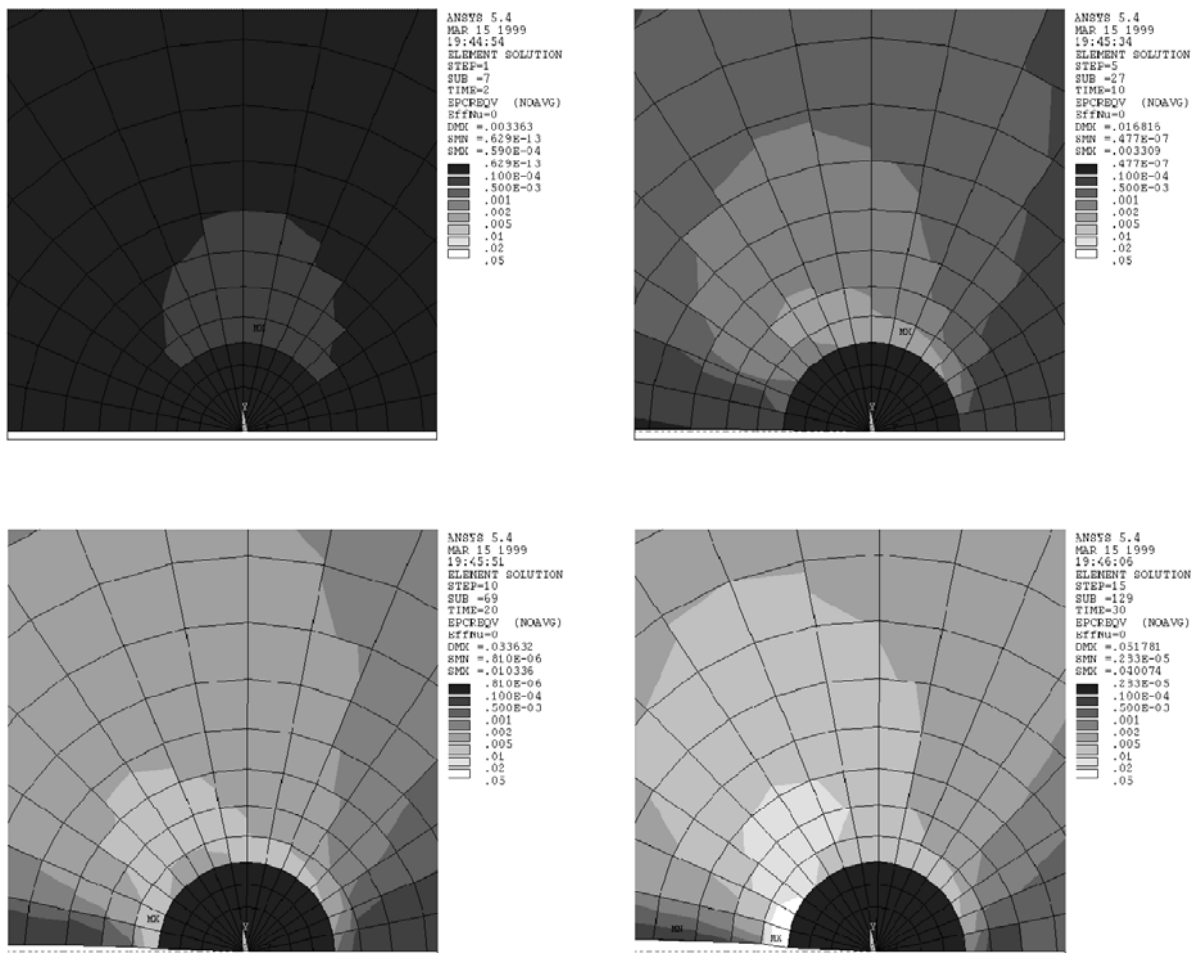


Figure 4.21: The von Mises equivalent plastic strain at different applied loads. The color scales are the same for each plot. The plastic zone expands from the highly-stressed regions towards the crack plane. Minima (MN) and maxima (MX) of the plastic strain are indicated in each graph.

A detailed analysis of the spatial distribution of the plastic strain at different stages of the loading reveals that the plastic zone starts to develop close to the elastic zone around the crack tip in the region between 45° to 135° , where the highest stresses are found (Figure 4.21A). During plastic relaxation these high stress levels are diminished and the plastic zone expands continuously around the elastic zone (Figures 4.21B). Finally, the location of the highest plastic strain moves towards the intersection of the elastic zone with the crack plane (Figure 4.21C and D).

During the simulations where the critical stress intensity at the crack tip is exceeded, the expansion of the plastic zone towards the crack plane is not complete. In these cases the load is transmitted to the elastic zone by the material in the vicinity of the crack plane, which behaves almost elastically. Only when this load transmission is delayed or even interrupted by viscoplastic relaxation, the elastic zone, and thus the crack tip, are efficiently shielded from the applied load. Since the time needed for the viscoplastic zone to expand towards the crack plane depends on temperature, the whole process is thermally activated as described by Equation (4.3).

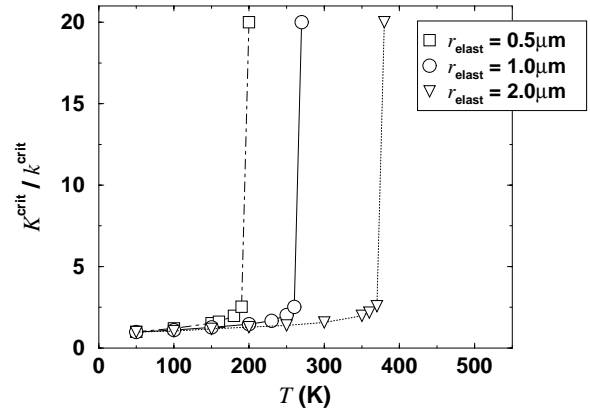


Figure 4.22: Dependence of the results on the model parameter r_{elast} . The loading rate is $\dot{K} = 0.1 \text{ MPa}\sqrt{\text{m}}/\text{s}$.

The size of the elastic zone has a quite pronounced influence on the resulting fracture toughness and BDT temperature. As seen in Figure 4.22, a smaller elastic zone results in higher fracture toughnesses and lower BDT temperatures. In contrast, a larger elastic zone decreases the fracture toughness and increases the BDT temperature. This is expected because the stresses are higher closer to the crack tip, and therefore the plastic relaxation at the perimeter of a smaller elastic zone is faster. In the investigated parameter range for r_{elast} no convergence of the results towards a constant value could be observed. Values smaller than $r_{\text{elast}} = 0.2 \mu\text{m}$ produce numerical problems.

The influence of the radius of the elastic zone on fracture toughness and BDT temperature is inverse to the influence of the dislocation density. A higher dislocation density leads to a faster plastic relaxation. This can be compensated by increasing the size of the elastic zone, which translates the zone of plastic relaxation into regions where the stresses are lower.

Chapter 5

Discussion

In this chapter the numerical results are discussed with respect to their importance to crack-tip plasticity and the brittle-to-ductile transition. Although the results have been obtained with a specific model under specific assumptions it will be shown that it is possible to generalize certain findings.

The discussion is subdivided with respect to the temperature regimes. The different sections deal with the low-temperature regime, the semi-brittle regime, and the BDT itself. The numerical data from this work is compared with experimental results on tungsten single crystals (Riedle, 1995). Generalization to and comparison with different materials is made where adequate.

After the physical meaning of the results is discussed, the applied methods are critically reviewed. This chapter is concluded by raising new questions that appeared in the course of this work and by proposing approaches to tackle these questions.

5.1 Low-temperature regime

In this section the importance of dislocation nucleation for the fracture toughness at low temperatures is deduced. This can be achieved because the process of dislocation nucleation can be influenced deliberately in experiment *and* in simulation.

5.1.1 Loading rate dependence

A thermally activated process is expected to show a rate dependent behavior. Since the thermally activated dislocation motion is the basis of the 2D-model, it must yield a thermal activation of fracture toughness. This is true especially for the simplest version of the model, where dislocation nucleation is assumed to occur without an energy barrier and homogeneously along the crack front. In Figure 4.4 it is consequently seen that the fracture

toughness obtained under these conditions shows a significant rate sensitivity even at the lowest temperature investigated ($T = 50$ K). Quantitative statements on the activation energy of the thermally activated fracture toughness are derived from the scaling behavior of the results, as detailed in Section 5.2.3.

In contrast, experiments conducted on tungsten single crystals with a sharp pre-crack did not reveal a loading rate dependence at liquid nitrogen temperature (Riedle, 1995). The data of Ebrahimi and Shrivastava (1998) on NiAl single crystals are not quite conclusive in this respect, but appear to display a weak rate sensitivity at room temperature. However, these authors used double-notched specimens without a sharp pre-crack. Dislocation-free silicon single crystals below the BDT temperature generally reveal fracture toughnesses close to the critical local stress intensity (St. John, 1975; Brede and Haasen, 1988; Samuels and Roberts, 1989). Moreover, the fracture toughness does not vary significantly with loading rate or temperature.

As described in Section 4.1.2 there exists a temperature regime in the numerical results, where only a single dislocation is nucleated and where consequently no rate sensitivity of the fracture toughness is found. This regime extends to higher temperatures for larger activation energies and smaller stress exponents. Silicon possesses a small stress exponent and a high activation energy for dislocation motion [$m = 1.1$ to 1.4 and $Q_{\text{dis}} = 1.4$ eV (Brede, 1993)]. Therefore the shallow increase in fracture toughness at temperatures below the BDT temperature is not quite unexpected (Brede and Haasen, 1988; Brede, 1993). However, the increase in fracture toughness determined experimentally is still much more shallow than that predicted by numerical simulations (Roberts, 1996). The fracture toughness of predeformed silicon specimens exhibits a temperature sensitivity already below the BDT temperature (Warren, 1989). However, the loading rate dependence has not been investigated in this case.

In the simulations for screw dislocations in tungsten, where the activation energy for dislocation motion ($H_{\text{screw}} = 1.8$ eV) is about six times larger than that for non-screw dislocations, the rate sensitivity practically vanishes below 200 K. Above this temperature the fracture toughness rises slowly and shows a significant rate sensitivity. The assumption of a purely screw dislocation controlled crack-tip plasticity leads to a severe underestimate of the fracture toughness at intermediate temperatures due to the high activation energy for screw dislocation motion. As detailed below this high activation energy for dislocation motion gives rise to an activation energy for the BDT which is also inconsistent with experiment.

Still it could be argued that crack-tip plasticity below $T = 150$ K is controlled by screw dislocations, while at higher temperatures it is controlled by other mechanisms. Another way of explanation of the low rate sensitivity at low temperatures would be to assume non-screw dislocation mobility and a small stress exponent. However, at these low temperatures

the employed value of the stress exponent is quite reliable, since it is directly measured at $T = 77\text{ K}$ (Schadler, 1964). This stress exponent is too high to explain the small rate dependence of the results.

None of the items mentioned so far can satisfactorily explain the rate insensitivity of the fracture toughness at low temperatures. Consequently, the assumption of easy and homogeneous dislocation nucleation must be rejected, and the implication of assuming dislocation nucleation at discrete sites are discussed in the following.

At least for dislocation free material with a sharp pre-crack, dislocation nucleation is presumed to be the limiting factor for fracture toughness at low temperatures. In this case, the lack of mobile dislocations would be responsible for the experimentally found low, rate and temperature-insensitive fracture toughness in the low temperature regime. This argument is supported by etch pit experiments on *post mortem* fracture surfaces of tungsten, which revealed that dislocation activity at low temperatures is concentrated at discrete sites along the crack front (Figure 2.3A). The same finding has been reported for silicon single crystals (Roberts et al., 1994). These results are also consistent with the theoretical work of Rice and Thomson (1974), who found homogeneous dislocation nucleation to be energetically unfavorable in bcc materials and silicon. As discussed in Section 2.1 dislocation nucleation in these materials occurs primarily at imperfections in the crack front (Zhou and Thomson, 1991*a*; Xu et al., 1995).

The assumption that dislocation nucleation at discrete sites reduces the rate sensitivity of the fracture toughness is tested by numerical simulations with the 2D model. As shown in Section 3.2.3, the influence of dislocation nucleation at discrete sites can be introduced into the 2D-model via the model parameter δ . This parameter is understood as the additional distance a dislocation has to move away from its nucleation site until its shielding covers the relevant section of the crack front. As seen in Figure 4.12, the rate dependence of the fracture toughness virtually vanishes at $T = 50\text{ K}$ on the scale of the plot. A quantitative evaluation of the differences in fracture toughness at $T = 50\text{ K}$ yields $(K^{\text{crit}}_1 - K^{\text{crit}}_2)/K^{\text{crit}}_1 = 16\%$ for nucleation at discrete sites and $(K^{\text{crit}}_1 - K^{\text{crit}}_2)/K^{\text{crit}}_1 = 19\%$ for homogeneous nucleation, where K^{crit}_1 is the fracture toughness at the loading rate of $\dot{K} = 0.01\text{ MPa}\sqrt{\text{m}}/\text{s}$ and K^{crit}_2 at $\dot{K} = 10\text{ MPa}\sqrt{\text{m}}/\text{s}$. This shows that under the conditions of the numerical simulation the relative loading rate sensitivity of the fracture toughness is slightly lowered by dislocation nucleation at discrete sites as compared with the rate sensitivity for homogeneous nucleation. Two reasons are identified why the simulation assuming nucleation at discrete sites still gives an overestimate of the loading rate dependence of the fracture toughness at low temperatures:

(i) In the 2D-model, the parameter δ is chosen proportional to the source separation, as determined by etch pit experiments (Figures 2.3A and B). As noted upon the introduction

of this parameter (Section 3.2.3) and as seen in the 3D calculations (Section 4.2.1), this parameter itself is loading rate dependent. Due to the inherent problems of the 3D-simulation, the loading rate dependence could not be investigated over a significant range. A small increase of δ with the loading rate was found within the investigated range of loading rates. To further improve the quantitative results of the 2D model, the parameter δ should be treated as loading rate dependent.

(ii) The dynamic evolution of the inverse dislocation pile-up in front of the crack tip is not changed by the introduction of the model parameter δ . The model of dislocation nucleation at discrete sites, which is employed here, only captures the delay in the shielding of the entire crack tip. The elastic interaction between the dislocation is not altered within this model, but it is evident that the repulsion between several small dislocation half loops and the rest of the pile up is smaller than the repulsion between a long, straight dislocation and the pile up. This leads to an overestimate of the dislocation velocity at which the dislocations move away from the crack tip, which, as a consequence, facilitates the nucleation of new dislocations.

However, it is not clear *a priori* if the model parameter δ reduces the rate sensitivity of the fracture toughness. This is found in the 2D simulations and thus confirms the assumption that dislocation nucleation is the decisive parameter for crack-tip plasticity in the low temperature regime.

5.1.2 Predeformation

In the previous section it has been shown that for tungsten the assumption of homogeneous dislocation nucleation in the low temperature regime is inconsistent with the small loading rate sensitivity of the experimental results. Taking into account dislocation nucleation at discrete sites influences the numerical results to give smaller rate sensitivities. However, this smaller rate sensitivity might also be achieved by modifications in the dislocation mobility law. Therefore additional considerations are needed to confirm the important role of dislocation nucleation in the low temperature regime.

There is experimental evidence that dislocation nucleation at a crack tip can be facilitated by increasing the dislocation density in the vicinity of a crack tip: Michot's (1997) *in-situ* investigation of silicon single crystals with X-ray topography showed that dislocation nucleation at an almost perfect crack front is a rare event, that can even be completely suppressed until an externally generated dislocation intersects the crack tip. From the instant of intersection a plastic zone develops along the crack front.

In Riedle's (1995) experimental investigation of predeformed tungsten single crystals, specimen material was predeformed in compression by 10% plastic strain at a tempera-

ture $T = 400$ K. Such a warm prestraining increases the dislocation density in the material. A crack, which is initiated after the predeformation, is therefore surrounded by a dislocation cloud. Dislocation intersections with the crack tip consequently occur frequently. Possibly also the morphology of the crack front is more irregular, because the pre-crack is introduced into a work hardened material. However, the *post mortem* specimens have not been investigated in that respect. According to the model of dislocation nucleation proposed in Section 3.2.3, dislocation nucleation at a “rougher” crack front is easier than at a more ideal, straight crack front.

In any case, it can be safely assumed that dislocation generation at the crack front is considerably facilitated by predeformation, either by enhanced dislocation generation or by increasing the density of active nucleation sites. Consequently the fracture toughness at low temperatures should be increased. This is in fact found experimentally in tungsten (Gumbsch et al., 1998), and also in silicon (Warren, 1989) and NiAl (Ebrahimi and Shrivastava, 1998).

This increase in fracture toughness cannot be explained by the polarization of a pre-existing dislocation population in the crack-tip stress field. As visualized in Figure 5.1 the anti-shielding dislocations are attracted towards the crack tip, whereas the shielding dislocations are repelled from it. Consequently, such polarization even decreases the fracture toughness. An enhanced shielding of the crack tip by polarization is only achieved if the anti-shielding dislocations are absorbed by the crack surface. Similar observations are made with the 2D finite element model (Section 4.4), where it is found that shielding of the crack tip is only achieved when the plastic zone reaches the crack plane.

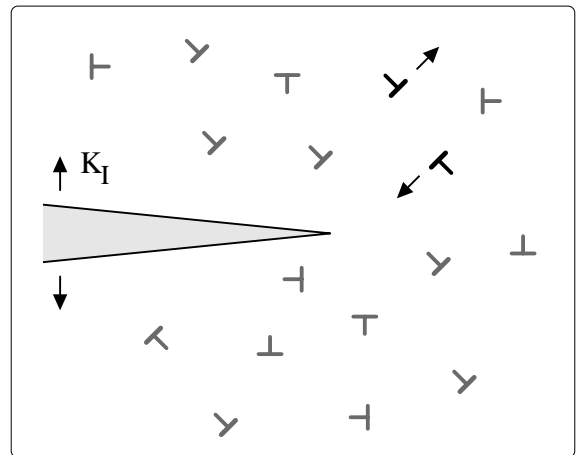


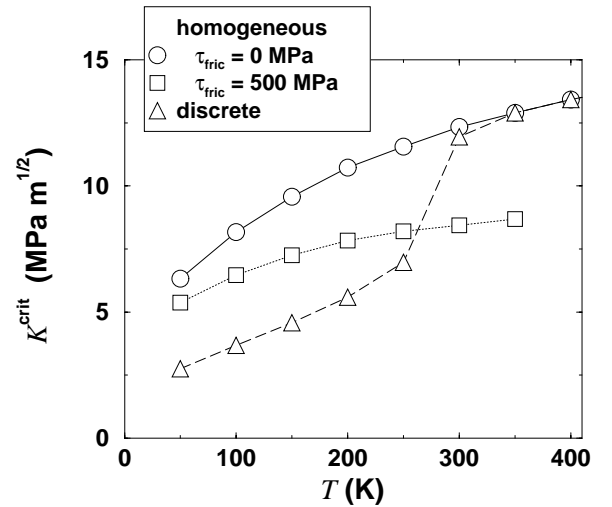
Figure 5.1: The polarization of preexisting dislocations around a crack tip increases the load on the crack tip, because anti-shielding dislocations are attracted towards the crack tip.

Zhou and Thomson (1991a) investigated the plastic polarization of the crack tip region quantitatively for the special case of dislocation dipoles originating from external dislocation sources, *i.e.* sources that are separated from the crack tip by more than a few Burgers vectors. Zhou and Thomson (1991a) found that dipoles originating from external sources are always anti-shielding. These two arguments show that neither the polarization of an existing

dislocation population, nor the nucleation of dislocation dipoles from external sources can shield the crack from the external load, unless anti-shielding dislocations are absorbed by the crack.

Since the dislocation cloud around the crack tip does not immediately produce shielding and the additional energy dissipation by dislocation motion is insignificant compared with crack-tip shielding at low temperatures, it must be concluded that the experimentally observed increase in fracture toughness by predeformation is caused by the enhancement of the dislocation nucleation rate at the crack tip. Therefore the experimental data from predeformed specimens is expected to agree better with the numerical results obtained for homogeneous dislocation nucleation than with the results for nucleation at discrete sites. This is verified in Figure 5.2 (compare also with Figure 2.5), where the numerical results for homogeneous nucleation and nucleation at discrete sites are compared. Similar results have been reported for silicon single crystals (Warren, 1989), where predeformation has been shown to increase the low temperature fracture toughness significantly. Predeformation of silicon single crystals also leads to a more gradual BDT, which is in better agreement with numerical simulations than the behavior of undeformed specimens.

Figure 5.2: The numerically determined fracture toughness under the assumption of *homogeneous* dislocation nucleation and nucleation at *discrete* sites is compared. In the case of homogeneous nucleation two different lattice friction stresses τ_{fric} are shown. The loading rate is $\dot{K} = 0.1 \text{ MPa}\sqrt{\text{m}}/\text{s}$ in each case.



A further effect of the warm prestraining is that dislocation motion is obstructed by the dislocation forest. This gives rise to a work hardening of the material. In the simulation this effect can be taken into account by reducing the driving force on each dislocation by subtracting a constant “lattice” friction. As shown in Figure 4.6 a constant lattice friction reduces the fracture toughness at all temperatures. In fact the agreement of experiment and simulation is further improved if a lattice friction is applied (Figure 5.2).

It is therefore concluded that fracture toughness in the low temperature regime is mainly determined by the ability of the crack to produce dislocations. The assumption of an easy

and homogeneous dislocation nucleation at the crack front leads to inconsistencies with experimental observations. First, if dislocation nucleation occurred homogeneously, a reduction of dislocation mobility by predeformation should result in a decrease in fracture toughness. Instead experiment shows an increase in fracture toughness by predeformation, which can only be explained by an enhancement of dislocation generation. Second, simulations under the assumption of homogeneous dislocation nucleation predict a significant loading rate sensitivity, which is not found in experiment. A small stress exponent and a high activation energy could reproduce this vanishing rate sensitivity, but both would be inconsistent with independent experimental investigations of the dislocation motion (Schadler, 1964) and produce problems in explaining the behavior of predeformed material. To obtain more conclusive information on this point, an experimental investigation of the loading rate sensitivity of predeformed material is suggested. In this case, the model, which is favored here, predicts a significantly higher rate sensitivity at low temperatures than for well-annealed material.

5.2 Semi-brittle regime

In this section a quantitative comparison of the fracture toughness as obtained by experiment and numerical simulation is conducted for the different models of dislocation nucleation. The comparison of the loading rate dependence of the fracture toughness at room temperature points towards the importance of crack-tip blunting and dislocation multiplication at intermediate temperatures. Conclusions about the apparent activation energies of crack-tip plasticity and the BDT are derived from the scaling behavior of the numerical results.

5.2.1 Quantitative comparison

Experimentally, the semi-brittle regime is characterized by a strong increase in fracture toughness following the brittle regime. Moreover, in this regime the fracture toughness is strongly rate dependent. In Figures 2.2A and B the slope in the $K^{\text{crit}}-T$ -curve changes abruptly at approximately $T = 200$ K. This change is also seen in Figure 2.4, where the temperature at which this “shoulder” occurs changes with the loading rate. Such a “shoulder” in the $K^{\text{crit}}-T$ -curve is also seen for γ -TiAl single crystals (Booth and Roberts, 1997, Figure 7 therein) and for NiAl polycrystals (Bergmann and Vehoff, 1995, Figure 2 therein). Below the BDT temperature the fracture toughness in tungsten rises steeply for all four low indexed crack systems (Figures 2.2A and B).

In Figure 5.3 the experimental data are plotted together with the numerical results obtained for homogeneous dislocation nucleation, disregarding crack-tip blunting, as well as

the results including nucleation at discrete sites *and* crack-tip blunting. Figure 5.3 shows the results for the loading rates $\dot{K} = 0.1 \text{ MPa}\sqrt{\text{m}}/\text{s}$ (A) and $\dot{K} = 1.0 \text{ MPa}\sqrt{\text{m}}/\text{s}$ (B).

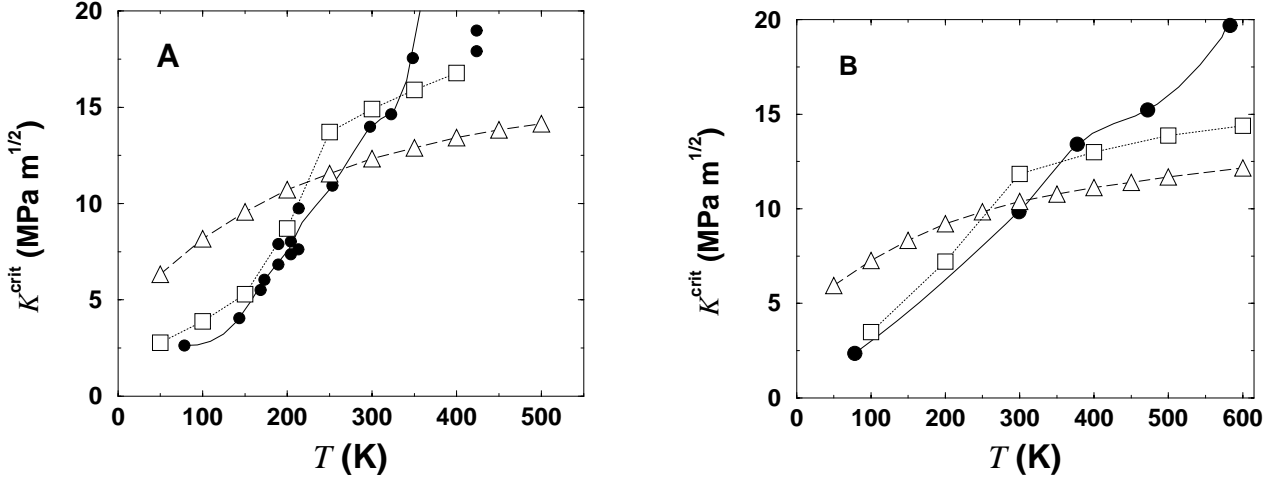


Figure 5.3: Fracture toughness as determined by the simulation (open symbols) compared with experimental data (filled circles) at two different loading rates $\dot{K} = 0.1 \text{ MPa}\sqrt{\text{m}}/\text{s}$ (A) and $\dot{K} = 1.0 \text{ MPa}\sqrt{\text{m}}/\text{s}$ (B). Simulation results are given for homogenous dislocation nucleation (triangles) and dislocation nucleation at discrete sites (squares) respectively. In the latter case crack-tip blunting is taken into account additionally.

As discussed above the assumption of homogeneous dislocation nucleation along the crack front is not justified in the low temperature regime. Consequently, not only the rate sensitivity, but also the absolute value of the fracture toughness is overestimated by these simulations. For temperatures above $T = 300 \text{ K}$ dislocation nucleation occurs (quasi-) homogeneously in both types of simulations. The differences are here due to the disregard of crack-tip blunting. Naturally, the fracture toughness is higher, if crack-tip blunting is taken into account.

It is reassuring that the results of the model, which takes into account dislocation nucleation at discrete sites *and* crack-tip blunting match the experimental data far better than the results of the simplest model (esp. Figure 5.3A). However, the refinement of the model is not high enough to allow for the quantitative prediction of fracture toughnesses. Because the model parameter δ is rate independent, and has been chosen to meet the conditions at the lower loading rate, the differences between experiment and simulation become slightly more pronounced at higher loading rates.

A special feature of the experimental data is the "S"-shaped change of slope or "shoulder" in the $K^{\text{crit}}-T$ -curve. The numerical results, too, show such a change of slope where the density of nucleation sites along the crack front saturates and dislocation nucleation becomes quasi-homogeneous. A *post-mortem* investigation of fracture surfaces could provide insight

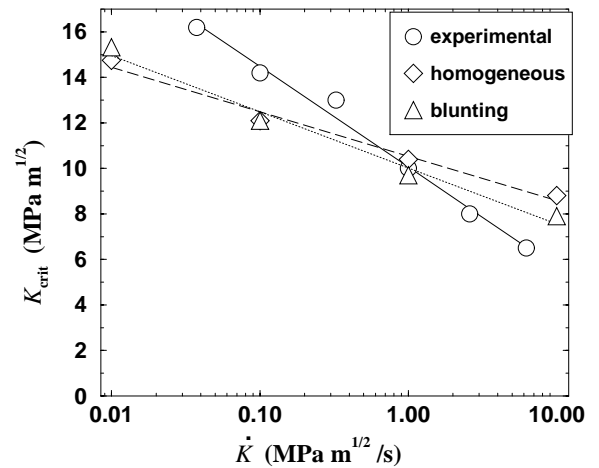
if the “shoulder” in the experimental results is caused by a similar saturation of dislocation sources.

It is noted here that the results obtained for screw dislocation velocity yield a far less satisfactory agreement between experiment and simulation. In the temperature regime under consideration the calculated fracture toughnesses are too low. Moreover the slope of the $K^{\text{crit}}-T$ -curve is too shallow due to the high activation energy of screw dislocations.

5.2.2 Rate dependence and crack-tip blunting

The loading rate sensitivity of the experimental data and the results of the simulation, both taken at room temperature, is compared in Figure 5.4. The experimental data from Riedle (1995) shows a logarithmic loading rate dependence of the fracture toughness. Simulations for homogeneous dislocation nucleation as well as nucleation at discrete sites with blunting also give a logarithmic loading rate dependence of the fracture toughness. However, the loading rate dependence of the simulated data points is far smaller than that of the experimental data points. The discrepancy can partly be explained by the lack of dislocation multiplication processes in the numerical model. Taking into account dislocation multiplication would presumably lead to higher fracture toughnesses at smaller loading rates, because dislocations would have more time to multiply under these conditions.

Figure 5.4: Fracture toughness K^{crit} at room temperature as a function of the loading rate \dot{K} ($\text{MPa}\sqrt{\text{m}}/\text{s}$). *Experimental* data is compared with numerical results accordingly obtained for *homogeneous* nucleation and nucleation at discrete sites combined with *blunting*.



Taking into account dislocation nucleation at discrete sites and crack-tip blunting gives a slightly lower fracture toughness at high loading rates, because the density of sources is not completely saturated at this temperature. At lower loading rates the increase in toughness by blunting is stronger than the embrittlement by nucleation at discrete sites. This indicates that taking into account the blunting of the crack tip increases preferentially the fracture toughness at lower loading rates, which can be understood as a self-amplifying effect of the

blunting: A larger number of emitted dislocation increases the critical local fracture toughness. Therefore the time-to-fracture is increased and still more dislocations are nucleated.

A better understanding of the temperature and loading rate dependence of the model parameter δ would probably enhance the agreement between experiment and simulation. This is indicated by the results of the 3D simulation (Section 4.2.1), where a slight increase of δ with the loading rate was found. An extraction of quantitative values of the rate dependence of δ was not possible within the frame of this work. In any case, experimental evidence is such that at room temperature the dislocation sites are almost dense along the crack front. Therefore, this influence on fracture toughness and its loading rate dependence can be presumed to be moderate, at least for low loading rates.

The importance of crack-tip blunting for the BDT gives a further motivation for the proposed model of dislocation nucleation, because dislocations on oblique slip planes do not blunt the crack tip. This is only achieved by dislocation gliding on blunting slip planes. Since the nucleation in the blunting configuration is more difficult than in the non-blunting configuration, the proposed cross-slip mechanism combines the advantages of both nucleation modes.

5.2.3 Scaling behavior

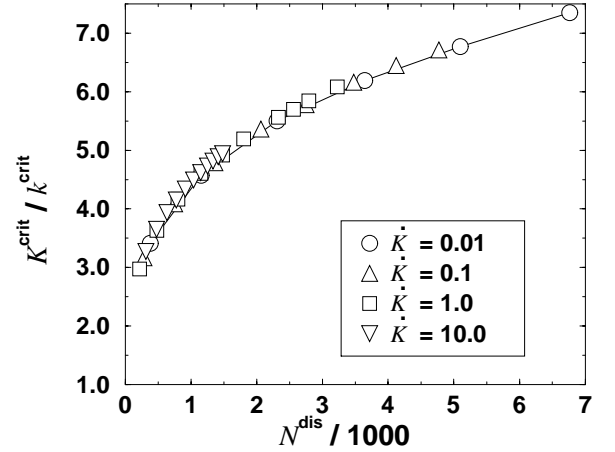
The Arrhenius relation expressed in Equation (2.12) is interpreted here as a scaling relation between the loading rate and the BDT temperature. As seen in Figure 2.4, the BDT in tungsten occurs approximately at a constant fracture toughness. Accordingly the BDT temperature is sometimes defined as the temperature where the fracture toughness exceeds a given limit. On this basis a more general scaling law can be derived for all points of constant fracture toughness on $K^{\text{crit}}-T$ -curves obtained for different loading rates.

A further argument for such a generalized scaling relation is that the fracture toughness is mainly determined by plastic relaxation, which is described by an Orowan law [Equation (2.1)]. While the Arrhenius law relates the loading rate with a thermal activation term, the Orowan law relates the strain rate with a thermal activation term of the same form. Therefore a relation between temperature and loading rate can be expected at points of constant fracture toughness, where consequently the same amount of plastic relaxation has occurred.

The relation between fracture toughness and plastic relaxation is visualized in Figure 5.5 where the fracture toughness is plotted against the number of dislocations that were emitted when failure occurred, *i.e.* when the local stress intensity at the crack tip exceeded $k^{\text{crit}} = 2.0 \text{ MPa}\sqrt{\text{m}}$. The points obtained for different loading rates can be connected by a single smooth line (master curve). Simulations in which an equal number of dislocations

is emitted show practically an equal fracture toughness. This means that a constant number of dislocations results in a comparable amount of shielding, even if the conditions of the calculations have been different. Therefore it can be concluded that the dynamics in the inverse dislocation pile-up is comparable if a constant fracture toughness is reached. This supports the assumption that loading rate and temperature are strongly correlated at points of constant fracture toughness.

Figure 5.5: Relative fracture toughness $K^{\text{crit}}/k^{\text{crit}}$ versus number N^{dis} of emitted dislocations at failure. The points obtained for different loading rates \dot{K} (in $\text{MPa}\sqrt{\text{m}}/\text{s}$) all fall on a master curve. The data points correspond to Figures 4.4 and 4.5.



Whether this result is completely due to the simplicity of the applied model or a principal symmetry in nature cannot be clarified here. If this relation is accepted, it follows that two specimens that are broken under different conditions, but reveal the same fracture toughness, will have a similar dislocation microstructure in the crack-tip region.

An implicit formulation of this generalized scaling relation between loading rates \dot{K}_i and temperatures T_i at which a given fracture toughness K^{crit} is reached ($i \in \mathbb{N}$) reads

$$K^{\text{crit}}(\dot{K}_i, T_i) = \text{const.} \quad (5.1)$$

It is evident that this equation cannot be fulfilled for every K^{crit} in the set of results if \dot{K}_i and T_i are unrelated. The relation between these two quantities is the desired scaling relation.

A generalization of the Arrhenius law for combinations of (\dot{K}_i, T_i) with the same fracture toughness K^{crit} is obtained by replacing the BDT temperature in Equation (2.12) with the temperature T_i . For two different temperatures at two different loading rates this yields the system of equations

$$\dot{K}_1 = A \exp\left(-\frac{U_{\text{BDT}}}{k_B T_1}\right) \quad \text{and} \quad (5.2)$$

$$\dot{K}_2 = A \exp\left(-\frac{U_{\text{BDT}}}{k_B T_2}\right). \quad (5.3)$$

Dividing Equation (5.3) by Equation (5.2), and solving with respect to T_2 gives

$$T_2 = \left[\frac{k_B}{U_{\text{BDT}}} \ln \frac{\dot{K}_1}{\dot{K}_2} + \frac{1}{T_1} \right]^{-1}. \quad (5.4)$$

Provided the validity of this scaling law, every $K^{\text{crit}}-T$ -curve obtained for loading rate \dot{K}_1 can be transformed into a $K^{\text{crit}}-T$ -curve for the loading rate \dot{K}_2 through an appropriate scaling of the temperature axis. Because the apparent activation energy for the BDT is a parameter of this scaling relation, it can be used in the sense of a fit parameter in the scaling procedure of the numerical results of the 2D simulations. By an appropriate scaling of the numerical results, thus, the the apparent activation energy for the BDT can be extracted, although the numerical results do not show a transition to plastic behavior due to the inherent simplifications of the 2D model. In a more rigorous sense, the resulting activation energy is the apparent activation energy for crack-tip plasticity rather than that for the BDT. However, as has been motivated above that these two activation energies should coincide.

It is possible to reformulate the scaling law with respect to the activation energies. This gives the relation

$$U_2 = \left[k_B T \log \frac{\dot{K}_1}{\dot{K}_2} + U_1 \right], \quad (5.5)$$

which has been used in Section 4.2.1 to scale down the activation energy for screw dislocation motion to enable simulations to be performed at higher loading rates.

In Figures 5.6 A and B the scaling is demonstrated for an edge-type mobility law with constant stress exponent m [Equation (2.10)] for two different activation energies for dislocation motion. Here and in all following cases, the smallest loading rate for which data are available is chosen to be the basis loading rate \dot{K}_2 . The data pairs (T_1, K^{crit}) for the higher loading rates \dot{K}_1 are then transformed according to Equation (5.4) into pairs (T_2, K^{crit}) , which are all plotted into a single graph. In Figure 5.6 it is shown, that the scaled data points obtained for a constant stress exponent m fall on on a single curve (master curve). The scaling procedure has been performed with a constant energy U_{BDT} , which is interpreted as the apparent activation energy for the BDT. In all investigated cases, this energy corresponds to the activation energy for dislocation glide, *i.e.* $U_{\text{BDT}} = Q_{\text{dis}}$. This result is non-trivial for stress exponents $m \neq 1$, because it is not clear *a priori* whether the coupling of the crack-tip plastic zone to the far field stress is based on stress or strain.

For non-screw-type mobility laws with a temperature dependent stress exponent [Equation (2.10) with the parameters from Table 2.3] this strict scaling behavior brakes down. Figure 5.7 shows that the scaling with a constant activation energy does not exactly project the points for different loading rates on a master curve. Also the activation energy used in the scaling relation is considerably smaller than the activation energy for dislocation motion ($U_{\text{BDT}} = 0.12$ eV compared with $Q_{\text{dis}} = 0.32$ eV). This is attributed to the temperature dependence of the stress exponent, which is quite strong in this temperature regime. However this value is a little higher than the apparent activation energy for the BDT $U_{\text{BDT}} = 0.09$ eV

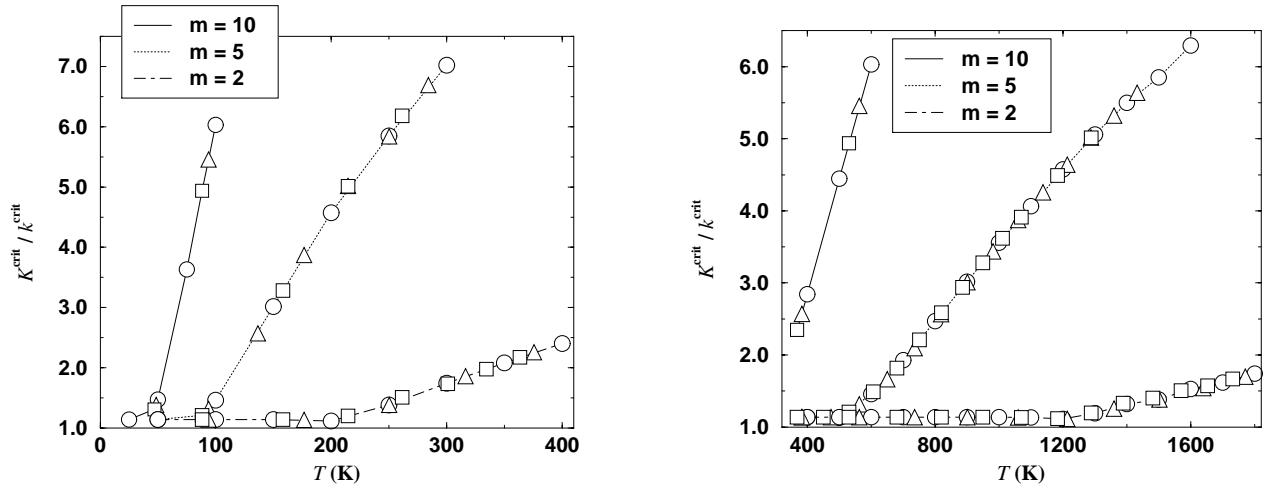
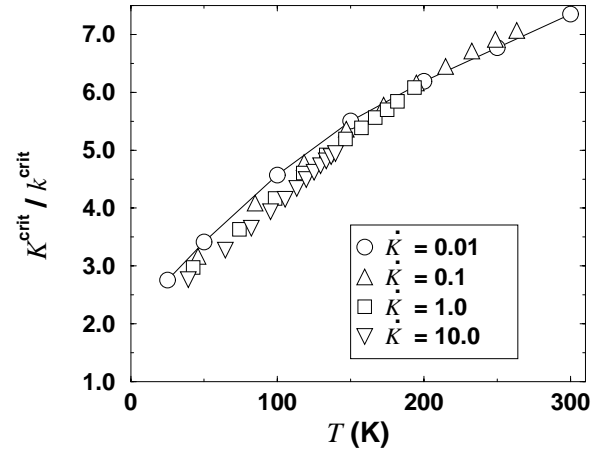


Figure 5.6: The fracture toughness values obtained for different loading rates are plotted on a single master curve by scaling the temperature axis of each curve according to Equation (5.4). Two different activation energies for dislocation motion have been investigated: $Q_{\text{dis}} = 0.3$ eV (A) and $Q_{\text{dis}} = 1.8$ eV (B). Different symbols are used for the loading rates: circles: $\dot{K} = 0.1$ MPa $\sqrt{\text{m}}/\text{s}$, triangles: $\dot{K} = 1.0$ MPa $\sqrt{\text{m}}/\text{s}$, squares: $\dot{K} = 10$ MPa $\sqrt{\text{m}}/\text{s}$. All data points are scaled according to Equation (5.4) to the master curve with $\dot{K}_2 = 0.1$ MPa $\sqrt{\text{m}}/\text{s}$.

obtained by the finite element model which uses the characteristics on non-screw dislocation mobility (Section 4.4).

Figure 5.7: The fracture toughness resulting from the numerical simulations with non-screw type dislocation mobility with parameters mimicking tungsten plotted against the scaled temperature according to Equation (5.4). A temperature dependent stress exponent is assumed. All loading rates \dot{K} are given in MPa $\sqrt{\text{m}}/\text{s}$. The basis loading rate for the scaling was set to $\dot{K}_2 = 0.01$ MPa $\sqrt{\text{m}}/\text{s}$.



If a higher activation energy for dislocation motion is employed, the temperature range where plasticity occurs is correspondingly higher. At elevated temperatures the variation of the stress exponent with temperature is less strong than at low temperatures. Therefore the scaling relation is obeyed more strictly in this temperature regime, even for temperature dependent stress exponents (Hartmaier and Gumbsch, 1997).

For a screw-type mobility law [Equation (2.5)] it is seen that the scaling of the results is not as strict as for the results obtained for a non-screw type mobility law with constant

stress exponent (Figure 5.8). The scaling shown in Figure 5.8 was performed with an activation energy $U_{\text{BDT}} = 1.4 \text{ eV}$, which is considerably smaller than the activation energy for dislocation motion $H_{\text{screw}} = 1.8 \text{ eV}$.

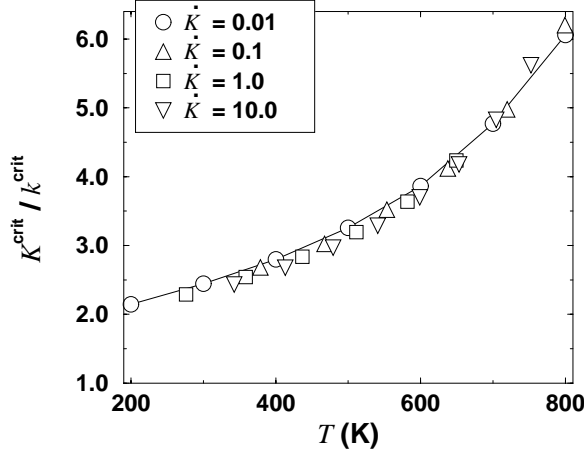


Figure 5.8: The fracture toughness resulting from the numerical simulations with screw type dislocation mobility plotted against the scaled temperature according to Equation (5.4). The symbols for the different loading rates correspond to Figure 5.7.

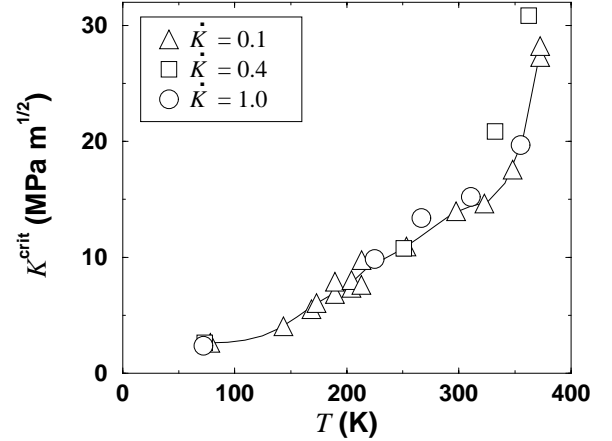


Figure 5.9: The scaling behavior of the experimental $K^{\text{crit}}-T$ -curves is described by an Arrhenius-type law [Equation (5.4)] with an apparent activation energy of $U_{\text{BDT}} = 0.19 \text{ eV}$. All loading rates \dot{K} are given in $\text{MPa}\sqrt{\text{m}}/\text{s}$. The basis loading rate for the scaling was set to $\dot{K}_2 = 0.1 \text{ MPa}\sqrt{\text{m}}/\text{s}$.

Finally, it is seen in Figure 5.9 that the experimentally determined fracture toughness of tungsten single crystals scales according to Equation (5.4) over the whole temperature range where dislocation motion is assumed to control fracture toughness. The scaling of the curves reveals an apparent activation energy of $U_{\text{BDT}} = 0.19 \text{ eV}$, which is equal to the activation energy for the BDT that is derived from the BDT temperatures for the different loading rates (Section 2.3.3).

In this section the close relation of loading rate and temperature has been shown. This close relation is expected for a strictly thermally activated process. It has also been shown that the Arrhenius-like scaling relation is only fulfilled approximately if the stress exponent is temperature dependent or if a stress dependent activation enthalpy is considered.

The systems under consideration here are highly driven and far from thermal equilibrium. The coupling of the applied stress (intensity) rate to the strain rate in the crack tip region is performed by the dislocation mobility law, which hence is responsible for the scaling behavior of the results. Dislocation velocity also controls the rate at which new dislocations are generated, because the back stress of a newly nucleated dislocation suppresses further

nucleation events until the dislocation has moved sufficiently far from the crack tip. In this work no additional barrier to dislocation nucleation is considered.

In the previous section it has already been shown that the assumption of easy and homogeneous dislocation nucleation is problematic if the number of active sources at the crack tip is insufficient. For tungsten this restriction seems to be important only below room temperature. The scaling behavior of the experimental results for this material confirms that a thermal activation of crack-tip plasticity is given. Moreover the activation energy is equal to that of the BDT derived from the loading rate dependence of the BDT temperature. This supports *a posteriori* the assumption made for the derivation of the generalized scaling relation.

The activation energy of $U_{\text{BDT}} = 0.2 \text{ eV}$ could not yet be attributed to an elementary process of dislocation motion. Hence it cannot be excluded that this activation energy is correlated with the process of dislocation nucleation or other elementary dislocation processes like cross-slip. If however dislocation nucleation were limiting, then dislocation motion would occur easier than dislocation nucleation. This means that the dislocations in average would be more remote from the crack-tip and thus produce a less efficient shielding than for a mobility controlled process. Therefore the predicted fracture toughnesses would lie below those of the mobility limited model presented in this work.

It can be stated here with sufficient certainty that crack-tip plasticity in tungsten is not limited by the motion of screw dislocations. The activation energy for screw dislocation motion is much higher than the activation energy for crack-tip plasticity. Moreover the assumption of such a high activation energy would shift the semi-brittle regime to higher temperatures. This argument is further supported by the observation that the experimentally determined BDT temperatures in tungsten (Riedle, 1995) are below the so-called “knee” temperature $T_{\text{knee}} = 600 \text{ K}$ (Brunner, 1998). Commonly this “knee” temperature is regarded as the temperature where screw dislocations become mobile and no longer limit the plastic deformation of the material (Argon and Maloof, 1966; Seeger, 1981). This result can be assumed to be also valid in other bcc materials.

The rather explicit nucleation and cross-slip process proposed in this work (Section 3.2.3) explains why the crack tip is a fertile source of non-blunting dislocations on blunting slip planes. Despite its shortcomings, this nucleation mechanism provides a quite natural explanation for the experimental findings. The model only assumes that dislocations, once they are nucleated at ledges in the crack front on non-blunting slip planes, are flexible enough to follow the path given by the highest driving force and “unzip” in the high stress field along the crack front.

5.3 Brittle-to-ductile transition

The comparison of experimental and numerical results has shown the importance of dislocation nucleation for the low temperature fracture toughness. It also has become evident that any physical model for the BDT must necessarily include dislocation mobility, and cannot exclusively be based on dislocation nucleation. Indeed, the discussion of the previous section has led to the conclusion that dislocation mobility is the major factor controlling fracture toughness in the semi-brittle regime. However, right below the BDT temperature a strong increase in fracture toughness is observed in the experimental data on tungsten single crystals (Figures 2.2A and B).

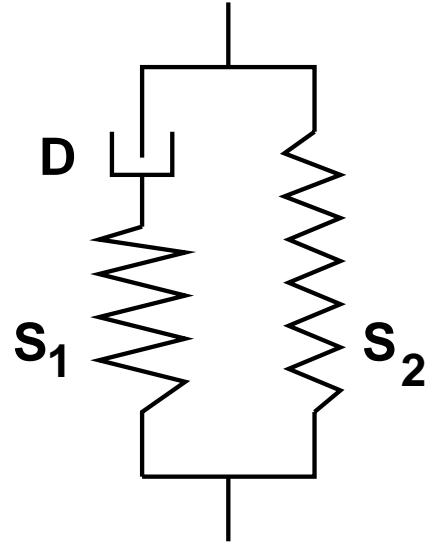
This abrupt increase is not found in the results of the discrete dislocation simulation. Even if crack-tip blunting is taken into account in a rudimentary way, the DDD model does not yield a sufficiently strong self-amplification of crack-tip plasticity to show a BDT. Still such a self-amplifying process cannot be excluded by the present investigation, due to its severe simplifications, especially with respect to crack-tip blunting and dislocation nucleation. Moreover, any kind of dislocation multiplication is disregarded in the DDD model.

The model proposed by Khanta, Pope, and Vitek (Khantha et al., 1995) of a sudden increase in the dislocation density caused by a Kosterlitz-Thouless-type instability, predicts a very steep increase in fracture toughness. However, in the form in which it is published, the model can neither explain the experimentally observed rate dependence of the BDT, nor the increase in the BDT temperature with predeformation. In contrast it would predict a reduced BDT temperature for a predeformed material.

The 2D finite element model of crack-tip plasticity proposed by Nitzsche and Hsia (1994) shows a sudden BDT similar to the experimentally observed BDT of silicon (St. John, 1975; Brede and Haasen, 1988; Samuels and Roberts, 1989). This model has been adapted to tungsten where also an abrupt BDT is determined (Section 4.4). The continuum plasticity model can be visualized by the rheological model shown in Figure 5.10. The stiff, breakable spring S_1 is loaded in series with the dashpot D . Spring S_2 , which is unbreakable and less stiff than S_1 , is loaded parallel to the system D - S_1 .

Spring S_1 can be rationalized as the elastic zone around the crack tip. If the relaxation in the dashpot occurs slowly, almost all the load is transmitted to spring S_1 which fails at a given load. The dashpot consequently relates to the viscoplastic zone. The stress that drives the viscoplastic relaxation in dashpot D is always equal to the stress transmitted by spring S_1 . If the plastic strain of the dashpot increases with a sufficient rate, spring S_2 transmits the main part of the applied load and thus relieves spring S_1 . Spring S_2 corresponds to the

Figure 5.10: Rheological model representing the continuum model of crack-tip plasticity. S_1 represents a stiff, breakable spring, S_2 is a less stiff, unbreakable spring, and D is a dashpot.



elastic zone around the viscoplastic zone. This spring is considered unbreakable and can transmit any given load.

The loading of “spring” and “dashpot” of the crack problem, however, occurs in a geometrically complex manner. In this simplistic reduction of this model, the BDT occurs when the stress relaxation in the dashpot takes place with the same rate at which the applied load is increased. The rate of the relaxation depends on temperature and on the stress in the dashpot, as described by Equation (4.3). The maximum stress that can occur in the system D - S_1 is given by the failure stress of spring S_1 . Thus, the BDT takes place if the temperature is high enough such that the rate of plastic relaxation at or below the failure stress is equal to the applied rate.

A closer investigation of the geometrically complex loading of the elastic zone (spring) embedded in the viscoplastic material (dashpot) shows that the plastic zone expands around the elastic zone and the region of the highest plastic strains moves towards the crack surface. Simulations resulting in ductile behavior always show that the highest plastic strains occur close to the corner of the elastic zone on the crack plane.

This leads to a physical interpretation of the model: The elastic zone can be understood as a “test-crack” in front of the “real” crack tip. If the crack tip, *i.e.* the corner of the elastic zone, blunts fast enough, the test-crack cannot proceed further. If, in contrast, the blunting is too slow, the critical load on the test-crack will be exceeded at some stage and brittle crack advance will occur. Obviously, the conditions for which a transition between these two types of behavior occurs depend on the size of the test-crack, which defines the size of the elastic zone. If the test-crack is larger, plastic relaxation occurs later and with a slower rate. Therefore, crack advance of larger test cracks is easier and the BDT temperature is higher.

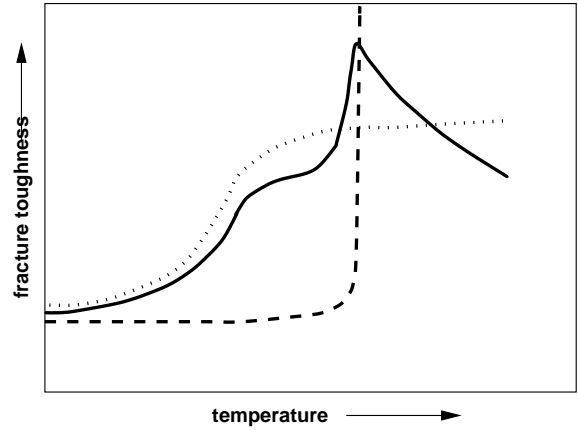
This interpretation already indicates the importance of crack-tip blunting for the BDT. The absence of a semi-brittle regime in this model is explained by the absence of plastic shielding at low and intermediate temperatures, due to the spatial separation of the plastic zone from the crack tip. This shielding, in contrast, is taken into account by the 2D-DDD model, which consequently shows a pronounced semi-brittle regime. It is further seen from the DDD results, that the blunting of the crack tip has a limited effect in the semi-brittle regime. The importance of blunting increases at higher fracture toughnesses, where the notch radius of the blunted crack tip becomes larger.

A drawback of this interpretation is the circular shape of the elastic zone. If the elastic zone is interpreted as a brittle inclusion in a viscoplastic matrix, the circular shape seems to be appropriate, but the crack front should be at the boundary rather than in the middle of the inclusion. If, in contrast, the elastic zone is interpreted as a test crack in the viscoplastic material, the occurring of a circular elastic zone seems rather arbitrary.

The apparent activation energy for the BDT obtained from this model is the same as that for bulk plasticity. This seems to exclude this model as a possible explanation for the steep increase in fracture toughness below the BDT temperature, because bulk plasticity in bcc materials is governed by screw dislocation motion. The activation energy for the BDT in tungsten is one order of magnitude lower than the activation energy for screw dislocation motion. However, the total plastic strain needed to achieve a BDT in the 2D-FEM model remains below 5%. This amount of plastic strain in bcc materials can be ascribed to microplasticity, *i.e.* plasticity that occurs without the large scale motion of screw dislocations. As assumed by the nucleation model proposed in this work (Section 3.2.3), the crack tip is a fertile source of dislocations, whose screw parts only move in the highly stressed crack-tip region, creating non-screw dislocations on blunting slip planes. Therefore plastic strains of 5% seem to be achievable without the motion of screw dislocations in the far field.

A final answer towards the decisive mechanism of the BDT cannot be provided within the frame of this work. Further experimental investigations of the blunting radius as a function of fracture toughness could provide more conclusive data if self-amplified crack-tip blunting is responsible for the BDT. The KPV-model does not necessarily predict a strong increase of the blunting radius at the BDT, because plasticity in this model is produced in a larger volume of the crack-tip region. If in contrast dislocation nucleation occurs preferentially at the crack tip, the blunting radius will show a significant increase parallel to the strong increase in fracture toughness at the BDT temperature.

Figure 5.11: Schematic drawing of typical fracture toughness versus temperature curves discussed in this work. Experimental findings (solid line) are compared with results of the discrete dislocation model (dotted line) and the continuum plasticity model (dashed line).



5.4 Summary

Figure 5.11 shows schematic drawings of typical fracture toughness versus temperature curves discussed in this work. This figure shows that the development of fracture toughness with temperature can be described on the basis of discrete dislocation models at low and intermediate temperatures. The comparison of the model predictions with experimental results showed that there is a transition in the mechanism controlling crack-tip plasticity. At very low temperatures it is the lack of active dislocation sources and thus dislocation nucleation that limits ductility. As temperature rises and the number of active sources increases, dislocation mobility starts to limit fracture toughness. The dislocations, which are generated in larger numbers, cannot leave the crack-tip region fast enough and thus inhibit the instantaneous nucleation of further dislocations.

At still higher temperatures the discrete dislocation models as applied in this work lose their validity, because dislocation multiplication is not taken into account. This temperature regime close to the BDT is the realm of continuum plasticity models, which are able to describe the BDT itself. At lower temperatures, in contrast, the results of the continuum plasticity models are not valid because they are not suited to describe the detailed dislocation nucleation mechanisms at the crack tip. Since a description of dislocation nucleation is not possible within the continuum model, no firm conclusion can be drawn whether it is dislocation nucleation or dislocation mobility that controls the BDT. However, it seems to become clear that the blunting of the crack tip by plastic deformation plays an important role for the BDT. Further, the comparison of model predictions of the continuum model as well as those of the discrete dislocation model with experimental results showed that screw dislocations cannot be limiting crack-tip plasticity. The detailed nucleation and cross-slip mechanism proposed in this work motivates the description of crack-tip plasticity as microplastic deformation, which is carried by non-screw dislocations.

5.5 Criticism of the applied methods

After the physical content of the numerical results has been discussed, the methods that have been applied in this work are critically reviewed in this section.

5.5.1 2D discrete dislocation model

The 2D DDD-model has proven a powerful tool to describe crack-tip plasticity in the semi-brittle regime. Its capability to predict macroscopic quantities that can immediately be compared with experimental data allowed far reaching general conclusions to be drawn. However, this capability to operate on the macroscopic level enforced the geometrical restriction to an edge-on description of the crack tip and the dislocations and the disregard of dislocation multiplication. Moreover, the use of a number of model parameters has been necessary to describe dislocation motion, dislocation nucleation and crack-tip blunting.

The parameters describing dislocation mobility all have a physical meaning and can therefore – in principle – be extracted from experiment or more specific theories. However, the specific data necessary for this investigation had to be interpolated over a large range. More reliable data and theories, especially describing the mobility of non-screw dislocations, would help to increase the predictative power of this model.

The model parameter δ and the constant C , describing the influence of the discrete sources and of crack-tip blunting on the local stress intensity, must be considered as fitting parameters with unclear physical meaning. A detailed description of dislocation nucleation at discrete sources is only possible by a fully 3D method and on smaller length and time scales. If the information gained by such an investigation could be transferred to the 2D model, a better description of the low-temperature regime would be possible. The influence of blunting is mainly of interest at elevated temperatures. A coupled DDD-continuum description as proposed by Cleveringa et al. (1997) is a very promising way to incorporate this effect into a 2D simulation.

A further disadvantage of the 2D method is that the implementation of an activation energy or an activation volume for dislocation nucleation is difficult. Such an activation barrier results in a nucleation criterion incorporating the shear components of the stress intensity (Schoeck, 1991). Such shear components in the stress intensity occur locally at imperfections in the crack front, but do not arise from a straight crack loaded under pure mode-I conditions. A mixed mode loading of the crack tip increases the number of model parameters and is only of limited value for the physical understanding of crack-tip plasticity. The internal stresses on the crack front arising from the dislocation population are too small to enable an energy-based dislocation nucleation criterion.

5.5.2 3D discrete dislocation model

While in two dimensions it was possible to derive a closed formulation for the stress field of a dislocation in an infinite medium with a semi-infinite crack, such a formula for the general case of an arbitrarily oriented dislocation segment of finite length in three dimensions is beyond the state of the art. The use of equations derived for an infinite medium is problematic, because the implementation of the correct boundary conditions yields conceptual problems. The direct interaction of a segment with the crack can be estimated reasonably well by an image force. However, the interaction of dislocations is different in the presence of a free surface and the error by disregarding this effect is not necessarily small (Section 3.2.1). Moreover, the topology of space is altered by the crack, *i.e.* the distance of interaction of dislocations above with dislocations below the crack plane is not the same as in a coherent space. This makes it very difficult to use coupled DDD-continuum methods.

Another shortcoming of the 3D method as it is applied here is that dislocation lines are discretized into pairwise orthogonal segments. This discretization makes it necessary to introduce a lower discretization length. In the high stress gradient close to the crack tip such a rigid discretization will always have an influence on the velocity of the dislocation segments. As explained in Section 3.2.1, a fine discretization length is desirable to get the correct dynamical evolution of the dislocation population close to the crack front. On the other hand, a fine discretization may produce artifacts in the dislocation self-interaction term, see the discussion in Appendix B.

Since the 3D-DDD method operates on smaller length scales than the 2D method, a shorter time step must also be used. This short time step makes it difficult to calculate macroscopic quantities. Furthermore the concept of stress intensity and shielding has been derived for a straight crack front that is homogeneously loaded. For a 3D study a reliable concept of a varying dislocation shielding along the crack front needs to be derived. Gao (1989) has already introduced such ideas, but not in a form suitable for numerical DDD models.

A 3D description of dislocation motion in the stress field at the crack-tip, and especially in that of imperfections in the crack front, offers the chance to better understand the process of dislocation nucleation at the crack tip. The stress field of such imperfections can be calculated with finite element methods, as shown in Section 3.2.3. It is known that the solution of the FE calculation is imprecise at locations close to the crack tip singularity. The exact value of the stress in this region is always dependent on the resolution of the mesh. However, the DDD simulation does not require the knowledge of the stress very close to the crack tip for two reasons: (i) large scale dislocation motion is not possible within the zone of instability, (ii) if the stress is beyond a certain level, the dislocation velocity approaches

its physical limit of the shear wave velocity.¹ Indeed, to assure numerical stability, the dislocation velocities are capped at 10% of this value. The larger of the two limits (i) and (ii) defines the region within which the precise knowledge of stress is not necessary to perform DDD simulations. The incorporation of imperfections in the crack front allows the shear components of the stress field to be considered, and thus could enable an energy-based dislocation nucleation criterion. Therefore it is considered worthwhile to continue the development of the 3D-DDD method.

5.5.3 2D continuum plasticity model

The finite element model with rate-dependent viscoplastic material behavior gave a clear idea of the interaction between the applied rate of increase in stress intensity and the strain rate the material can sustain. A shortcoming of this method is the concept of the elastic zone. The shape and size of this elastic zone must be set arbitrarily, but has a quite pronounced influence on the results. Furthermore the application of continuum plasticity can be problematic in the vicinity of a crack tip, because it is not clear if dislocation cross-slip and multiplication operate in the same way as in the bulk.

5.6 Outlook

Several ideas how this work could be extended and improved have already been presented in the respective sections. Three points shall be stressed here in summary:

(i) A more reliable theory and more detailed experimental investigations of dislocation motion in bcc materials, especially the motion of non-screw dislocations, are essential for a dynamical discrete dislocation description of crack-tip plasticity.

(ii) A three dimensional DDD or atomistic description of dislocation nucleation from ledges or jogs in the crack front in connection with the ongoing experimental work (Baither et al., 1999) could clarify the issues raised in the discussion of the low-temperature dislocation nucleation limited regime.

(iii) Experimental investigations of fracture of predeformed material holds great promise to shed some light on the open questions of dislocation nucleation and multiplication in the crack tip region. An immediate prediction of the 2D-DDD model employed in this work is that predeformed specimens should exhibit a significant loading rate dependence even at low temperature, because dislocation nucleation should occur more easily than in

¹Elasticity theory shows that there exist solutions for dislocation motion beyond the shear wave velocity, however dislocations cannot be accelerated to such velocities, but have to be generated in this velocity regime (Gumbsch and Gai, 1999).

dislocation-free material. Moreover, by prestraining up to various amounts of plastic strain and at various temperatures the dislocation microstructure can be adjusted on purpose. These investigation could therefore distinguish between the role of screw and non-screw dislocations. An investigation of the crack-tip radius as a function of fracture toughness could give conclusive data on whether the dislocations are mainly nucleated close to the crack tip or in a larger region.

Chapter 6

Conclusions

In this work crack-tip plasticity has been investigated with a 2D dislocation dynamics simulation scheme. From the comparison of the numerical results obtained in this work with experimental data on tungsten single crystals (Riedle, 1995) it could be concluded that crack-tip plasticity at low temperatures is limited by the nucleation of dislocations. At higher temperatures dislocation mobility must be taken into account as an important factor to explain the experimental findings. A model assuming a purely *mobility controlled* microplastic deformation of the crack-tip region has been shown to be consistent with a number of experimental results at elevated temperatures. The blunting of the crack tip has a pronounced influence on the fracture toughness in the semi-brittle regime and is proposed to be of great importance for the brittle-to-ductile transition (BDT).

Concerning the question, whether it is dislocation generation or dislocation motion that limits crack-tip plasticity, a firm answer can be given for the low-temperature regime. The predictions of the purely mobility controlled model, where dislocation nucleation is assumed to occur homogeneously along the crack front without an energetic barrier, are not consistent with the experimental findings on tungsten single crystals: First, the mobility controlled model predicts a significant loading rate sensitivity of fracture toughness at low temperatures, which is in direct contradiction with the experimental results. Second, if dislocation nucleation occurred easily even at low temperatures, then it is difficult to understand why predeformation increases the fracture toughness in single crystalline material at these temperatures. The increase in fracture toughness by predeformation can most convincingly be explained by assuming that dislocation nucleation limits crack-tip plasticity in well-annealed material and that dislocation nucleation is facilitated by predeformation.

This explanation is also consistent with results from experiments on dislocation-free silicon single crystals, where it is found that almost no plasticity is activated right up to the BDT temperature. After predeformation this material shows a well-developed semi-brittle transition regime with a slowly increasing fracture toughness.

In the semi-brittle regime of tungsten, where experimental investigations reveal a strong loading rate sensitivity, the 2D dislocation dynamics model underestimates the rate sensitivity of fracture toughness. If the blunting of the crack-tip by plastic deformation is taken into account, the numerical results yield a more pronounced loading rate sensitivity, which is however still below that found in experiment. More quantitative conclusions in this respect have not been possible due to the restrictions of the applied model. Dislocation multiplication does probably play an important role in this regime.

From the scaling behavior of the numerically determined fracture toughness with loading rate and temperature important conclusions on the activation energy of plasticity in the crack-tip region are drawn. This activation energy, which can be presumed to be identical with the activation energy for the BDT, proves to be equal or close to the activation energy for dislocation motion. The quality of agreement of these quantities, however, depends on the specifics of the equation describing dislocation mobility.

Experiments show (Ziebart, 1986; Brunner, 1998) that the activation energy for screw dislocation motion in tungsten is one order of magnitude higher than the activation energy determined by the BDT temperature. The latter agrees well with the activation energy associated with the scaling relation for the fracture toughness-temperature curves. Therefore it can be concluded that – in contrast to bulk plasticity – crack-tip plasticity in this material is *not* limited by screw dislocation motion. Resulting from the high activation energy for screw dislocation motion, the simulations assuming the limitation of crack-tip plasticity by screw dislocation mobility yield a significant increase in fracture toughness only at very high temperatures. These temperatures are far beyond the experimentally determined BDT temperature of tungsten.

In the semi-brittle regime, the 2D dislocation dynamics simulations, which consider microplastic deformation of the crack-tip region by non-screw dislocations, yield results that are quantitatively comparable to the experimental data.

The assumption of a purely microplastic deformation of the crack-tip is also consistent with a continuum plasticity model. If the temperature is high enough or the loading rate low enough, the time-dependent plastic deformation of the crack-tip region as calculated within this model can sustain a given loading rate without failure. This property is used to define the BDT. The plastic strains at the BDT are small enough to be explained by microplasticity. The importance of crack-tip blunting for the BDT is further confirmed by this continuum model.

It can be presumed that the results obtained for tungsten, *i.e.* nucleation control at low temperatures, microplasticity in the semi-brittle regime, and the importance of dislocation mobility and blunting for the BDT, are in general also valid for other transition metals. For

ceramics and semi-conductors dislocation nucleation is most probably even more difficult than in transition metals for all temperatures. Therefore the purely nucleation limited regime may extend to higher temperatures, possibly right up to the BDT temperature.

Bibliography

- Abraham, F. F. (1997), ‘On the transition from brittle to plastic failure in breaking a nanocrystal under tension’, *Europhysics Lett.* **38**, 103–106.
- Abraham, F. F., D. Schneider, B. Land, D. Lifka, J. Skovira, J. Gerner and M. Rosendrantz (1997), ‘Instability dynamics in three-dimensional fracture: an atomistic approach’, *Journal of the Mechanics and Physics of Solids* **45**, 1461–1471.
- Alexander, H., C. Kisielowski-Kemmerich and A. T. Swalski (1987), ‘On the stress dependence of the dislocation velocity in silicon’, *physica status solidi (a)* **104**, 183–192.
- Anderson, P. M. and J. R. Rice (1987), *Journal of the Mechanics and Physics of Solids* **35**, 743.
- Ansys Manual* (n.d.).
- Argon, A. S. and S. R. Maloof (1966), ‘Plastic deformation of tungsten single crystals at low temperatures’, *Acta Metallurgica* **14**, 1449.
- Ashby, M. F. and J. D. Embury (1985), ‘The influence of dislocation density on the ductile-brittle transition in bcc metals’, *Scripta Metallurgica* **19**, 557–562.
- Bacon, D. J. and P. P. Grooves (1970), The dislocation in a semi-infinite isotropic medium, in J. A. Simmons, R. de Wit and R. Bullough, eds, ‘Fundamental Aspects of Dislocation Theory’, Vol. I, National Bureau of Standards (U.S.), Spec. Publ. 317, pp. 35–45.
- Baither, D., F. Ernst, T. Wagner, M. Rühle, M. Bartsch and U. Messerschmidt (1999), ‘Micromechanics of fracture in NiAl studied by in situ straining experiments in an HVEM’, *Intermetallics* **7**, 479–489.
- Barnett, D. M. and J. Lothe (1974), ‘An image theorem for dislocations in anisotropic bicrystals’, *Journal of Physics F: Metal Physics* **4**, 1618–1635.
- Bergmann, G. and H. Vehoff (1995), ‘Effect of environment on the brittle-to-ductile transition of pre-cracked NiAl single and polycrystals’, *Materials Science and Engineering A* **192/193**, 309–315.
- Bilby, B. A. and J. D. Eshelby (1968), Dislocations and the theory of fracture, in H. Liebowitz, ed., ‘Fracture – An advanced treatise’, Vol. I, Academic Press, New York and London, pp. 100–178.
- Booth, A. S. and S. G. Roberts (1997), ‘The brittle-to-ductile transition in γ -TiAl single crystals’, *Acta Materialia* **45**, 1045–1053.

- Boussinesq, J. (1885), *Applications des potentiels à l'étude de l'équilibre des solides élastiques*, Gautiers-Villars, Paris.
- Brede, M. (1993), 'The brittle-to-ductile transition in silicon', *Acta Metallurgica et Materialia* **41**, 211–228.
- Brede, M. and P. Haasen (1988), 'The brittle-to-ductile transition in doped silicon as a model substance', *Acta Metallurgica* **36**, 2003–2018.
- Brunner, D. (1998), 'The plastic behavior of high-purity tungsten', *UHPM-98, September 7–11, 1998, Sevrier Annecy Lake, France* .
- Cleveringa, H. H. M., E. van der Giessen and A. Needleman (1997), 'Comparison of discrete dislocation and continuum plasticity predictions for a composite material', *Acta Materialia* **45**, 3163–3179.
- Cleveringa, H. H. M., E. van der Giessen and A. Needleman (1999), 'A discrete dislocation analysis of rate effects on mode I crack growth (unpublished)', *Delft University of Technology, Report No. 1201* .
- Courtney, T. H. (1999), *Mechanical Behavior of Materials*, 2nd edn, McGraw-Hill Series in Materials Science and Engineering.
- Devincre, B. (1996), Meso-scale simulation of the dislocation dynamics, in H. O.Kirchner, L. P.Kubin and V.Pontikis, eds, 'Computer Simulations in Materials Science', Vol. 308, Series E: Applied Sciences, Kluwer Academic Publishers, Dordrecht, pp. 309–323.
- Devincre, B. and L. P. Kubin (1994), 'Simulations of forest interactions and strain hardening in fcc crystals', *Modelling and Simulation in Matererials Science & Engineering* **2**, 559–570.
- Devincre, B. and M. Condat (1992), *Acta Metallurgica et Materialia* **40**, 2629.
- Devincre, B. and S. G. Roberts (1996), 'Three-dimensional simulation of dislocation-crack interactions in b.c.c. metals at the mesoscopic scale', *Acta Materialia* **44**, 2891–2900.
- Domke, W. (1994), *Werkstoffkunde und Werkstoffprüfung (in German)*, 10. edn, Cornelsen Schwann - Giradet, Essen, Germany.
- Duesbery, M. S. and W. Xu (1998), 'The motion of edge dislocations in body-centered cubic metals', *Scripta Materialia* **39**, 283–287.
- Eberhart, M. E. (2000), 'Warum Marmor bricht und Eisen nicht (in German)', *Spektrum der Wissenschaft* **Januar 2000**, 44–50.
- Ebrahimi, F. and S. Shrivastava (1998), 'Brittle-to-ductile transition in NiAl single crystal', *Acta Materialia* **46**, 1493–1502.
- Ebrahimi, F. and T. G. Hoyle (1997), 'Brittle-to-ductile transition in polycrystalline NiAl', *Acta Materialia* **45**, 4193–4204.
- Fivel, M. C. (1997), PhD thesis, INP Grenoble, France.
- Fivel, M. C., C. F. Robertson, G. R. Canova and L. Boulanger (1999), '3D modeling of indent induced plastic zone at a mesoscale', *Acta Materialia* **46**, 6183–94.

- Fivel, M. C., T. J. Gosling and G. R. Canova (1996), 'Implementing image stresses in a 3D dislocation simulation', *Modelling and Simulation in Materials Science & Engineering* **4(6)**, 581–596.
- Fivel, M. C., T. Verdier and G. R. Canova (1997), *Materials Science and Engineering A* **234–236**, 923.
- Gao, H. (1989), 'Application of 3-d weight functions—i. formulations of crack interactions with transformation strains and dislocations', *Journal of the Mechanics and Physics of Solids* **37**, 133–153.
- Gao, H. and J. R. Rice (1989), 'Application of 3-d weight functions—ii. the stress field and energy of a shear dislocation loop at a crack tip', *Journal of the Mechanics and Physics of Solids* **37**, 155–174.
- George, A. and G. Michot (1993), *Materials Science and Engineering A* **164**, 118–134.
- Glebovsky, V. G., B. M. Shipilevsky, I. V. Kapchenko and V. V. Kireyko (1992), *Alloys and Compounds* **184**, 297.
- Glebovsky, V. G., I. V. Kapchenko and B. M. Shipilevsky (1992), *Alloys and Compounds* **184**, 205.
- Göken, M., H. Vehoff and P. Neumann (1995), 'Investigations of loaded crack tips in NiAl by atomic force microscopy', *Scripta Metallurgica et Materialia* **33**, 1187–1192.
- Gottschalk, K. H., N. Hiller, S. Sauerland, P. Specht and H. Alexander (1993), 'Constricted dislocations and their use for TEM measurements of the velocities of edge and 60-degree dislocations in silicon - A new approach to the problem of kink migration', *physica status solidi (a)* **138**, 547–555.
- Gumbsch, P. (1995), 'An atomistic study of brittle fracture: Towards explicit failure criteria from atomistic modelling', *Journal of Materials Research* **10**, 2897–2907.
- Gumbsch, P. and H. Gai (1999), 'Dislocation faster than the speed of sound', *Science* **283**, 965–968.
- Gumbsch, P., J. Riedle, A. Hartmaier and H. F. Fischmeister (1998), 'Controlling factors for the brittle-to-ductile transition in tungsten single crystals', *Science* **282**, 1293–1295.
- Gutkin, M. Yu. and A. E. Romanov (1991), 'Straight edge dislocations in a thin two-phase plate', *physica status solidi (a)* **125**, 107–125.
- Hähner, P. and H. Stamm (1995), 'A dislocation dynamical theory of the brittle-to-ductile transition', *Acta Metallurgica et Materialia* **43**, 2797–2805.
- Hansen, S., U. Holzwarth, C. Hugenschmidt, U. Maennig, K. Maier and T. Wider (1997), 'In-situ positron annihilation during plastic deformation of copper (aural contribution)', *Positron Annihilation, ICPA-11. 11th International Conference. Kansas City, USA*.
- Hartmaier, A., M. C. Fivel, G. R. Canova and P. Gumbsch (1998), 3D discrete dislocation models of thin-film plasticity, in E. Busso, R. Cammarata, M. Nastasi and W. Oliver, eds, 'Thin Films – Stresses and Mechanical Properties', Vol. 505 of *Materials Research Society Symposium Proceedings Series*, pp. 539–544.

- Hartmaier, A., M. C. Fivel, G. R. Canova and P. Gumbsch (1999), 'Image stresses in a free-standing thin film', *Modelling and Simulation in Materials Science & Engineering* **7**, 781–793.
- Hartmaier, A. and P. Gumbsch (1997), 'On the activation energy for the brittle/ductile transition', *physica status solidi (b)* **202**, R1.
- Hartmaier, A., W. D. Nix, P. Gumbsch and E. Arzt (1999), 'Discrete dislocation simulation of work hardening in thin films on substrates', *to be published*.
- Hirsch, P. B. (1960), 'oral contribution', *5th International Congress of Crystallography, Cambridge*.
- Hirsch, P. B. and S. G. Roberts (1989), 'The dynamics of edge dislocation generation along a plane orthogonal to a mode I crack', *Scripta Metallurgica* **23**, 925–930.
- Hirsch, P. B., S. G. Roberts and J. Samuels (1989), 'The brittle-ductile transition in silicon. ii. interpretation', *Proceedings of the Royal Society London* **A421**, 25–53.
- Hirth, J. P. and J. Lothe (1992), *Theory of Dislocations*, reprinted (second) edn, Krieger Publishing Company, Malabar, Florida.
- Hsia, K. J. and A. S. Argon (1994), Experimental study of the mechanisms of brittle-to-ductile transition of cleavage in Si single crystals, *in* H. K. et al., ed., 'International Conference on Fundamentals of Fracture', pp. 31–39.
- Huang, H. and W. W. Gerberich (1994), 'Quasi-equilibrium modeling of the toughness transition during semibrittle cleavage', *Acta Metallurgica et Materialia* **42**, 639–647.
- Hutchinson, J. W. (1968), *Journal of the Mechanics and Physics of Solids* **16**, 13.
- Jassby, K. M. and T. Vreeland, Jr. (1970), *Philosophical Magazine* **21**, 1147.
- Khantha, M. (1994), 'The brittle-to-ductile transition – ii: Dislocation dynamics and the strain-rate dependence of the transition temperature', *Scripta Metallurgica et Materialia* **31**, 1355–1360.
- Khantha, M., D.P. Pope and V. Vitek (1994), 'The brittle-to-ductile transition – i: A cooperative dislocation generation instability', *Scripta Metallurgica et Materialia* **31**, 1349–1354.
- Khantha, M., V. Vitek and D. P. Pope (1995), 'The brittle-to-ductile transition: A cooperative dislocation generation instability', *Key Engineering Materials* **103**, 227–236.
- Kim, H. S. and S. G. Roberts (1994), *Journal of the American Ceramical Society* **77**, 2099.
- Kocks, U. F., A. S. Argon and M. F. Ashby (1975), Thermodynamics and kinetics of slip, *in* B. Chalmers, J. W. Christian and T. B. Massalski, eds, 'Progress in Materials Science', Vol. 19, Pergamon Press Ltd., Oxford, UK.
- Kosterlitz, J. M. and D. J. Thouless (1972), *Journal of Physics C: Solid State Physics* **6**, 1181.
- Kubin, L. P., B. Devincre, G. Canova and Y. Bréchet (1995), '3-D simulations of dislocations and plasticity', *Key Engineering Materials* **103**, 217–226.

- Kubin, L. P., G. Canova, M. Condat, B. Devincere, V. Pontikis and Y. Bréchet (1992), 'Dislocation microstructures and plastic flow: A 3D simulation', *Solid State Phenomena* **23&24**, 455–472.
- Lii, M.-J., X.-F. Chen, Y. Katz and W. W. Gerberich (1990), 'Dislocation modeling and acoustic emission observation of alternating ductile/brittle events in Fe-3wt%Si crystals', *Acta Metallurgica et Materialia* **38**, 2435–2453.
- Lin, I.-H. and R. Thomson (1986), 'Cleavage, dislocation emission, and shielding for cracks under general loading', *Acta Metallurgica* **34**, 187–206.
- Loyola de Oliveira, M. A. and G. Michot (1994), Analysis of crack-dislocation interaction: crack closure, crack opening, in H. K. et al., ed., 'International Conference on Fundamentals of Fracture', pp. 59–65.
- Lubarda, V., J. A. Blume and A. Needleman (1993), *Acta Metallurgica et Materialia* **41**, 625.
- Ludwig, M. and P. Gumbsch (1998), 'Cleavage fracture and crack tip dislocation emission in B2 NiAl: An atomistic study', *Acta Materialia* **46**, 3135–3143.
- Marsh, P. G. and W. W. Gerberich (1994), 'A microscopically-shielded griffith criterion for cleavage in grain oriented silicon steel', *Acta Metallurgica et Materialia* **42**, 613–619.
- Michot, G. (1997), 'Overview of crack dislocation interactions', *2do Congresso Internacional de Tecnologia Metalurgica e de Materiais (ABM), 12.-17. October 1997, Sao Paulo, Brasil*.
- Nadgorny, E. (1988), Dislocation dynamics and mechanical properties of crystals, in J. W. Christian, P. Haasen and T. B. Massalski, eds, 'Progress in Materials Science', Vol. 31, pp. 1–531.
- Needleman, A. (1987), *Journal of Applied Mechanics* **54**, 525–531.
- Nitzsche, V. R. and K. J. Hsia (1994), 'Modelling of dislocation mobility controlled brittle-to-ductile transition', *Materials Science and Engineering* **A176**, 155–164.
- Nix, W. D. (1997), 'Elastic and plastic properties of thin films on substrates: nanoindentation techniques', *Materials Science and Engineering* **A234-236**, 37–44.
- Ochmann, P. and H. Vehoff (1995), 'Experimental investigation of the fracture toughness of NiAl bicrystals combined with computer simulations', *Materials Science and Engineering* **A192/193**, 364–370.
- Pearson, W. B. (1956), Handbook of lattice spacings and structures of metals, in G. V. Raynor, ed., 'International Series of Monographs on Metal Physics and Physical Metallurgy', Vol. 4.
- Pippan, R. and F. Riemelmoser (1995), 'Dislocation shielding of fatigue cracks', *Zeitschrift für Metallkunde* **86**, 823–826.
- Prekel, H. L., A. Lawly and H. Conrad (1968), 'Dislocation velocity measurements in high purity molybdenum', *Acta Metallurgica* **16**, 337–345.
- Press, W. H., B. P. Flannery, S. A. Teukolsky and W. T. Vetterling (1986), *Numerical Recipes*, Cambridge University Press, Cambridge, UK.

- Rice, J. R. (1968), Mathematical analysis in the mechanics of fracture, *in* H.Liebowitz, ed., 'Fracture – An advanced treatise', Vol. II, Academic Press, New York and London, chapter 3, pp. 192–314.
- Rice, J. R. and G. F. Rosengren (1968), *Journal of the Mechanics and Physics of Solids* **16**, 1.
- Rice, J. R. and R. Thomson (1974), 'Ductile versus brittle behavior of crystals', *Philosophical Magazine A* **29**, 73–97.
- Riedle, J. (1995), Bruchwiderstand in Wolfram-Einkristallen: Einfluß der kristallographischen Orientierung, der Temperatur und der Lastrate, PhD thesis, Universität Stuttgart.
- Riedle, J., P. Gumbsch and H. F. Fischmeister (1996), 'Cleavage anisotropy in tungsten single crystals', *Physical Review Letters* **76**, 3594–3597.
- Roberts, S. G. (1996), Modelling the brittle to ductile transition in single crystals, *in* H. O.Kirchner, L. P.Kubin and V.Pontikis, eds, 'Computer Simulations in Materials Science', Vol. 308, Series E: Applied Sciences, Kluwer Academic Publishers, Dordrecht, pp. 409–433.
- Roberts, S. G., A. S. Booth and P. B. Hirsch (1994), 'Dislocation activity and brittle-ductile transitions in single crystals', *Materials Science and Engineering A* **176**, 91–98.
- Roberts, S. G., P. B. Hirsch, A. S. Booth, M. Ellis and F. C. Serbena (1993), 'Dislocations, cracks and brittleness in single crystals', *Physica Scripta* **T49**, 420–426.
- Samuels, J. and S. G. Roberts (1989), 'The brittle-ductile transition in silicon. i. experiments', *Proceedings of the Royal Society London A* **421**, 1–23.
- Schadler, H. WS. (1964), 'Mobility of edge dislocations on {110} planes in tungsten single crystals', *Acta Metallurgica* **12**, 861–870.
- Schoeck, G. (1965), *physica status solidi* **8**, 499.
- Schoeck, G. (1991), 'Dislocation emission from crack tips', *Philosophical Magazine A* **63**, 111–120.
- Schroll, R., V. Vitek and P. Gumbsch (1998), 'Core properties and motion of dislocations in nial', *Acta Materialia* **46**, 903–918.
- Schwarz, K. W. (1997), 'Interaction of dislocations on crossed glide planes in a strained epitaxial layer', *Physical Review Letters* **78**, 4785–4788.
- Schwarz, K. W. and J. Tersoff (1996), 'Interaction of threading and misfit dislocations in a strained epitaxial layer', *Applied Physics Letters* **69**, 1220–1222.
- Seeger, A. (1981), 'The temperature and strain-rate dependence of the flow stress of body-centered cubic metals: A theory based on kink-kink interactions', *Zeitschrift für Metallkunde* **72**, 369–380.
- Seeger, A. and B. Šesták (1978), 'Gleitung und Verfestigung in kubisch-raumzentrierten Metallen und Legierungen (in german) (I–III)', *Zeitschrift für Metallkunde* **69**, 195;355;425.

- Serbena, F. C. and S. G. Roberts (1994), 'The brittle-to-ductile transition in germanium', *Acta Metallurgica et Materialia* **42**, 2505–2510.
- Shrivastava, S. (1997), Brittle-to-ductile transition in NiAl single crystals, PhD thesis, University of Florida.
- St. John, C. (1975), *Philosophical Magazine* **32**, 1193.
- Suo, Z., C. F. Shih and A. G. Varias (1993), 'A theory for cleavage cracking in the presence of plastic flow', *Acta Metallurgica et Materialia* **41**, 1551–1557.
- Tang, M., L. P. Kubin and G. R. Canova (1998), 'Dislocation mobility and the mechanical response of b.c.c. single crystals: A mesoscopic approach', *Acta Materialia* **46**, 3221–3235.
- Thomson, R. (1986), Physics of fracture, in H. Ehrenreich and D. Turnbull, eds, 'Solid State Physics', Vol. 39, Academic Press, New York, pp. 1–129.
- Vehoff, H. (1992), in 'Ordered Intermetallics—Physical Metallurgy and Mechanical Behavior', Vol. 213 (Series E, Applied Sciences), Kluwer, Dordrecht, p. 299.
- Vitek, V. (1974), *Crystal Lattice Defects* **5**, 1.
- Warren, P. D. (1989), 'The brittle-ductile transition in silicon: The influence of pre-existing dislocation arrangements', *Scripta Metallurgica* **23**, 637–642.
- Wider, T., S. Hansen, U. Holzwarth and K. Maier (1998), 'Sensitivity of positron annihilation to plastic deformation', *Physical Review B-Condensed Matter* **57**, 5126–5139.
- Xin, Y.-B. and K. J. Hsia (1997), 'Simulation of the brittle-ductile transition in silicon single crystals using dislocation mechanics', *Acta Materialia* **45**, 1747–1759.
- Xu, G., A. S. Argon and M. Ortiz (1995), 'Nucleation of dislocations from crack tips under mixed modes of loading: implications for brittle against ductile behavior of materials', *Philosophical Magazine A* **72**, 415–451.
- Zacharopoulos, N., D. J. Srolovitz and R. A. LeSar (1997), 'Dynamic simulation of dislocation microstructures in mode III cracking', *Acta Materialia* **45**, 3745–3763.
- Zbib, H. M., M. Rhee and J. P. Hirth (1998), 'On plastic deformation and the dynamics of 3D dislocations', *International Journal of Mechanical Sciences* **40**, 113–127.
- Zhou, S. J., D. L. Preston, P. S. Lomdahl and D. M. Beazley (1998), 'Large-scale molecular dynamics simulations of dislocation intersection in copper', *Science* **279**, 1525–1527.
- Zhou, S. J., D. M. Beazley, P. S. Lomdahl and B. L. Holian (1996), 'Dynamic crack processes via molecular dynamics', *Physical Review Letters* **76**, 2318–2321.
- Zhou, S. J. and R. Thomson (1991a), 'Dislocation emission at ledges on cracks', *Journal of Materials Research* **6**, 639–653.
- Zhou, S. J. and R. Thomson (1991b), 'Shielding of cracks in a plastically polarizable material', *Journal of Materials Research* **6**, 1763–1772.
- Ziebart, U. (1986), Experimentelle Untersuchungen zum Beitrag von Versetzungen zur inneren Reibung von Wolfram, PhD thesis, Universität Stuttgart.

- Zielinski, W., H. Huang, S. Venkataraman and W. W. Gerberich (1995), 'Dislocation distribution under a microindentation into an iron-silicon single crystal', *Philosophical Magazine A* **72**, 1221–1237.

Appendix A

Peach-Koehler force on a screw dislocation in front of a crack

A semi-infinite crack in an infinite, isotropic, and linear elastic medium is considered. The stress field σ due to a mode-I loading of the crack with stress intensity K is given as [see for example (Thomson, 1986, Section 9)]

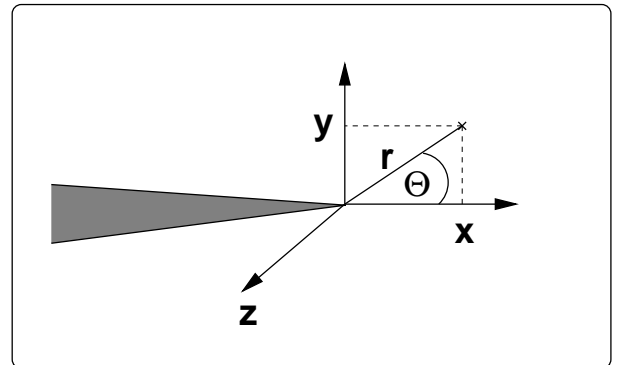
$$\left. \begin{array}{l} \sigma_{xx} \\ \sigma_{yy} \\ \sigma_{xy} \end{array} \right\} = \frac{K}{\sqrt{2\pi r}} \left\{ \begin{array}{l} \cos(\Theta/2) [1 - \sin(\Theta/2) \sin(3\Theta/2)] \\ \cos(\Theta/2) [1 + \sin(\Theta/2) \sin(3\Theta/2)] \\ \sin(\Theta/2) \cos(\Theta/2) \cos(3\Theta/2) \end{array} \right.$$

$$\sigma_{zz} = \begin{cases} 0 & \text{for plane stress} \\ \nu(\sigma_{xx} + \sigma_{yy}) & \text{for plane strain} \end{cases} \quad (\text{A.1})$$

$$\sigma_{xz} = \sigma_{yz} = 0,$$

where ν is the Poisson ratio. The coordinates r and Θ are defined by the cylindrical coordinate system that has its origin in the crack tip (Figure A.1). The Cartesian components of the stress tensor are given according to the coordinate system in Figure A.1.

Figure A.1: Sketch of the coordinate systems used at a crack tip. The crack front represents the Cartesian z -axis and is perpendicular to the plane of the paper.



The Peach-Koehler force \mathbf{f}_{PK} per unit length on a screw dislocation with Burgers vector $\mathbf{b} = (b_x, b_y, b_z)$, is written as [see for example (Hirth and Lothe, 1992, Section 3.6)]

$$\begin{aligned} \mathbf{f}_{\text{PK}} &= (\boldsymbol{\sigma} \cdot \mathbf{b}) \times \mathbf{b} \\ &= \left[b_y b_z (\sigma_{yy} - \sigma_{zz} + \sigma_{xy}), b_x b_z (\sigma_{zz} - \sigma_{xx} - \sigma_{xy}), b_x b_y (\sigma_{xx} - \sigma_{yy}) \right]. \end{aligned} \quad (\text{A.2})$$

The symbol “ \times ” means the vector product. In this equation the stress components equal to zero have already been eliminated. For simplicity it is assumed here that the coordinate system of the crack corresponds to the crystal coordinate system, which means that the (010)[001]-crack system is considered.

For the glide along the crack front, *i.e.* the z -axis, only the z -component of the Peach-Koehler force is of importance. Combining Equations (A.1) and (A.2) yields for this component

$$f_{\text{PK}}^{(z)} = -\frac{2b_x b_y K}{\sqrt{2\pi} r} \left[\cos(\Theta/2) \sin(\Theta/2) \sin(3\Theta/2) \right]. \quad (\text{A.3})$$

It is verified easily that Equation (A.3) can be written as

$$f_{\text{PK}}^{(z)} = \sigma_{r\Theta} b_x b_y, \quad (\text{A.4})$$

where $\sigma_{r\Theta}$ is the shear stress component in cylindrical coordinates.

Appendix B

Validation of the line-tension correction

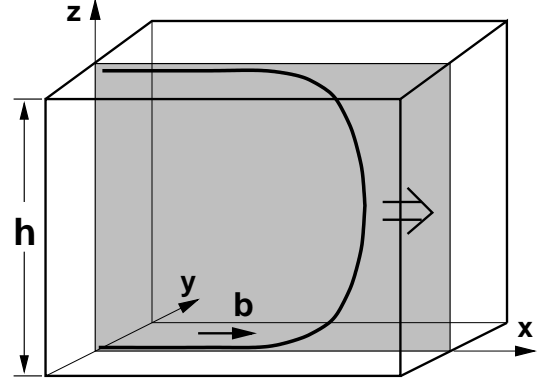
The calculation of the self-stress of a curved dislocation requires the line integral over the whole dislocation line to be performed. Since this integral diverges at the point under consideration, it is necessary to introduce a cut-off radius (Hirth and Lothe, 1992, Chapter 6). If the dislocation line is discretized into pairwise orthogonal segments, the discretization length determines this cut-off radius. Therefore, the self stress of a discretized dislocation depends on the discretization length.

Such a dependence on the discretization length is unphysical. Consequently either a term correcting for the local self-interaction must be introduced (Fivel, 1997; Devincere and Condat, 1992), or the discretization length must be chosen such that the results for the line tension, which is mainly determined by the local self-interaction, agree with experimental or theoretical data (Hartmaier et al., 1998; Hartmaier, Fivel, Canova and Gumbsch, 1999). In this work the former approach is chosen, because it yields a better efficiency of the method. The line tension correction is evaluated according to Equation (3.5) with the fitting parameter γ .

The correction term for the line tension depends naturally on the discretization length, and therefore must be validated by comparison with experiment or analytical models. Such a model has been derived for the process of channeling of a dislocation through a channel of width h . This process is mainly governed by line tension and hence well-suited for a calibration of the DDD model. Another possibility would be to validate the model by the comparison of the critical stress to operate a Frank-Read source. However, this critical stress depends to some degree on the way how the dislocation segments outside the pinning points are treated.

The channel can be imagined as a layer of thickness h in an infinite medium, bounded by interfaces that are impenetrable to dislocations. By moving through this channel, a mobile dislocation deposits interfacial segments at these interfaces (Figure B.1). An analytical, continuum mechanical analysis of the energetic balance of this process (Nix, 1997) yields a

Figure B.1: Sketch of the configuration used to calculate the critical stress for dislocation channeling.



critical stress

$$\tau_0 = \frac{\mu b}{4\pi} \frac{1}{h} \log\left(\frac{h}{b}\right). \quad (\text{B.1})$$

Below this stress the mobile dislocation cannot move through the channel, because the energy required to lengthen the interfacial segments is higher than the work done by the mobile segment.

Figure B.2: Critical stress to drive a dislocation through a channel. The relative difference of the numerical value τ_{chan} and the value τ_0 defined by Equation (B.1) is plotted as function of the channel width h .

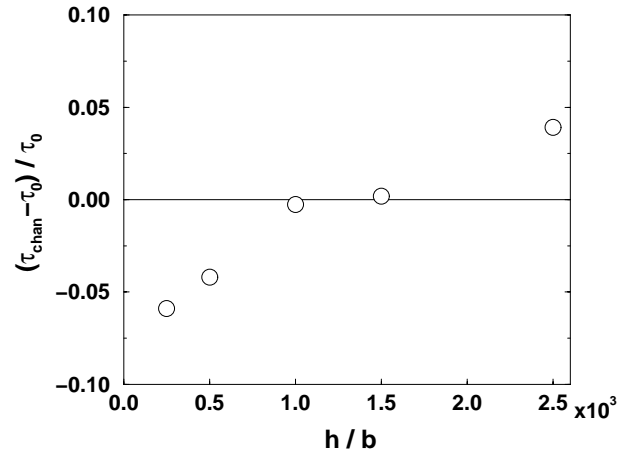


Figure B.2 shows that the numerical results for $\gamma = 2 \times 10^{-5}$ and $L_{\text{min}} = 10b$ agree reasonably well with the theoretical expectations. The error is smaller 5%, within the range of investigated channel widths. However, the numerical results show a trend towards an overestimation of the critical stress for wider channels and an underestimation for smaller channels widths.

Appendix C

Zusammenfassung (in German)

C.1 Einleitung

Materialanwendungen sind oftmals eingeschränkt durch einen Übergang von duktilem Materialverhalten zu Sprödbbruchneigung mit sinkender Temperatur. Dieser Übergang wird gewöhnlich als ein Wettstreit zwischen sprödem Rissfortschritt und der Abstumpfung und Abschirmung der Risssspitze durch plastische Verformung betrachtet. Eine endgültige Antwort, welche Mechanismen die plastische Verformung bei unterschiedlichen Temperaturen unterdrücken oder fördern, konnte bisher noch nicht gefunden werden. Einige Gruppen postulieren, dass die Versetzungsentstehung an der Risssspitze der limitierende und somit entscheidende Mechanismus ist (Rice and Thomson, 1974; Khantha et al., 1995), während andere Gruppen den *Spröd-duktil-Übergang* als thermisch aktivierten Prozess betrachten, der von der Versetzungsmobilität limitiert wird (Hirsch et al., 1989; Nitzsche and Hsia, 1994; Roberts, 1996; Hartmaier and Gumbsch, 1997; Gumbsch et al., 1998).

In der vorliegenden Arbeit wird ein zweidimensionales (2D) Modell entwickelt, das die plastische Verformung im Bereich einer Risssspitze auf der Basis einzelner (diskreter) Versetzungen beschreibt. In diesem Modell können sowohl die Versetzungsmobilität als auch die Versetzungsentstehung gezielt beeinflusst werden. Durch einen Vergleich verschiedener Modellvoraussagen mit experimentellen Befunden ist es möglich, Aussagen über die limitierenden Mechanismen bei verschiedenen Temperaturen zu treffen.

Die homogene Versetzungsentstehung an der Risssspitze erscheint bei Metallen mit kubisch-flächenzentrierter (kfz) Kristallstruktur möglich (Rice and Thomson, 1974; Abraham et al., 1997). Bei Metallen mit kubisch-raumzentrierter (krz) Kristallstruktur hingegen ist die energetische Barriere für homogene Entstehung höher als diejenige für Rissfortschritt (Rice and Thomson, 1974; Schoeck, 1991). Darum tritt Versetzungsentstehung in krz Metallen bevorzugt an Imperfektionen in der Rissfront, wie Stufen oder Kinken, auf (Xu et al., 1995; Zhou and Thomson, 1991a). Die genauen Bedingungen unter welchen Versetzungsquellen an der Rissfront aktiviert werden sind noch nicht verstanden. In der vorliegenden Arbeit wird die Ausbreitung von bereits erzeugten Versetzungskeimen mit Hilfe einer dreidimensionalen (3D) Versetzungsdynamik-Simulation untersucht.

C.2 Modell der Rissspitzenplastizität

Ein einfaches 2D Modell, das bereits früher beschrieben und angewandt wurde (Lin and Thomson, 1986; Roberts, 1996; Hartmaier and Gumbsch, 1997), wird in dieser Arbeit eingesetzt, um die Versetzungsaktivität im Bereich einer Rissspitze zu untersuchen. Die elastische Wechselwirkung von mehreren Versetzungen, die aus der Rissspitzen-Region entspringen, wird im Rahmen der isotropen Elastizitätstheorie beschrieben (Lin and Thomson, 1986; Thomson, 1986), wobei das Rechengebiet die Ebene senkrecht zur Rissfront darstellt (Abbildung 2.6). Diese Beschreibung beinhaltet sämtliche Bildkräfte und Selbst-Wechselwirkungen, die durch die freien Rissflächen verursacht werden.

Der Riss unterliegt einer rein öffnenden Belastung, d.h. die Spannungsintensitäten betragen $K_I = K$ und $K_{II} = K_{III} = 0$. Die Versetzungen werden als reine Stufenversetzungen parallel zur Rissfront beschrieben (Abbildung 2.6). Es wird nur eine Gleitebene betrachtet, wofür die mit der höchsten aufgelösten Schubspannung ausgewählt wurde. Diese Ebene schließt mit der Rissfläche einen Winkel von 72° ein.

Die Gesamtkraft \mathbf{f}_{tot} pro Einheitslänge auf eine Versetzung ergibt sich aus der linearen Überlagerung der Kräfte, die vom Spannungsfeld um die Rissspitze ausgehen, der Bildkräfte und der Kräfte durch die Wechselwirkung mit anderen Versetzungen, die ebenfalls durch die Anwesenheit von freien Oberflächen beeinflusst wird. Nahe der Rissspitze ist die Bildkraft stets stärker als die abstoßende Kraft des Rissfeldes (Lin and Thomson, 1986). Um den Riss existiert daher eine *Zone der Instabilität*, in der Versetzungen zum Riss hin angezogen werden. Trifft eine Versetzung auf eine freie Oberfläche wie die Bruchfläche, wird sie von dieser absorbiert.

Da der Prozess der Versetzungsentstehung an der Rissspitze auf Raum- und Zeitskalen unterhalb der hier betrachteten abläuft, wird ein Kriterium verwendet, das es erlaubt, diesen Prozess in die mesoskopische Modellierung mit einzubeziehen: Eine „Test“-Versetzung wird an den Ort der Versetzungsquelle im Abstand d_{c-s} zur Rissspitze gesetzt (Abbildung 2.6). Ist die Kraft auf diese Versetzung abstoßend, d.h. zeigt sie von der Rissspitze weg, gilt die Versetzung als erzeugt und wird im Folgenden in die Berechnungen miteinbezogen. Im Falle einer anziehenden Kraft, wird keine Versetzung erzeugt, da diese ohnehin vom Riss absorbiert würde (Lin and Thomson, 1986).

Die Geschwindigkeit v_{dis} einer Versetzung ergibt sich aus der aufgelösten Schubspannung $\tau = \mathbf{f}_{\text{tot}} \cdot \mathbf{b}/b^2$ („ \cdot “ bezeichnet das Skalarprodukt, b ist der Betrag des Burgers-Vektors \mathbf{b})¹ und der Temperatur T gemäß

$$v_{\text{dis}}(\tau, T) = A \left(\frac{\tau}{\tau_0} \right)^{m(T)} \exp \left(-\frac{Q_{\text{dis}}}{k_B T} \right), \quad (\text{C.1})$$

dabei ist Q_{dis} die Aktivierungsenergie für die Versetzungsbewegung, $m(T)$ der temperaturabhängige Spannungsexponent und k_B die Boltzmann-Konstante. Die dimensionsbehafteten Konstanten A und τ_0 dienen zum Festlegen der Einheiten von Geschwindigkeit

¹Da hier von reinen Stufenversetzungen ausgegangen wird, definiert die Richtung des Burgers-Vektors gleichzeitig die Gleitrichtung.

und Spannung. Für den Spannungsexponenten wird eine Temperaturabhängigkeit gemäß $m(T) = \alpha + \beta/T$ angenommen (Prekel et al., 1968), mit den Konstanten α und β .

Dieses Mobilitätsgesetz beschreibt die Geschwindigkeit von Nicht-Schraubenversetzungen in krz Metallen. Die Beweglichkeit von reinen Schraubenversetzungen in diesen Metallen unterliegt einer hohen thermischen Aktivierungsschwelle (Peierlsbarriere), sodass diese Versetzungen bei den moderaten Spannungen im Fernfeld des Risses erst oberhalb der so genannten *Knietemperatur* beweglich werden (Argon and Maloof, 1966; Seeger, 1981).

Die Simulationen werden mit einer verschwindenden Spannungsintensität gestartet. Zu Beginn sind keine Versetzungen vorhanden. Während der Simulation wird eine konstante, homogene Temperatur angenommen. Die Spannungsintensität wird mit einer konstanten Rate (Lastrate) erhöht. In jedem Zeitschritt wird das Versetzungsentstehungskriterium überprüft, um zu entscheiden, ob eine neue Versetzung erzeugt wird. Die Entstehung von Versetzungen schirmt den Riss von der äußeren Last ab. Dies führt zu einer effektiven lokalen Spannungsintensität an der Rissspitze, die kleiner ist als die äußere Spannungsintensität. Die Simulation wird beendet, wenn die lokale Spannungsintensität an der Rissspitze einen kritischen Wert übersteigt. Die äußere Spannungsintensität in diesem Moment entspricht der Bruchzähigkeit.

Für das krz Metall Wolfram wird diese kritische lokale Spannungsintensität entsprechend der Tieftemperaturmessungen (Riedle, 1995) mit $k^{\text{crit}} = 2 \text{ MPa}\sqrt{\text{m}}$ angesetzt. Die Materialparameter zur Berechnung der Geschwindigkeit von Nicht-Schraubenversetzungen gemäß Gleichung (C.1) sind in Tabelle 2.3 aufgeführt. Für Wolfram liegt die „Knietemperatur“ $T_{\text{Knie}} = 600 \text{ K}$ (Brunner, 1998) oberhalb der Spröd-duktil-Übergangstemperatur. Die Knietemperatur ist die Grenze bis zu der die plastische Verformung im Massivmaterial thermisch aktiviert verläuft. Bis zu dieser Temperatur wird die plastische Verformung von Schraubenversetzungen limitiert. Schraubenversetzungen sollten somit nur im Bereich nahe der Rissspitze, wo sehr hohe Spannungen vorliegen, beweglich sein. Im Fernfeld hingegen sollten sie weitgehend unbeweglich sein, weswegen dort die Nicht-Schraubenversetzungen die Ratenabhängigkeit der Rissspitzenplastizität bestimmen. Darum wird in dieser Zusammenfassung nicht auf Schraubenversetzungen eingegangen, ihre Rolle wird jedoch im Hauptteil der vorliegenden Arbeit ausführlicher diskutiert.

C.2.1 Versetzungsentstehung

Das oben beschriebene Kriterium zur Versetzungsentstehung beschreibt die homogene Versetzungsentstehung entlang der Rissspitze. Eine solche homogene Entstehung ist jedoch wie bereits erwähnt in krz Metallen nicht ohne weiteres möglich. Darum soll in diesem Abschnitt eine Erweiterung des Modells im Hinblick auf ein realistischeres Entstehungskriterium beschrieben werden.

Aufgrund der geometrischen Einschränkungen des 2D Modells kann die Versetzungsentstehung an diskreten Stellen entlang der Rissfront nicht direkt in das Modell einbezogen werden. Basierend auf Ideen von Roberts (1996) wird hier ein Modell entwickelt, welches

die wesentlichen Eigenschaften der Versetzungsentstehung an diskreten Quellen beinhaltet und zugleich leicht in die 2D Simulation implementiert werden kann. Dazu wird zunächst die Versetzungsentstehung an Stufen in der Rissfront näher beleuchtet.

Untersuchungen von Zhou and Thomson (1991a) und Xu et al. (1995) zeigten, dass die Versetzungsentstehung an Stufen in der Rissfront den geringsten energetischen Aufwand erfordert. Versetzungen, die an solchen Stufen entstehen, bewegen sich jedoch primär auf Gleitebenen, die zur nominellen Rissfront geneigt sind und diese somit nicht enthalten. Die Abschirmung des Risses durch solche Versetzungsschleifen ist recht hoch aber lokalisiert um den Quellenort (Devincre and Roberts, 1996). Außerdem tragen solche Versetzungen nicht zur Abstumpfung des Risses bei. Des weiteren folgt aus geometrischen Überlegungen, dass Versetzungsschleifen stets große Teile mit Schraubencharakter besitzen, die sich im Fernfeld des Risses bewegen müssen (Devincre and Roberts, 1996). Für die schwer beweglichen Schraubenversetzungen von krz Metallen bedeutet dies, dass einmal erzeugte Versetzungen nahe beim Riss bleiben und dadurch weitere Versetzungsentstehungen erschweren.

In der vorliegenden Arbeit wird ein Quergleitmechanismus vorgeschlagen, der Versetzungsschleifen von geneigten Gleitebenen auf Gleitebenen transferiert, welche die Rissfront enthalten. Dazu ist es notwendig, dass der Teil der Versetzung, der mit der Rissfront verbunden ist, Schraubencharakter besitzt und somit quergleiten kann (Abbildung 3.3). Details der Versetzungsentstehung können nur auf atomarer Raum- und Zeitskala geklärt werden, jedoch kann mit Hilfe von kontinuumsmechanischen Überlegungen gezeigt werden (siehe z.B. Anhang A), dass auf ein mit der nominellen Rissfront verbundenes Schraubensegment stets eine Triebkraft für die Bewegung entlang der Rissfront wirkt. Durch die Anwesenheit einer Stufe in der Rissfront wird diese Triebkraft lokal noch verstärkt (Abschnitt 3.2.3 dieser Arbeit). Durch diesen Quergleitprozess werden die auf geneigten Gleitebenen entstandenen Versetzungen gleichsam entlang der Rissfront ausgezogen. Dabei müssen sich die Versetzungssegmente mit Schraubencharakter nur im hohen Spannungsfeld nahe an der Risssspitze bewegen. Im Fernfeld des Risses bewegen sich nur Nicht-Schrauben-Anteile. Darüber hinaus wird die Rissfront durch diesen Prozess abgestumpft. Sowohl die Abschirmung als auch die Abstumpfung des Risses sind jedoch auf den Bereich beschränkt, der in der Versetzungsschleife enthalten ist.

Befinden sich entlang der Rissfront mehrere Quellen, deren Versetzungen auf die gleiche Gleitebene quergleiten, so verbinden sich die Versetzungslinien durch Versetzungsannihilationsprozesse. Aufgrund der Linienspannung besteht eine Triebkraft, diese Versetzungslinien in eine möglichst geradlinige Formation zu bringen. Diese gerade Versetzungslinie ist dann wieder näherungsweise parallel zur Rissfront und kann somit im 2D Modell beschrieben werden.

Letzteres geschieht indem die Abschirmung einer Versetzung, die nach dem ursprünglichen Modell entstanden ist, solange nicht mitberücksichtigt wird bis sich die Versetzung eine gewisse Distanz δ vom Riss entfernt hat. Diese Distanz δ beschreibt somit die Ausdehnung, die eine Versetzungsschleife erfährt, bis sie sich mit anderen Versetzungen verbunden hat und somit die gesamte Rissfront abgeschirmt und abgestumpft ist.

Der Modellparameter δ ist im allgemeinen abhängig vom Abstand der Quellen entlang der Rissfront und der Beweglichkeit der Versetzungen, die ihrerseits eine Funktion der angelegten Spannung und der Temperatur ist. Die angelegte Spannung ist durch den Ort der Versetzung und durch die Lastrate gegeben. Eine 3D Studie des Versetzungsgleitens entlang der Rissfront zeigt, dass der Einfluss des Quellenabstands in einem gewissen Parameterbereich größer ist als der der Lastrate (siehe Abschnitt 4.2.1). Somit wird der Modellparameter δ in erster Näherung als lastratenunabhängig aber proportional zum Quellenabstand betrachtet.

Wiederum für Wolfram konnte der Quellenabstand λ aus *post mortem*-Untersuchungen an Bruchflächen abgeschätzt werden (Gumbsch et al., 1998). Es ergaben sich Werte von $\lambda = 60 \mu\text{m}$ bei $T = 77\text{K}$ und $\lambda = 3 \mu\text{m}$ bei Raumtemperatur. Diese Werte wurden für Berechnungen bei anderen Temperaturen linear inter- bzw. extrapoliert.

C.2.2 Rissabstumpfung

Um den Einfluss der Rissabstumpfung qualitativ in das 2D Modell mit einzubeziehen, wurde die Erhöhung der kritischen lokalen Spannungsintensität als proportional zur Wurzel aus dem Abstumpfungsradius betrachtet. Dies basiert auf Überlegungen wonach die maximale Spannung σ_{max} vor einem abgestumpften Riss mit der Wurzel des Abstumpfungsradius r ansteigt (Rice, 1968, Gleichung (161)). Der Abstumpfungsradius wird als proportional zur Anzahl der erzeugten Versetzungen angenommen.

C.3 Ergebnisse

Im Folgenden werden die Ergebnisse der 2D Simulationen unter verschiedenen Modellvoraussetzungen betrachtet. Dabei wird stets die Bruchzähigkeit als Funktion der Temperatur bei verschiedenen Lastraten wiedergegeben. Zunächst wird das einfachste Modell verwendet, in dem von homogener Versetzungsentstehung ausgegangen wird. In diesem Modell wird auch der Einfluss einer konstanten Gitterreibspannung analysiert. Anschließend werden die Ergebnisse präsentiert, die unter der Annahme der Versetzungsentstehung an diskreten Quellen entlang der Rissfront erhalten wurden. Schließlich wird noch qualitativ der Einfluss der Rissabstumpfung betrachtet.

Die diskreten Punkte, die sich aus der Simulation ergeben, sind stets mit Linien verbunden. Diese Linien dienen nur zur Führung des Auges, da gewöhnlich Ergebnisse für verschiedene Parameter in einer Abbildung wiedergegeben sind. Die Liniestücke basieren nicht auf einem analytischen Ansatz für die Kurvenform.

Wird die Rissabstumpfung vernachlässigt und homogene Versetzungsentstehung an der Rissfront vorausgesetzt, ergeben sich aus der 2D Simulation Bruchzähigkeiten, die streng monoton mit der Temperatur ansteigen (Abbildung 4.4). Die Erhöhung der Bruchzähigkeit in einem bestimmten Temperaturintervall schwächt sich mit steigender Temperatur ab. Eine Erhöhung der Lastrate senkt die Bruchzähigkeit bei allen Temperaturen. Ein Übergang zu

plastischem Verhalten oder ein starker Anstieg der Bruchzähigkeit ab einer bestimmten Temperatur wird im 2D Modell nicht gefunden.

Eine Gitterreibspannung kann in das Modell miteinbezogen werden, indem der Betrag der Triebkraft für die Versetzungsbewegung um einen konstanten Wert vermindert wird. Dadurch wird die mittlere Versetzungsgeschwindigkeit bei allen Temperaturen verringert. Wie in Abbildung 4.6 zu sehen ist, vermindert diese Herabsetzung der Versetzungsbeweglichkeit auch die Bruchzähigkeit bei allen Temperaturen.

Der Einfluss der Versetzungsentstehung kann mit dem in Abschnitt C.2.1 eingeführten Modellparameter δ untersucht werden. Dieser Parameter gibt die zusätzliche Distanz an, die sich eine Versetzung von der Risspitze entfernen muss, bevor ihre Abschirmung berücksichtigt wird. In der vorliegenden Arbeit wird dieser Parameter als der zehnte Teil des mittleren Abstands der Versetzungsquellen entlang der Risspitze angesetzt, der wiederum linear mit der Temperatur sinkt (siehe Abschnitt C.2.1).

In Abbildung 4.12 ist zu sehen, dass die große Distanz δ bei niedrigen Temperaturen die Bruchzähigkeit deutlich herabsetzt. Außerdem ist der Einfluss der Lastrate bei tiefen Temperaturen deutlich verringert. Bei Temperaturen oberhalb $T = 300$ K verschwindet die Distanz δ , so dass die Bruchzähigkeit gleich derjenigen ist, die für homogene Versetzungsentstehung erhalten wurde. Unmittelbar unterhalb dieser Temperatur steigt die Bruchzähigkeit stark an, bei höheren Temperaturen ist der Anstieg mit der Temperatur relativ flach.

Wird der Einfluss der Rissabstumpfung zusätzlich wie beschrieben berücksichtigt, so ergibt sich eine Erhöhung der Bruchzähigkeit (Abbildung 4.14). Besonders ausgeprägt ist die Erhöhung bei höheren Temperaturen, wo viele Versetzungen erzeugt werden. Allerdings ergibt sich auch in diesen Rechnungen kein vollständig plastisches Verhalten oder ein starker Anstieg der Bruchzähigkeit bei einer bestimmten Temperatur, der als Spröd-duktil-Übergang interpretiert werden könnte.

C.4 Diskussion

Die numerischen Ergebnisse werden im Hinblick auf die verschiedenen Temperaturbereiche diskutiert. Dabei wird stets ein Vergleich zwischen Modell und Experiment gezogen, der es erlaubt, Rückschlüsse auf die Mechanismen zu ziehen, welche die plastische Verformung der Risspitzenregion limitieren.

C.4.1 Tieftemperaturbereich

Aus Abbildung 4.4 geht hervor, dass die numerischen Ergebnisse auch bei der Temperatur $T = 50$ K noch eine signifikante Lastratenabhängigkeit zeigen. Dies steht in direktem Widerspruch zu experimentellen Ergebnissen an Wolfram-Einkristallen (Riedle, 1995; Gumbsch et al., 1998). Darüber hinaus sind die numerisch bestimmten Bruchzähigkeiten bei tiefen Temperaturen deutlich höher als die experimentellen Werte.

Durch Variation der Modellparameter, welche die mittlere Versetzungsgeschwindigkeit beschreiben, könnte eine bessere Übereinstimmung sowohl der absoluten Werte als auch der Lastratenabhängigkeit der Bruchzähigkeit erreicht werden. Solche Veränderungen sind allerdings schwer zu rechtfertigen, da die Parameter der Versetzungsmobilität in diesem Temperaturbereich recht verlässlich sind (Schadler, 1964). Eine Erhöhung der Aktivierungsenergie für die Versetzungsbewegung zieht außerdem Probleme bei der Erklärung des halb-spröden Bereichs nach sich.

Wenn die Versetzungsentstehung schon bei tiefen Temperaturen leicht geschieht, ist es schwer zu erklären, warum eine Vorverformung des Materials eine Steigerung der Bruchzähigkeit bei tiefen Temperaturen nach sich zieht, was experimentell bei verschiedenen Materialien gefunden wird (Warren, 1989; Ebrahimi and Shrivastava, 1998; Gumbsch et al., 1998, für Silizium, NiAl und Wolfram). Durch die Vorverformung bei hoher Temperatur vor der Anriss-erzeugung wird die Versetzungsdichte im Material gleichmäßig erhöht. Diese Kaltverfestigung bewirkt zunächst eine Herabsetzung der Versetzungsmobilität was – wie die Ergebnisse für verschiedene Gitterreibspannungen zeigen (Abbildung 4.6) – eher eine Verringerung der Bruchzähigkeit nach sich ziehen sollte. Auch die Polarisation der Versetzungswolke um die Rissspitze senkt die Bruchzähigkeit ab, da sich abschirmende Versetzungen von der Rissspitze entfernen, während Versetzungen, die die rissöffnende Spannung noch verstärken, näher zum Riss gelangen (Zhou and Thomson, 1991b). Bei tiefen Temperaturen ist die Energiedissipation durch die Versetzungsbewegung von untergeordneter Bedeutung im Vergleich zur elastischen Abschirmung.

Die einfachste, mit den Beobachtungen verträgliche Erklärung für die Erhöhung der Bruchzähigkeit bei tiefen Temperaturen durch Vorverformung ist, dass die Versetzungsentstehung an der Rissspitze durch die Präsenz von bereits existierenden Versetzungen erleichtert wird. Dies kann entweder durch Versetzungsmultiplikationsprozesse im hohen Spannungsfeld der Rissspitze geschehen oder durch eine Änderung der Topologie der Rissfront. Eine Erleichterung der Versetzungsentstehung ist aber nur dann wirksam, wenn im unverformten Material die Versetzungsentstehung der limitierende Prozess ist.

Abbildung 5.2 zeigt numerische Ergebnisse für homogene Versetzungsentstehung und Versetzungsentstehung an diskreten Quellen im Vergleich. Es ist zu sehen, dass bei tiefen Temperaturen die Bruchzähigkeit unter der Annahme von homogener Versetzungsentstehung selbst bei einer recht hohen Gitterreibspannung größer ist als die Bruchzähigkeit unter der Annahme von Versetzungsentstehung an diskreten Quellen. Bei höheren Temperaturen, wenn die Versetzungsquellen dichter werden und die Versetzungsentstehung somit leichter geschieht, ist die Bruchzähigkeit größer als die im „verfestigten“ Material (erhöhte Gitterreibspannung). Dies entspricht den experimentellen Ergebnissen (Ebrahimi and Shrivastava, 1998; Gumbsch et al., 1998) im Detail.

Die Ergebnisse für Versetzungsentstehung an diskreten Quellen entlang der Rissfront zeigen, wie auch experimentell gefunden, eine sehr geringe Abhängigkeit von der Lastrate. Außerdem stimmen die Bruchzähigkeiten für Wolfram auch quantitativ wesentlich besser mit den experimentellen Daten überein (siehe Abschnitt 5.2.1).

C.4.2 Halb-spröder Bereich

Ein quantitativer Vergleich von numerischen und experimentellen Ergebnissen bei Raumtemperatur zeigt, dass die Lastratenabhängigkeit der numerischen Ergebnisse geringer ist als die der experimentellen Daten (Abbildung 5.4). Allerdings ergibt sich in der halblogarithmischen Auftragung in beiden Fällen ein Graph, der gut durch eine Ausgleichsgerade beschrieben werden kann. Es zeigt sich, dass die Berücksichtigung der Rissabstumpfung und der Versetzungsentstehung an diskreten Quellen zu einer besseren Übereinstimmung von Simulation und Experiment führt. Bei hohen Lastraten überwiegt die Absenkung der Bruchzähigkeit durch die schwierigere Versetzungsentstehung. Bei niedrigeren Lastraten hingegen, wo mehr Versetzungen erzeugt werden, überwiegt die Bruchzähigkeitssteigerung durch die Abstumpfung. Dadurch ergibt sich eine etwas stärkere Lastratenabhängigkeit der Bruchzähigkeit.

Die Abhängigkeit von der Lastrate kann auch dazu verwendet werden, eine Aussage über die Aktivierungsenergie der Rissspitzenplastizität zu treffen. Geht man davon aus, dass die plastische Verformung an der Rissspitze ein rein thermisch aktivierter Prozess mit einer wohldefinierten Aktivierungsenergie ist, so ergibt sich für Punkte mit gleichem plastischem Verformungsgrad, d.h. gleicher Bruchzähigkeit, eine Arrhenius-artige Beziehung für Lastrate und Temperatur. Dies lässt sich in den Gleichungen

$$\dot{K}_1 = A \exp\left(-\frac{U_{\text{plast}}}{k_B T_1}\right) \quad \text{und} \quad (\text{C.2})$$

$$\dot{K}_2 = A \exp\left(-\frac{U_{\text{plast}}}{k_B T_2}\right) \quad (\text{C.3})$$

ausdrücken, wobei (\dot{K}_1, T_1) und (\dot{K}_2, T_2) Paare von Lastraten und Temperaturen sind, die zur gleichen Bruchzähigkeit führen. Die Aktivierungsenergie für die Rissspitzenplastizität wird als U_{plast} geschrieben, A ist ein Proportionalitätsfaktor.

Dividiert man Gleichung (C.3) durch Gleichung (C.2) und löst nach der Temperatur T_2 auf, so ergibt sich die Beziehung

$$T_2 = \left[\frac{k_B}{U_{\text{plast}}} \ln \frac{\dot{K}_1}{\dot{K}_2} + \frac{1}{T_1} \right]^{-1}, \quad (\text{C.4})$$

mit der $K^{\text{crit}}-T$ -Kurven für verschiedene Lastraten ineinander übergeführt werden können.

Wendet man diese Skalierungsbeziehung auf die Bruchzähigkeiten an, die für homogene Versetzungsentstehung erhalten wurden, so ergibt sich zwar kein striktes Skalierungsverhalten, jedoch werden näherungsweise alle Punkte gleicher Bruchzähigkeit auf eine Masterkurve projiziert (Abbildung 5.6). Die Aktivierungsenergie, die man so erhält beträgt $U_{\text{plast}} = 0.12 \text{ eV}$. Diese Aktivierungsenergie ist niedriger als diejenige für die Versetzungsbewegung, was auf den temperaturabhängigen Spannungsexponenten zurückgeführt werden kann. Für einen konstanten Spannungsexponenten ergibt sich ein strenges Skalierungsverhalten und einen Aktivierungsenergie für die Rissspitzenplastizität, die gleich der Aktivierungsenergie für die Versetzungsbewegung ist (siehe Abschnitt 5.2.3).

Da der Spröd-duktil-Übergang letztlich von der plastischen Verformung der Rissspitze bewirkt wird, kann man davon ausgehen, dass die Aktivierungsenergie für den Spröd-duktil-Übergang gleichzusetzen ist mit der Aktivierungsenergie für die Rissspitzenplastizität. Somit kann aus dem Skalierungsverhalten der numerischen Ergebnisse eine Aussage über die Aktivierungsenergie des Spröd-duktil-Übergangs getroffen werden, obwohl die Simulationsergebnisse keinen starken Anstieg der Bruchzähigkeit ab einer bestimmten Temperatur bzw. keinen Übergang zu duktilem Verhalten zeigen. Dieses Argument wird dadurch unterstützt, dass die experimentellen Ergebnisse von Riedle (1995) für verschiedene Lastraten ebenfalls mit der Beziehung (C.4) auf eine einzige Masterkurve projiziert werden können. Die so gewonnene Aktivierungsenergie für die Rissspitzenplastizität stimmt mit der aus einer Arrhenius-Auftragung gewonnenen Aktivierungsenergie für den Spröd-duktil-Übergang überein, wie im Hauptteil der Arbeit beschrieben wird.

C.4.3 Spröd-duktil-Übergang

Der Vergleich numerischer und experimenteller Ergebnisse hat die Bedeutung der Versetzungsentstehung bei tiefen Temperaturen gezeigt. Es wurden auch Belege dafür angegeben, dass ein physikalisches Modell des Spröd-duktil-Übergangs nicht allein auf der Versetzungsentstehung beruhen kann, sondern notwendigerweise die Versetzungsmobilität einbeziehen muss. Im vorigen Abschnitt wurde gezeigt, dass die Versetzungsbewegung als der entscheidende Prozess im halb-spröden Bereich angesehen werden muss.

Allerdings zeigen experimentelle Ergebnisse für Wolfram-Einkristalle direkt unterhalb der Spröd-duktil-Übergangstemperatur einen starken Anstieg der Bruchzähigkeit (Gumbsch et al., 1998). Ein solcher Anstieg der Bruchzähigkeit wird von den 2D Simulation nicht vorausgesagt, was wohl auf die starken Vereinfachungen zurückzuführen ist, die diesem Simulationsverfahren zugrunde liegen. So bleiben zum Beispiel Versetzungsquergleiten und Versetzungsmultiplikation unberücksichtigt.

Ein Modell, das von Khanta, Pope und Vitek (Khantha et al., 1995) vorgeschlagen wurde, sagt einen sehr abrupten Spröd-duktil-Übergang durch eine kooperative Kosterlitz-Thouless-artige Instabilität voraus. Somit könnte vermutet werden, dass eine solche Instabilität den starken Anstieg der Bruchzähigkeit direkt unterhalb der Spröd-duktil-Übergangstemperatur verursacht. Dieses Modell kann jedoch die Beobachtungen bei Vorverformung sowie die Lastratenabhängigkeit der Spröd-duktil-Übergangstemperatur nicht zufrieden stellend erklären (Abschnitt 5.3).

Ein Selbstverstärkungsmechanismus durch Rissabstumpfung konnte mit der 2D Simulation nicht belegt werden, jedoch sind diese Resultate nur qualitativ zu verstehen. Darum ist ein solcher Selbstverstärkungsmechanismus nicht mit Sicherheit auszuschließen. Ein kontinuumsmechanisches Modell, das auf Nitzsche and Hsia (1994) zurückgeht, belegt zumindest die Bedeutung der Rissabstumpfung für den Spröd-duktil-Übergang (Abschnitt 5.3).

Die Aktivierungsenergie für den Spröd-duktil-Übergang in Wolfram-Einkristallen liegt mit $U_{\text{BDT}} = 0.2 \text{ eV}$ (Gumbsch et al., 1998) eine Größenordnung unterhalb der Aktivierungsenergie

gie für die Bewegung von Schraubenversetzungen in diesem Material (Ziebart, 1986; Brunner, 1998). Der angegebene Wert liegt allerdings recht nahe bei der für die Bewegung von Nicht-Schraubenversetzungen gefundenen Aktivierungsenergie $Q_{\text{dis}} = 0.32 \text{ eV}$ (Schadler, 1964). Die 2D Simulationen, die von einem temperaturabhängigen Spannungsexponenten ausgehen, liefern eine zu niedrige Aktivierungsenergie für die Rissspitzenplastizität ($U_{\text{plast}} = 0.12 \text{ eV}$). Dieser Wert ist jedoch mit einer gewissen Unsicherheit behaftet, da die Werte für den Spannungsexponenten von tieferen Temperaturen extrapoliert wurden.

Das hier vorgestellte Modell der Rissspitzenplastizität geht von einer durch Nicht-Schraubenversetzungen getragenen mikroplastischen Verformung der Rissspitze aus. Setzt man hingegen eine durch Schraubenversetzungen getragene plastische Verformung voraus, wie sie für Massivmaterialien mit krz Kristallstruktur angenommen wird [siehe z.B. (Argon and Maloof, 1966; Seeger, 1981)], so findet der Anstieg der Bruchzähigkeiten erst bei Temperaturen oberhalb der so genannten „Knie temperatur“ statt, die in Wolfram mit $T_{\text{Knie}} \approx 600 \text{ K}$ (Brunner, 1998) bereits über den beobachteten Spröd-duktil-Übergangstemperaturen liegt (Gumbsch et al., 1998). Eine solche Annahme führt also zum direkten Widerspruch mit experimentellen Befunden.

C.5 Zusammenfassung

In der vorliegenden Arbeit wurde die plastische Verformung der Rissspitzenregion mit einem zweidimensionalen numerischen Versetzungsdynamik-Verfahren untersucht. Aus dem Vergleich von numerischen Ergebnissen mit experimentellen Befunden an Wolfram-Einkristallen konnte die Schlussfolgerung gezogen werden, dass die Rissspitzenplastizität bei tiefen Temperaturen von der Versetzungsentstehung an der Rissspitze limitiert wird. Bei mittleren Temperaturen im halb-spröden Bereich muss die Versetzungsmobilität berücksichtigt werden, um die experimentellen Ergebnisse zu erklären. Ein Modell, das eine rein mobilitätskontrollierte mikroplastische Verformung der Rissspitzenregion annimmt, erwies sich als konsistent mit einer Reihe von experimentellen Befunden. Die Abstumpfung der Rissspitze hat einen ausgeprägten Einfluss auf die Bruchzähigkeit im halb-spröden Übergangsbereich und vermutlich auch auf den Spröd-duktil-Übergang selbst.

Curriculum Vitae

Date of Birth: May 5, 1970
 Place of Birth: Zweibrücken, Germany
 Parents: Heide Maria Hartmaier (born Backe)
 Manfred Hartmaier
 Marital Status: Married with Sigrid Hartmaier,
 since April 3, 1992, one child
 Nationality: German

Education

April 1, 1996 – University of Stuttgart, Germany
 March 31, 1998 Graduate student program in materials science
 Oct. 1, 1990 – University of Kaiserslautern, Germany
 Dec. 31, 1995 Diploma program in physics (*Diplom-Physiker*)
 1980 – 1989 Grammar school at Landstuhl, Germany
 High-school certificate (*Abitur*)
 1976 – 1980 Elementary school at Obernheim-Kirchenarnbach, Germany

Professional Activities

since June 1, 1999 Research engineer at the Hilti Corp., Liechtenstein
 Jan. 1, 1996 – Research assistant at the *Max-Planck-Institut für Metallforschung*,
 May 31, 1999 Stuttgart, Germany
 Collaboration in the project “Deformation and Fracture of ordered alloys” supported by the *Deutsche Forschungsgemeinschaft*
 Oct. 27 – Visiting scientist at Stanford University, California, USA
 Nov. 28, 1997 (scholarship from the *Deutscher Akademischer Austauschdienst*, DAAD)
 Sep. 1 – Visiting Scientist at the *Centre Nationale de la Recherche Scientifique*, Châtillon, France (DAAD scholarship)
 Nov. 30, 1996

Award “Graduate Student Silver Medal Award” of the Materials Research Society, Fall Meeting 1998

Civil Service

Aug. 1989 – Educational assistant at the orphanage *Sankt Nikolaus*, Landstuhl,
 Sep. 1990 Germany